Spatial transcriptomic clocks reveal cell proximity effects in brain ageing

https://doi.org/10.1038/s41586-024-08334-8

Received: 13 December 2023

Accepted: 1 November 2024

Eric D. Sun[1,2,3], **Olivia Y. Zhou**[3,4,5], **Max Hauptschein**[3], **Nimrod Rappoport**[3], **Lucy Xu**[3,6], **Paloma Navarro Negredo**[3], **Ling Liu**[7,8,9], **Thomas A. Rando**[7,8,9], **James Zou**[2,13] ✉ & **Anne Brunet**[3,10,11,12,13] ✉

Old age is associated with a decline in cognitive function and an increase in neurodegenerative disease risk[1]. Brain ageing is complex and is accompanied by many cellular changes[2]. Furthermore, the influence that aged cells have on neighbouring cells and how this contributes to tissue decline is unknown. More generally, the tools to systematically address this question in ageing tissues have not yet been developed. Here we generate a spatially resolved single-cell transcriptomics brain atlas of 4.2 million cells from 20 distinct ages across the adult lifespan and across two rejuvenating interventions—exercise and partial reprogramming. We build spatial ageing clocks, machine learning models trained on this spatial transcriptomics atlas, to identify spatial and cell-type-specific transcriptomic fingerprints of ageing, rejuvenation and disease, including for rare cell types. Using spatial ageing clocks and deep learning, we find that T cells, which increasingly infiltrate the brain with age, have a marked pro-ageing proximity effect on neighbouring cells. Surprisingly, neural stem cells have a strong pro-rejuvenating proximity effect on neighbouring cells. We also identify potential mediators of the pro-ageing effect of T cells and the pro-rejuvenating effect of neural stem cells on their neighbours. These results suggest that rare cell types can have a potent influence on their neighbours and could be targeted to counter tissue ageing. Spatial ageing clocks represent a useful tool for studying cell–cell interactions in spatial contexts and should allow scalable assessment of the efficacy of interventions for ageing and disease.

Brain ageing is associated with a striking increase in the risk of neurodegenerative diseases, including Alzheimer's disease and other forms of dementia[1]. Previous studies have interrogated the molecular changes that occur during brain ageing at single-cell resolution[3–15]. These datasets provide rich information on age-related cellular changes in the brain, but they lack insight into the spatial context, especially at scale. We are therefore missing a systematic understanding of spatiotemporal changes in the brain during ageing, including changes in local cell neighbourhoods and cell–cell interactions.

The advent of high-throughput spatial omics holds great promise for characterizing spatial interactions[16]. Although recent studies on spatial brain ageing have helped clarify cellular and regional changes with age[17–19], they have provided either spatial single-cell resolution[17] or temporal resolution[18,19], but not both. The lack of high spatiotemporal resolution at single-cell level in current studies makes it difficult to understand the full range of cell-type-specific changes and interactions that occur throughout life, particularly in geriatric ages, when cognitive decline and the onset of neurodegenerative disease are most prominent. Notably, there is a need for new advanced computational tools to analyse spatial omics data and capture spatial interactions during ageing. Here we generate a spatially resolved single-cell transcriptomics atlas of the mouse brain across adult life and in response to rejuvenating interventions (exercise and partial reprogramming), and we develop powerful machine learning tools to identify prominent cell proximity effects in spatial datasets.

Spatiotemporal atlas of brain ageing

We generated a single-cell spatial transcriptomics atlas of the ageing mouse brain across the entire lifespan (Fig. 1a). We collected coronal brain sections from male mice at 20 different ages tiling the entire lifespan (2 independent cohorts of mice; Methods), as well as sagittal brain sections from male mice at 6 different ages. To generate spatial transcriptomic data at single-cell resolution, we used multiplexed error-robust fluorescence in situ hybridization (MERFISH) technology[20] and measured transcripts of 300 genes across entire coronal or sagittal sections. This 300-gene panel was designed to contain cell-type markers, genes in ageing-related pathways, and genes involved in other

---

[1]Biomedical Data Science Graduate Program, Stanford University, Stanford, CA, USA. [2]Department of Biomedical Data Science, Stanford University, Stanford, CA, USA. [3]Department of Genetics, Stanford University, Stanford, CA, USA. [4]Biophysics Graduate Program, Stanford University, Stanford, CA, USA. [5]Medical Scientist Training Program, Stanford University, Stanford, CA, USA. [6]Biology Graduate Program, Stanford University, Stanford, CA, USA. [7]Department of Neurology, Stanford University, Stanford, CA, USA. [8]Department of Neurology, UCLA, Los Angeles, CA, USA. [9]Eli and Edythe Broad Center for Regenerative Medicine and Stem Cell Biology, UCLA, Los Angeles, CA, USA. [10]Glenn Center for the Biology of Aging, Stanford University, Stanford, CA, USA. [11]Wu Tsai Neurosciences Institute, Stanford University, Stanford, CA, USA. [12]The Phil & Penny Knight Initiative for Brain Resilience at the Wu Tsai Neurosciences Institute, Stanford University, Stanford, CA, USA. [13]These authors contributed equally: James Zou, Anne Brunet. ✉e-mail: jamesz@stanford.edu; abrunet1@stanford.edu

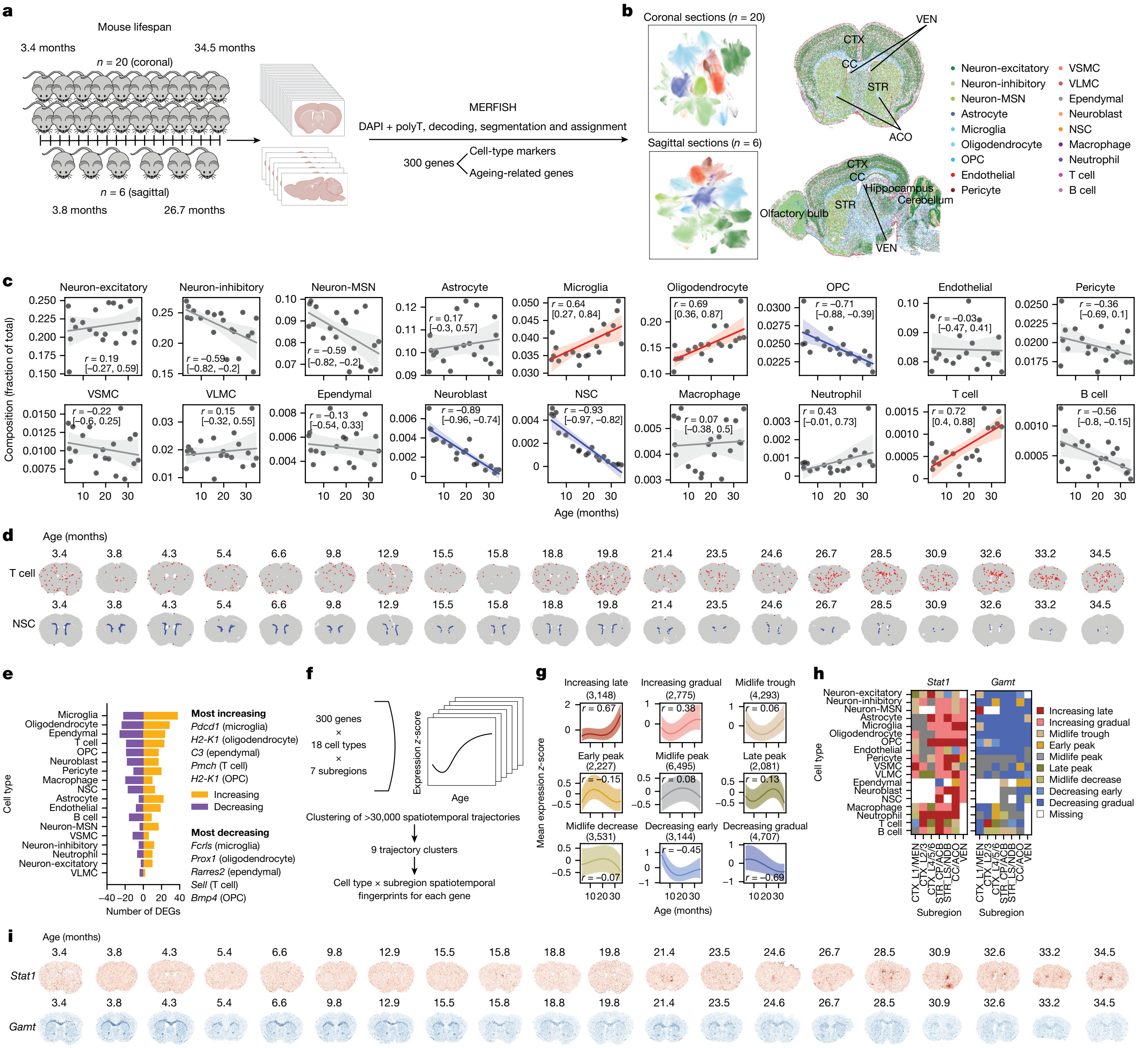

Fig. 1 | Spatially resolved single-cell transcriptomic profiling of the brain across lifespan. a, Experimental workflow for generating spatial transcriptomics data from mouse brains collected across the adult lifespan using MERFISH. **b**, Visualization of single cells coloured by cell type using uniform manifold approximation and projection (UMAP) coordinates across all coronal section samples (top left) or all sagittal section samples (bottom left), and visualizations under spatial coordinates for one representative coronal section (top right) with region labels and one representative sagittal section (bottom right) with some anatomic structures annotated. **c**, Global cell-type composition changes in the coronal section dataset with each dot representing an individual mouse. Line of best fit shown with 95% confidence interval. Pearson correlations (*r*) between cell-type composition and age are shown with their 95% confidence interval. Strong increases are in red and strong decreases are in blue. **d**, Scatter plot of cells by their spatial coordinates across all coronal sections and ages with cells coloured by cell type: T cells (red), NSCs (blue) and other cell types (grey). **e**, Number of genes with increasing or decreasing expression with age for each cell type across coronal sections. Genes with the largest changes are shown for the top five cell types. **f**, Schematic of the clustering approach for identifying spatiotemporal gene expression trajectories across coronal sections. **g**, Smoothed median and interquartile range (error band) of the mean gene expression *z*-scores across age of all gene, cell-type and subregion combinations split into nine annotated clusters. Pearson correlation (*r*) between median gene expression *z*-score and age is shown; number of trajectories within each cluster is noted inside parentheses. **h**, Heat maps showing trajectory cluster membership across different cell types and subregions for two selected genes. **i**, Scatter plot of cells by their spatial coordinates across all coronal sections and ages with cells coloured by scaled log-normalized gene expression of *Stat1* (red) and *Gamt* (blue).

processes (gene panel selection is described in Methods and Supplementary Table 1).

Our spatiotemporal atlas of the ageing mouse brain yielded a total of 2.3 million high quality cells from coronal sections across 20 ages (3.4 to 34.5 months) and sagittal sections across 6 ages (3.8 to 26.7 months) (Supplementary Tables 2–4). MERFISH measurements were highly reproducible across adjacent coronal sections (Extended Data Fig. 1a) and the log-normalized gene expression quantiles were similar across different sections (Extended Data Fig. 1b).

In the coronal dataset, we identified 18 cell types using pre-defined marker genes that are included in the MERFISH gene panel (Extended Data Fig. 1c,d and Supplementary Table 5), including neuronal cell types: excitatory neurons (neuron-excitatory), inhibitory neurons (neuron-inhibitory) and medium spiny neurons (neuron-MSN); glial cell types: astrocytes, oligodendrocytes and oligodendrocyte progenitor cells (OPCs); cell types that are localized to the lateral ventricles (VEN), which contain the neurogenic niche: neural stem cells (NSCs), neuroblasts and ependymal cells; cell types involved in brain vasculature: endothelial cells, pericytes, vascular smooth muscle cells (VSMCs) and vascular leptomeningeal cells (VLMCs); and immune cell types: microglia (the resident immune cell of the brain), T cells, B cells, macrophages and neutrophils (Fig. 1b and Extended Data Fig. 1e). We identified the same cell types except for neutrophils in the sagittal dataset (Fig. 1b). Our atlas includes both abundant cell types (for example, excitatory and inhibitory neurons, oligodendrocytes, astrocytes and microglia) and rare cell types (for example, T cells, B cells, neutrophils, ependymal cells, NSCs and neuroblasts), some of which have not been studied in previous spatial transcriptomics atlases of the brain[17,21–26]. Cell types localized to their expected spatial regions. For example, excitatory neurons were found predominantly in the cortex (CTX), whereas oligodendrocytes were most densely populated in the white matter tracts (Fig. 1b and Extended Data Fig. 1e). The spatial localizations of the main cell types in our dataset are consistent with those in existing spatial transcriptomics studies[17,21,23] (Extended Data Fig. 1f). Immunofluorescence staining also confirmed the spatiotemporal expression of specific markers in the panel (Extended Data Fig. 2).

To determine how cells localize to different regions of the brain, we performed unbiased clustering of cells on the basis of cell neighbourhood abundances[17]. This clustering resulted in annotation of seven anatomic subregions that were manually grouped into four regions: (1) white matter tracts of the corpus callosum and anterior commissure (CC/ACO); (2) three subregions of the CTX (CTX layer 1 and meninges (CTX_L1/MEN), CTX layer 2/3 (CTX_L2/3), CTX layer 4/5/6 (CTX_L4/5/6)); (3) two subregions of the striatum and adjacent regions (STR) (caudoputamen and nucleus accumbens (STR_CP/ACB) and septal nucleus and diagonal band nucleus (STR_LS/NDB)); and (4) the VEN (Fig. 1b and Extended Data Fig. 3a,b). Known cortical layer and neuronal markers exhibited similar spatial expression patterns between our dataset and the Allen brain in situ hybridization atlas[27] (Extended Data Fig. 3c,d and Supplementary Table 1), confirming the coarse annotation of the cortical layers.

We observed a global increase in the proportion of microglia, oligodendrocytes and T cells during ageing, as well as a global decrease in the proportion of OPCs, NSCs and neuroblasts in the coronal section dataset (Fig. 1c and Supplementary Table 6). Notably, T cells and NSCs exhibited the strongest changes with age. T cells were found across all sampled regions and strongly increased with age (Pearson correlation $r = 0.72$ with 95% confidence interval [0.40, 0.88]) (Fig. 1c,d). NSCs were generally localized to the VEN throughout life and substantially decreased in proportion with age (Pearson correlation $r = -0.93$ with 95% confidence interval [−0.97, −0.82]) (Fig. 1c,d).

We also observed region-specific cell-type proportion changes with age (Supplementary Table 6). For example, oligodendrocytes strongly increased in the CTX and STR during ageing (Extended Data Fig. 3e), whereas OPCs strongly decreased in the CC/ACO and STR (Extended Data Fig. 3f). Notably, T cells and microglia strongly increased in the CC/ACO white matter region with age (Extended Data Fig. 3g,h), and T cells also strongly increased in the STR (Extended Data Fig. 3g).

To determine whether similar changes in cell-type proportion during ageing are observed in other regions of the brain, we used our sagittal section dataset, which contains regions such as the olfactory bulb and cerebellum that are not captured in the coronal section dataset. The cell-type proportion changes with age in the sagittal sections were largely consistent with those observed in coronal sections (Extended Data Fig. 3i). T cell numbers increased in several regions of the brain with age (Extended Data Fig. 3j). NSCs were present mostly in the subventricular zone of the VEN, the rostral and caudal migratory streams, and to a reduced extent in the dentate gyrus in sagittal sections (Extended Data Fig. 3j). NSCs decreased in the subventricular zone within the VEN (Extended Data Fig. 3j).

These datasets represent a spatially resolved single-cell atlas of multiple brain regions across life, which reveals substantial changes in cell-type proportions with age.

Spatiotemporal gene expression changes

We identified genes that change in expression during ageing in each cell type (Methods and Supplementary Table 7). Genes that increased in expression with age were generally involved in immune response (Supplementary Fig. 1a and Supplementary Table 8), whereas genes that decreased in expression with age were generally involved in cellular metabolism and development pathways (Supplementary Fig. 1b and Supplementary Table 8). Microglia exhibited the largest number of genes that changed in expression with age of any cell type (Fig. 1e). In microglia, *Pdcd1*, which encodes the receptor PD-1, was one of the most highly upregulated genes with age (Spearman correlation with age $\rho = 0.93$), and *Fcrls*, which encodes a Fc receptor-like molecule, was the most strongly downregulated gene with age (Spearman correlation with age $\rho = -0.76$).

The magnitude of transcriptomic changes in different cell types varied across subregions. The CC/ACO region, which consists of white matter tracts, exhibited the largest gene expression changes across multiple cell types with age (Supplementary Fig. 1c), in line with white matter tracts as hotspots of ageing in the brain[19].

To characterize the patterns of gene expression changes during ageing (hereafter 'trajectories'), we clustered gene expression trajectories across all 20 ages for each combination of gene, cell type and spatial subregion (as defined in Extended Data Fig. 3a), and we identified nine different clusters representing archetypes of gene expression trajectories (Fig. 1f,g and Supplementary Table 7; see Extended Data Fig. 4a,b for other clustering results). Within a given cell type and subregion, the genes present in these trajectory clusters were associated with distinct biological processes. For example, for oligodendrocytes in the CC/ACO, 'decreasing early' genes are implicated in development pathways, whereas 'decreasing gradual' genes are involved in stress response and DNA damage repair; and 'increasing gradual' genes are implicated in many signalling and development pathways, whereas 'increasing late' genes are involved in immune responses (Extended Data Fig. 4c and Supplementary Table 9).

This analysis provides a spatiotemporal transcriptomic fingerprint for any given gene, showcasing its temporal expression pattern for each combination of subregion and cell type. For example, the spatiotemporal fingerprints for the interferon-response genes *Stat1* and *Ifi27* show both 'increasing late' (dark red) and 'increasing gradual' (light red) trajectories with age across nearly all cell types and subregions (Fig. 1h and Extended Data Fig. 4d). Conversely, the spatiotemporal fingerprint for *Gamt*, a gene involved in creatine synthesis, broadly shows 'decreasing gradual' (dark blue) trajectories with age (Fig. 1h), whereas the antioxidant enzyme gene *Cat* shows cell-type-specific 'decreasing gradual' (dark blue) expression in oligodendrocytes, OPCs, and vascular cell types across most subregions (Extended Data Fig. 4d). Several genes exhibited cell-type-specific gene and/or subregion-specific expression trajectories with age (Extended Data Fig. 4d). Gene expression can also be visualized directly on brain sections (Fig. 1i and Extended Data Fig. 4e) and for individual cell types (Supplementary Fig. 2), confirming the cell-type-specific and region-specific changes in gene expression. Using immunofluorescence staining, we validated the spatiotemporal levels of STAT1 in young, middle-aged, and old brains (Extended Data Fig. 2).

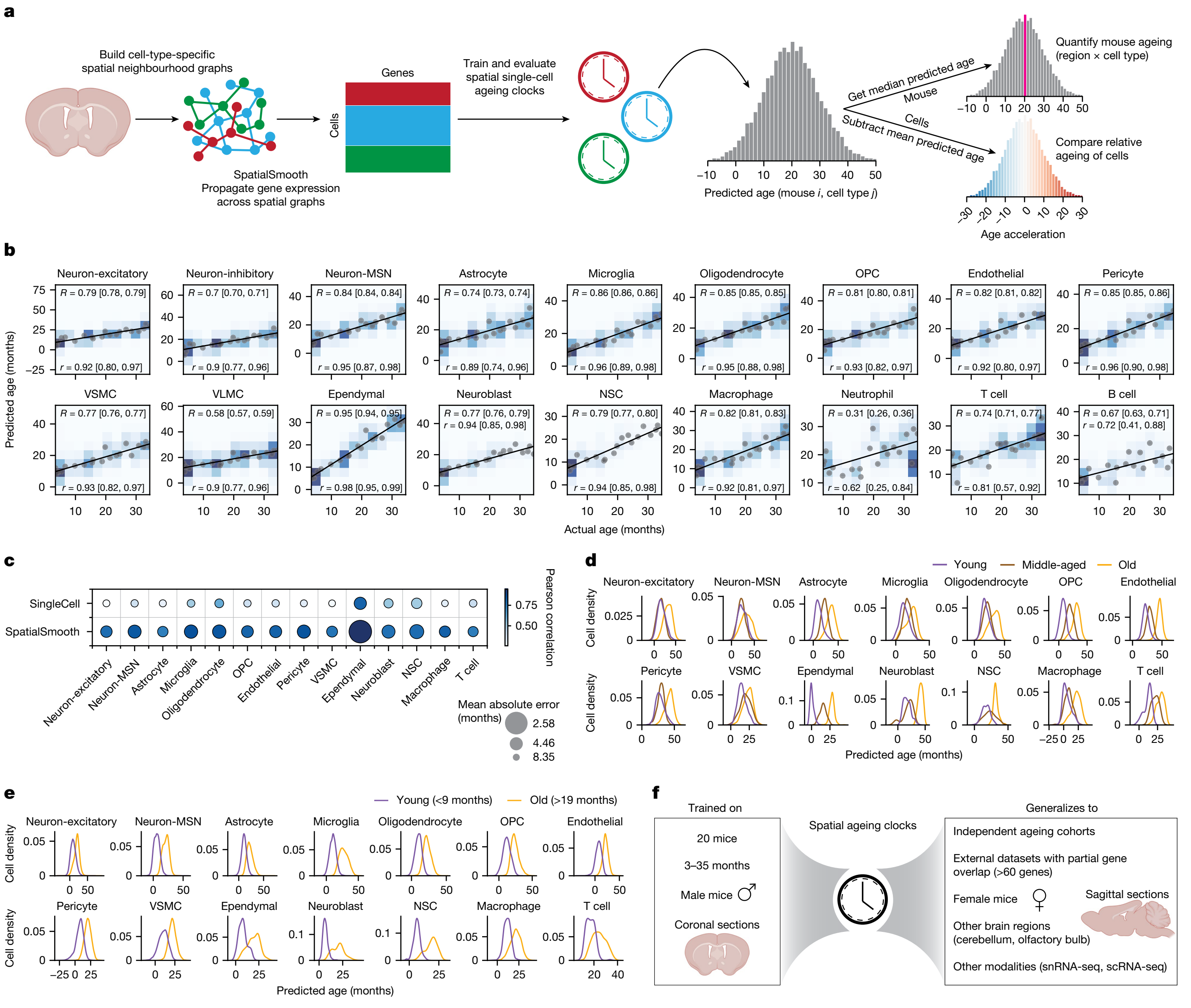

Fig. 2 | Spatial ageing clocks. a, Pipeline for building spatial ageing clocks from the coronal section dataset and using them to compare ageing across conditions or quantify the deviation (age acceleration) of a cell from its expected predicted age. **b**, Predicted age as a function of actual age, with predicted ages obtained by leaving out all cells from one mouse and training spatial ageing clocks on the remaining data to make predictions on the held-out cells and repeating this procedure for all mice. Heat map shows density of predicted ages, circles show median predicted age per mouse, and the line of best fit for the median predicted ages is shown in black. Pearson correlation between predicted age and actual age for all cells is reported as R (with values of $R > 0.7$ in bold), and the Pearson correlation between median predicted age and actual age for all mice is reported as r; 95% confidence intervals for correlations are shown in brackets. **c**, Dot plot comparing the performance of single-cell ageing clocks without spatial smoothing (SingleCell) with our spatial ageing clocks (SpatialSmooth). Dot colour corresponds to Pearson correlation and dot size is inversely related to mean absolute error between predicted age and actual age. **d**, Density of predicted ages in an external 140-gene MERFISH dataset consisting of 6 coronal sections from 3 mice (3, 19 and 25 months old). **e**, Density of predicted ages across the young (<9 months) and old (>19 months) sagittal section samples. **f**, Summary of the training data used to build the spatial ageing clocks and the generalization of spatial ageing clocks to different datasets. scRNA-seq, single-cell RNA-seq; snRNA-seq, single-nucleus RNA-seq.

Thus, our atlas provides a spatiotemporal transcriptomic view of brain ageing at single-cell resolution.

Spatial ageing clocks

To measure the biological age of individual cells, we trained machine learning models to predict mouse age from the spatially preprocessed gene expression data of each cell (hereafter 'spatial ageing clocks'). In the MERFISH gene panel, we included several genes with a causal role in ageing[28] (Methods and Supplementary Table 1), which is helpful for generating more biologically meaningful ageing clocks.

To preserve spatial information while maximizing the performance of single-cell ageing clocks, we developed a soft spatial pseudobulking procedure, referred to as SpatialSmooth. This method involves iterative smoothing of gene expression values along a spatial graph of neighbouring cells of the same cell type before training cell-type-specific ageing clock models on the smoothed single-cell transcriptomes (Fig. 2a; details in Methods). Ageing clocks developed using the SpatialSmooth method on the coronal section dataset yielded high performance ($R > 0.7$) across 14 of the 18 cell types, including very rare cell types such as T cells, NSCs and neuroblasts (Fig. 2b). Spatial ageing clock performance was generally robust to different parameter choices in

SpatialSmooth (Extended Data Fig. 5a) and was similar when trained and evaluated on the two independent cohorts in the coronal section dataset (Extended Data Fig. 5b,c). Spatial ageing clocks trained using SpatialSmooth substantially outperformed those trained directly on the spatial single-cell transcriptomes of the coronal section dataset (Fig. 2c). These spatial ageing clocks generally outperformed previous cell-type-specific transcriptomic ageing clocks[4] (Extended Data Fig. 5d and Supplementary Fig. 3), and could be generated for more cell types, even less common ones (for example, ependymal cells, macrophages, T cells and pericytes). For all downstream applications, we used the 14 high-performing spatial ageing clocks.

The number of genes automatically selected by each cell-type-specific spatial ageing clock was variable, ranging from 62 genes for T cells to 292 genes for astrocytes (Supplementary Fig. 4 and Supplementary Table 10). Spatial ageing clock genes with positive coefficients were enriched for many distinct biological processes (Extended Data Fig. 5e and Supplementary Table 11), whereas spatial ageing clock genes with negative coefficients were generally enriched for differentiation and development processes (Extended Data Fig. 5f and Supplementary Table 11).

Spatial ageing clocks exhibit better performance within the same cell type than across different cell types (Extended Data Fig. 5g). Within the same cell type, spatial ageing clocks generally produced accurate predicted ages across all subregions of the coronal brain sections (Extended Data Fig. 5h). Spatial ageing clocks trained on individual subregions also exhibited good performance (Methods, Extended Data Fig. 5i), and they could similarly generalize to the same cell types in other subregions of the coronal brain sections (Extended Data Fig. 5j).

We evaluated whether these spatial ageing clocks are generalizable to external datasets. Our spatial ageing clocks robustly separate three ages (young, middle-aged and old) on an independent MERFISH dataset of coronal brain sections generated using a panel of 140 genes[29] (Methods) (Fig. 2d, Supplementary Fig. 5a). The separation of the three ages in this external dataset was generally similar to that observed for cross-validation within the coronal section dataset (Fig. 2d and Supplementary Fig. 5b). Instances of reduced spatial ageing clock performance in this external dataset are probably linked to a combination of low gene overlap with our dataset (72 out of 300 genes), relatively small transcriptomic changes with age in certain cell types such as neurons[17,19], and low cell numbers for some cell types such as neuroblasts and NSCs. Notably, the spatial ageing clocks, which were trained on data from male mice, generalized to an external MERFISH dataset of coronal brain sections from female mice[17] (Extended Data Fig. 6a) and to a corresponding single-nuclei RNA-sequencing (RNA-seq) dataset from female mice[17] (Extended Data Fig. 6b).

Spatial ageing clocks, which were trained on cells from coronal brain sections, also generalized to sagittal brain sections, which include regions that are not present in coronal sections (for example, olfactory bulb and cerebellum) (Fig. 2e, Extended Data Fig. 6c,d and Supplementary Fig. 5c), and to a dissociated single-cell RNA-seq dataset of the entire brain containing additional brain regions from male mice (young and old)[5] (Extended Data Fig. 6e). Overall, spatial ageing clocks can robustly separate young and old cells across most cell types in all external datasets evaluated (statistical analysis in Supplementary Table 12).

Our spatial ageing clocks can generalize to independent cohorts of mice, to external spatial transcriptomics datasets with only partial gene overlap, across sex, across brain regions, and to other single-cell transcriptomics technologies (Fig. 2f).

Spatial ageing clocks record rejuvenation

Several interventions restore aspects of brain function in old age[30,31]. We explored whether spatial ageing clocks could provide a scalable way of assessing the effect of 'rejuvenating interventions' across different cell types and regions of the brain. To test this possibility, we generated additional MERFISH spatial transcriptomics datasets using coronal brain sections from young and old mice in response to two rejuvenating interventions: voluntary exercise and partial reprogramming (that is, cyclic in vivo expression of the Yamanaka factors *Oct4*, *Sox2*, *Klf4* and *Myc* (OSKM)) (Fig. 3a and Methods). We chose these two rejuvenating interventions because they are thought to affect many cell types and probably have different modes of action[32–35] (systemic for exercise versus cell-intrinsic for partial reprogramming).

The exercise intervention dataset yielded more than 900,000 cells, which clustered into 18 cell types (Fig. 3b and Extended Data Fig. 7a). The partial reprogramming intervention dataset yielded more than 1 million cells that clustered into 15 cell types (T cells, B cells and neutrophils were not identified, probably because of reduced infiltrating immune cells in this model[35]) (Fig. 3c and Extended Data Fig. 7b). The exercise and partial reprogramming interventions did not have a significant effect on cell-type proportion in old mice (Extended Data Fig. 7c,d), although the detection of such changes may be limited by the low sample size.

We applied our spatial ageing clocks to assess which brain cell types and regions exhibit the greatest transcriptomic rejuvenation (that is, exhibiting a younger predicted age with intervention than the control) by exercise and partial reprogramming.

Our spatial ageing clocks indicated that the transcriptomes of several cell types were rejuvenated by exercise, including endothelial cells (median rejuvenation of 4.9 months), pericytes (median rejuvenation of 3.4 months) and VSMCs (median rejuvenation of 4.7 months) (Fig. 3d,f and Supplementary Table 12). These strong rejuvenating effects on cells of the brain vasculature were present across multiple brain regions (except for the VEN) (Fig. 3f), consistent with a systemic effect of exercise. The strong response of the brain vasculature to exercise may be linked to exposure to circulating blood factors, which mediate some effects of exercise[30,36], and to generation of new blood vessels in the brain upon exercise[32,37]. Gene set enrichment analysis revealed that genes that were downregulated by exercise were significantly enriched for cell junction and focal adhesion processes in endothelial cells in the rejuvenated regions, but not in the VEN (Supplementary Table 13), consistent with the region-specific rejuvenation of endothelial cells by exercise. Neuroblasts also exhibited region-specific rejuvenation by exercise (Fig. 3f). Whereas neuroblasts are present in the VEN and adjacent regions such as the corpus callosum (CC), they only showed strong rejuvenation by exercise near the CC (Fig. 3f), perhaps because of the presence of specific growth factors in this region. Overall, exercise has a strong rejuvenating effect on the brain, consistent with previous studies[30,31], and this beneficial effect is particularly pronounced in brain vasculature cells and neuroblasts in specific brain regions.

Our spatial ageing clocks also revealed that the transcriptomes of a few cell types were rejuvenated by partial reprogramming, including NSCs (median rejuvenation of 2.7 months) and neuroblasts (median rejuvenation of 2.8 months) (Fig. 3e,g; statistical analysis in Supplementary Table 12), consistent with the restoration of neural progenitors by partial reprogramming[35]. In general, rejuvenation by partial reprogramming was weaker than rejuvenation by exercise (Supplementary Table 12). Ependymal cells exhibited region-specific rejuvenation near the CC but not in the VEN or near the STR (Fig. 3g). By contrast, other cell types (medium spiny neurons, microglia and glial cells) were prematurely aged across multiple brain regions in response to partial reprogramming (Fig. 3g). Thus, partial reprogramming may have both beneficial and detrimental effects on the brain, depending on the cell type.

Our spatial ageing clocks reveal the specific cell types and regions most affected by two different rejuvenating interventions, highlighting potentially complementary modes of rejuvenation.

Spatial ageing clocks record disease

We next applied our spatial ageing clocks to compare the effects of interventions and diseases that are known to be detrimental to the brain.

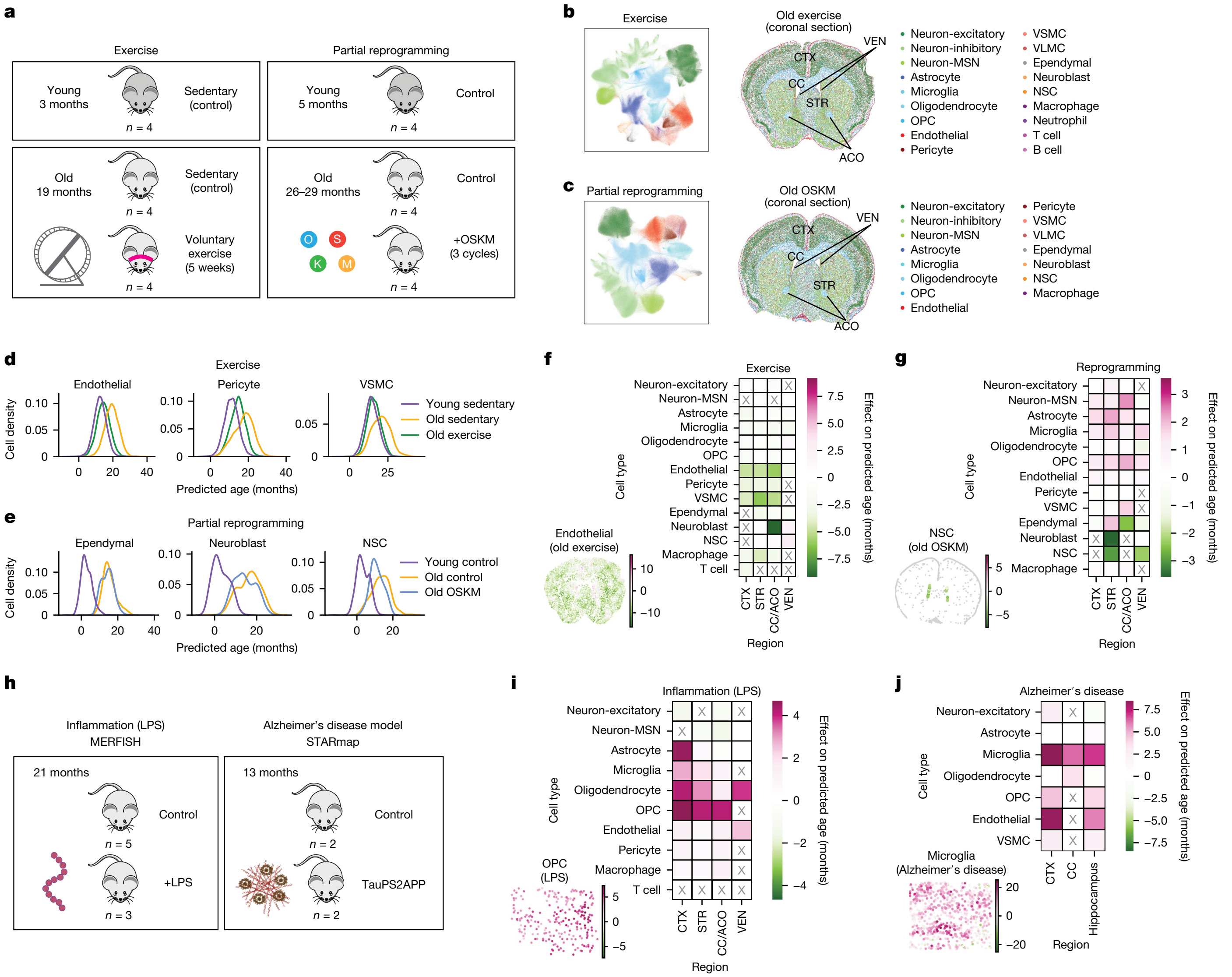

Fig. 3 | Effects of rejuvenation strategies, inflammation and disease on spatial single-cell ageing. **a**, Experimental design for exercise and whole-body partial reprogramming as rejuvenating interventions. **b**,**c**, UMAP visualization of all cells coloured by cell type (left) and visualization under spatial coordinates for all cells in one representative coronal section (right) from the exercise experiment (**b**) and from the whole-body partial reprogramming experiment (**c**). Brain regions are annotated. **d**,**e**, Density of predicted ages across different experimental conditions for spatial ageing clocks corresponding to three cell types rejuvenated by exercise (**d**) and three cell types rejuvenated by whole-body partial reprogramming (**e**). **f**,**g**, Heat maps showing the effect of rejuvenating interventions on predicted age for different cell types and regions, measured as the difference in median predicted age between intervention and control conditions for old mice, under exercise (**f**) and whole-body partial reprogramming (**g**). Cell types and regions with insufficient numbers of cells (<50) are denoted by 'X'. Insets show spatial visualization of cells in an example intervention sample coloured by their difference from the median predicted age in the control condition, with endothelial cells (**f**) and NSCs (large dots) and VLMCs (small grey dots) (**g**). **h**, Schematic of cohorts from publicly available spatial transcriptomics datasets for systemic inflammatory challenge by LPS injection[17] and for the Alzheimer's disease model[22]. **i**,**j**, Heat maps showing the effect on predicted age for different cell types and regions, measured as the difference in median predicted age between intervention and control conditions for systemic inflammatory challenge by LPS injection (**i**) and the Alzheimer's disease model (**j**). Cell types and regions with insufficient numbers of cells (<50) are denoted by 'X'. Insets show spatial visualization of cells in an example intervention sample coloured by their difference from the median predicted age in the control condition, with OPCs (**i**) and microglia (**j**).

We analysed a publicly available MERFISH spatial transcriptomics dataset of brain sections containing parts of the CTX, STR and CC from mice subjected to systemic inflammatory challenge following injection of lipopolysaccharide (LPS) as a model of accelerated ageing[17] (Fig. 3h). Spatial ageing clocks revealed that several cell types, including glial cells (astrocytes, oligodendrocytes and OPCs) and microglia exhibited accelerated ageing in response to LPS (Fig. 3i and Extended Data Fig. 8a). The effect of LPS on the predicted age of astrocytes was highly specific to the cortical regions, whereas the effect of LPS on oligodendrocytes, OPCs and microglia was present across multiple brain regions (Fig. 3i and Supplementary Table 12). The accelerated transcriptomic ageing of oligodendrocytes and OPCs may be driven by their upregulated inflammation state under LPS condition (Extended Data Fig. 8b), in line with reported upregulation of inflammatory (activation) states of astrocytes and microglia in response to LPS[17].

We also analysed a publicly available STARmap spatial transcriptomic dataset on brain sections containing the hippocampus from mouse models of Alzheimer's disease (triple-transgenic TauPS2APP[22]) (Fig. 3h). Spatial ageing clocks revealed that most cell types (microglia, neurons and cells of the brain vasculature) exhibited accelerated transcriptomic ageing in the Alzheimer's disease model across several brain regions (Fig. 3j, Extended Data Fig. 8c and Supplementary Table 12).

The strongly accelerated transcriptomic ageing of microglia in Alzheimer's disease is consistent with the enrichment of disease-associated microglia in this model[22].

For both LPS and Alzheimer's disease models, application of our spatial ageing clocks to brain sections from younger mice revealed similar patterns in accelerated transcriptomic ageing of cell types, but the effects were generally more pronounced in older mice (Extended Data Fig. 8d,e). These observations suggest that older mice may be more susceptible to the detrimental effects of inflammation and disease.

Demyelination injury in the brain (including in the context of multiple sclerosis) has been linked to accelerated brain ageing in humans[38–40]. We applied our spatial ageing clocks to publicly available datasets on two different multiple sclerosis mouse models—an in situ sequencing dataset of global demyelination upon experimental autoimmune encephalomyelitis[23] (EAE) and a MERFISH dataset of localized demyelination injury[21]. Spatial ageing clocks revealed accelerated transcriptomic ageing for most cell types, notably microglia, in the global EAE model compared with control mice across all brain regions (Extended Data Fig. 8f). By contrast, for localized demyelination injury, the greatest age acceleration was spatially restricted to the site of injury for multiple cell types (Extended Data Fig. 8g), suggesting that localized interventions can have a strong and specific effect.

Thus, spatial ageing clocks reveal cell-type-specific and regional effects of inflammation, neurodegenerative disease and demyelination injury on the brain, providing a high-resolution foundation for developing targeted interventions.

Cell proximity effects of brain ageing

We next considered the potential influence of some cells on the age of neighbouring cells. Using spatial ageing clocks, we quantified the spatial proximity effect of a given 'effector' cell type on the deviation from the expected predicted age ('age acceleration') of a 'target' cell type (cell proximity effect analysis is described in detail in Methods) (Fig. 4a and Extended Data Fig. 9a). After computing the proximity effect for all combinations of effector and target cell types, we identified 214 distinct cell–cell proximity effects (Fig. 4b and Supplementary Table 14). Target cells that were most affected by any effector cell include cells of the VEN (ependymal cells, NSCs and neuroblasts), pericytes and OPCs (Extended Data Fig. 9b). The proximity effects of effector cell types were generally similar across different brain regions, although microglia had a stronger pro-ageing effect on several target cell types in the CC/ACO (Extended Data Fig. 9c).

We were particularly interested in effector cells with the strongest global effect on their neighbours. Notably, T cells had the strongest pro-ageing average proximity effect (Fig. 4c and Extended Data Fig. 9d), and this influence was especially clear on oligodendrocytes and pericytes (Fig. 4b). The pro-ageing proximity effect of T cells (which are mostly cytotoxic in the ageing brain; Supplementary Fig. 6a) was more pronounced in older mice (Extended Data Fig. 9e). Surprisingly, NSCs had the strongest pro-rejuvenating average proximity effect (Fig. 4c and Extended Data Fig. 9d), which was particularly evident on OPCs and pericytes (Fig. 4b). The pro-rejuvenating proximity effect of NSCs was more pronounced in younger mice (Extended Data Fig. 9e).

The effects of T cells and NSCs on nearby cells are robust. T cells remained the most pro-ageing effector cell type and NSCs remained the most pro-rejuvenating effector cell type even when using different definitions of cell proximity effect (Supplementary Fig. 6b,c), when restricting to independent cohorts of the coronal section dataset (Supplementary Fig. 6d,e), and when using other types of spatial ageing clocks (see Methods, Supplementary Fig. 6f,g). Notably, we verified that on average, T cells were the most pro-ageing cell type and NSCs were the most pro-rejuvenating cell type in multiple external datasets (Extended Data Fig. 9f and Supplementary Table 15).

The observed proximity effects are unlikely to be confounded by changes in cell-type proportion with age. Randomly permuting the spatial locations of all cells within subregions of each sample resulted in the complete loss of the proximity effects of all effector cell types (Fig. 4c), suggesting that cell-type proportion or regional heterogeneity do not influence the magnitude of proximity effects. We also showed that these proximity effects are unlikely to be confounded by spillover of transcripts between nearby effector and target cells (Supplementary Figs. 7 and 8a–c and Methods).

As expected, the proximity effects of T cells and NSCs on neighbouring cells decreased in magnitude over increasing distance between effector and target cells (Extended Data Fig. 9g). Notably, however, the pro-ageing effect of T cells on nearby cells generally persisted over longer distances than the pro-rejuvenating effect exerted by NSCs (Extended Data Fig. 9g and Supplementary Fig. 8d), perhaps indicating that longer-range pro-ageing T cell effects could be propagated by more diffusible factors or cascades of events (for example, successive inflammation of oligodendrocytes).

We next explored whether T cells have a pro-ageing effect on neighbouring cells or are attracted to already aged and inflamed cells (for example, activated microglia[41]). To distinguish between these possibilities, we selected the most activated microglia and inflamed oligodendrocytes on the basis of expression of activation and inflammation signatures respectively (Methods). We observed similar activation/inflammation signature levels between the most activated microglia and inflamed oligodendrocytes that were near or far from T cells (Extended Data Fig. 10a), although activated microglia and inflamed oligodendrocytes tended to be spatially closer than other cell types to T cells (Extended Data Fig. 10b,c). Crucially, we observed that T cells still had strong pro-ageing proximity effects on oligodendrocytes or microglia even after controlling for activation and inflammation status (Extended Data Fig. 10d). Together, these results suggest that T cells promote the ageing of nearby cells, independent of their activation/inflammation state.

We also interrogated whether NSCs have a pro-rejuvenating effect on neighbouring cells or whether cells near NSCs mostly originate from newborn cells and would therefore be predicted to be younger. We compared the NSC proximity effect across differentiated cell types in the NSC lineage (astrocytes and oligodendrocytes) and differentiated cell types not in the NSC lineage (microglia, endothelial cells and pericytes) (Extended Data Fig. 10e). NSCs exerted similarly strong pro-rejuvenating effects on all target cell types, including those from a different cell lineage altogether, suggesting that the NSC proximity effect is not limited to newborn cells in the NSC lineage and extends to other cells (Extended Data Fig. 10e).

Finally, we tested whether these proximity effects can be modulated by interventions to rejuvenate the brain. Using our spatial transcriptomics dataset on exercise (see Fig. 3a), we first confirmed that the spatial pro-ageing proximity effect of T cells was higher in old sedentary mice than young sedentary mice, and that the pro-rejuvenating effect of NSCs was less pronounced in old mice (Extended Data Fig. 11a,b). Of note, the pro-ageing proximity effect of T cells was reduced in old mice when subjected to voluntary exercise (Extended Data Fig. 11a). The NSC proximity effect was shifted in a rejuvenating manner by voluntary exercise in old mice (Extended Data Fig. 11b). This strong shift in the pro-rejuvenating NSC proximity effect with exercise occurs in the absence of intrinsic rejuvenation of NSCs by exercise (see Fig. 3f), suggesting that proximity effects can provide a complementary perspective on intervention outcomes. By contrast, we did not observe a substantial influence of partial reprogramming on spatial proximity effects (Extended Data Fig. 11c), perhaps because of the cell-intrinsic nature of this intervention. Thus, the pro-ageing proximity effects of T cells and the pro-rejuvenating proximity effects of NSCs can be modulated by rejuvenating interventions such as exercise.

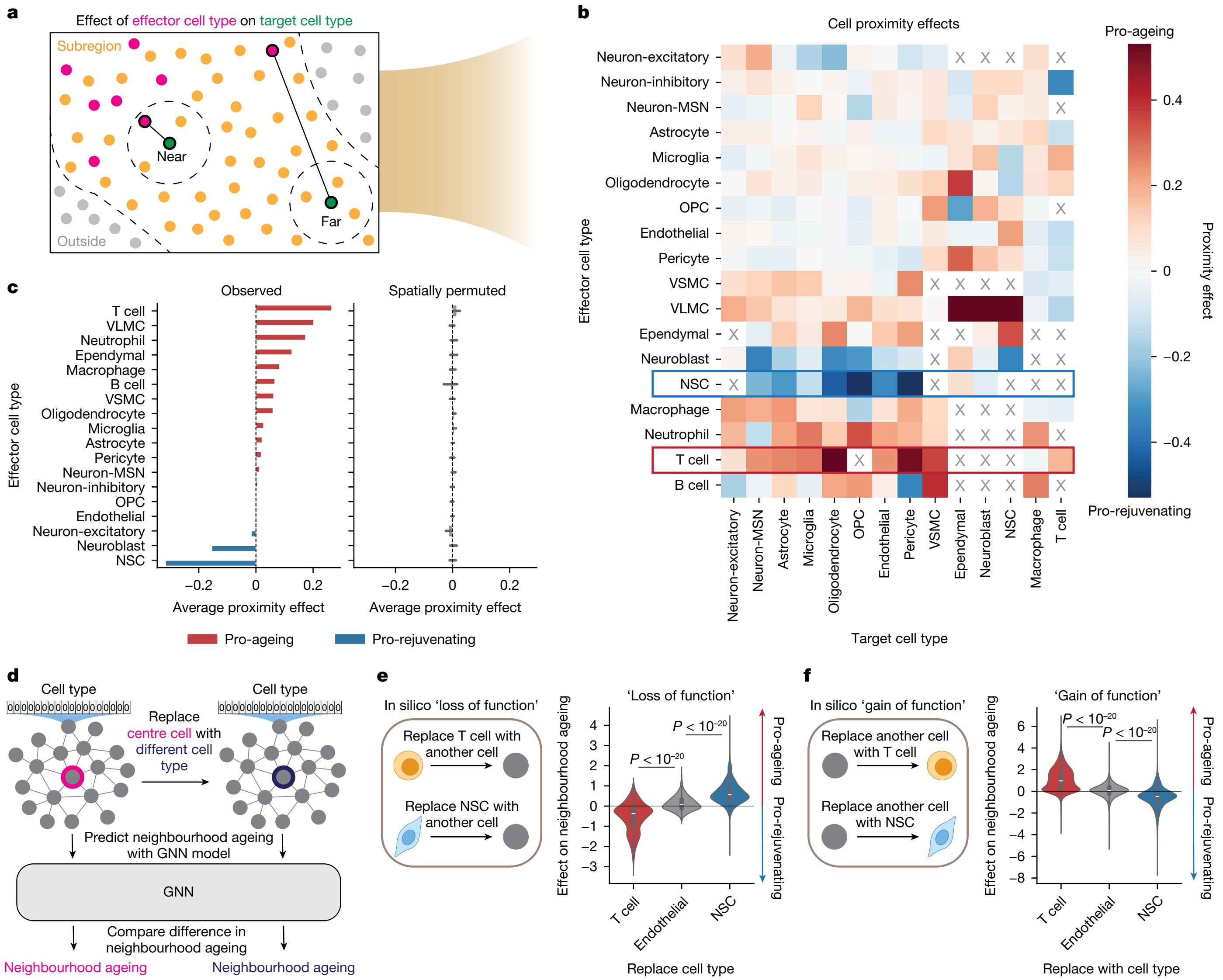

Fig. 4 | Proximity effects of cells on neighbouring cells during ageing and rejuvenation. a, Matching procedure for determining 'near' and 'far' target cells to compute the proximity effect of effector cells on the age acceleration of target cells. **b**, Heat map showing the proximity effect for different cell-type proximity relationships. Columns show the 14 target cell types with high-performing spatial ageing clocks. Proximity relationships for which there are insufficient cell pairings (<50) to compute a proximity effect are denoted by 'X'. Colour bar is trimmed at top 2% absolute proximity effect values. **c**, Average proximity effect for a given effector cell type on all other target cell types ranked from most pro-ageing to most pro-rejuvenating (left) and median average proximity effects of effector cell types computed after spatial permutation of all cells within subregions across each section (right). Error bars show 95% confidence interval across 20 spatial permutations. **d**, Scheme for in silico cell-type perturbation experiments using GNN models trained to predict neighbourhood ageing from local cell graphs. **e**,**f**, Effect of perturbing effector cell types on neighbourhood ageing. **e**, Perturbations that replace the effector cell type with another cell type (loss of function) for $n = 1{,}611$ T cell, $n = 1{,}623$ endothelial cell and $n = 2{,}833$ NSC local cell graph perturbations. **f**, Perturbations that replace another cell type with the effector cell type (gain of function) for $n = 26{,}685$ T cell, $n = 26{,}675$ endothelial cell and $n = 25{,}469$ NSC local cell graph perturbations. The line indicates the median, the inner box corresponds to 25th and 75th percentiles, and the whiskers span up to 1.5 times the interquartile range of the effects. Two-sided Mann–Whitney test.

Deep graph modelling of proximity effects

A key step in understanding the role of specific cells on their neighbours is to study perturbations. To test the effect of in silico cell-type perturbations involving T cells and NSCs on the ageing of nearby cells, we used a deep learning approach. We trained a graph neural network (GNN) model on local cell graphs extracted around centre cells to predict neighbourhood ageing, defined as the average age acceleration of all nearby cells, using only the cell type and graph connectivity as features (Fig. 4d and Methods). Using this GNN model, we performed both 'loss-of-function' and 'gain-of-function' in silico manipulations by permuting the cell type of the centre cell and measuring the effect on neighbourhood ageing. Replacing a T cell with another cell (loss-of-function experiment) led to decreased neighbourhood ageing (Fig. 4e), whereas replacing an NSC with another cell resulted in increased neighbourhood ageing (Fig. 4e). Conversely, replacing any cell with a T cell (gain-of-function experiment) led to increased neighbourhood ageing (Fig. 4f), whereas replacing any cell with an NSC resulted in decreased neighbourhood ageing (Fig. 4f). We verified that in both setups, the replacement or addition of a neutral cell type (endothelial cells) did not substantially affect the neighbourhood ageing (Fig. 4e,f). Together, these in silico perturbations confirm that T cells have a pro-ageing effect on their neighbours, whereas NSCs have a pro-rejuvenating effect on their neighbours.

Potential mediators of proximity effects

We next investigated potential mediators of the pro-ageing effect of T cells or the pro-rejuvenating effect of NSCs on nearby cells. We assessed global changes in gene expression in the more pro-ageing T cells or the more pro-rejuvenating NSCs and in their neighbours. To augment the 300 genes measured through MERFISH to more 12,000 genes, we used TISSUE[29] with single-cell RNA-seq datasets to perform uncertainty-aware spatial gene expression imputation (Extended Data Fig. 12a–c and Methods). We first conducted unbiased differential gene expression analysis using all imputed genes and then did targeted comparisons of imputed gene signatures or individual genes related to the most enriched signatures (Methods). This approach augments our limited gene panel to screen for potential mediators of the T cell and NSC proximity effect.

T cell effect via interferon signalling

Our unbiased differential gene expression analysis on more than 12,000 genes revealed that cells near T cells have increased expression of genes associated with viral immune response (Fig. 5a), perhaps in response to interferon signalling. Indeed, T cells with a greater pro-ageing proximity effect exhibited increased expression of imputed gene signature for 'positive regulation of type II interferon production' compared with T cells with less pro-ageing proximity effect ($P = 0.026$, two-sided TISSUE t-test, Fig. 5b). Consistently, the more pro-ageing T cells are more activated than their less pro-ageing counterparts (Extended Data Fig. 12d), with T cell activation being linked to increased interferon gamma (IFNγ) production[42–44]. T cells with greater pro-ageing proximity effect did not upregulate other candidate inflammatory production pathways, such as 'positive regulation of type I interferon production' ($P = 0.14$, two-sided TISSUE t-test), 'positive regulation of tumor necrosis factor production' ($P = 0.47$, two-sided TISSUE t-test), and 'interleukin-6 production' ($P = 0.22$, two-sided TISSUE t-test). Consistent with the increased production of IFNγ pathway in effector T cells, target cells near T cells exhibited concomitant increase in expression of IFNγ response genes (*Bst2*, $P = 2.9\times10^{-14}$; *Stat1*, $P = 4.4\times10^{-5}$; two-sided Mann–Whitney tests) (Fig. 5c). Target cells near T cells also showed increased expression of imputed gene signature for 'cellular response to type II interferon' ($P = 2.3\times10^{-4}$, two-sided TISSUE t-test) compared with target cells far from T cells after matching by cell type and subregion (Fig. 5c).

We next explored whether conditions that lower IFNγ in T cells modulate their proximity effects. We used the MERFISH dataset on LPS injection[17], as LPS is known to dampen T cell activation and IFNγ secretion[45–47], among other effects. In line with published findings, we observed significantly reduced scaled log-normalized expression of *Ifng* in the LPS condition compared with control ($P < 10^{-20}$, two-sided Mann–Whitney U-test). Notably, the LPS condition was associated with an attenuation of the T cell pro-ageing proximity effect (Extended Data Fig. 12e). Together with the unbiased gene expression analysis, these data suggest a role for IFNγ in mediating the T cell proximity effect.

For experimental validation, we performed immunofluorescence staining on coronal brain sections of old (28 months) male mice using antibodies to the T cell marker CD3 and the interferon-response marker STAT1, a marker that is also linked with inflammation-dependent ageing[48] (Methods). We observed significantly higher STAT1 intensity in cells near T cells (CD3$^+$ cells) compared with cells that were not near T cells, across the CC ($P = 0.016$, two-sided Mann–Whitney U-test), CTX ($P = 0.0078$, two-sided Mann–Whitney U-test) and VEN ($P = 0.0078$, two-sided Mann–Whitney U-test) and a trending increase in the STR ($P = 0.078$, two-sided Mann–Whitney U-test) (Fig. 5d,e and Extended Data Fig. 12f). These findings experimentally validate that the T cell proximity effect is associated with upregulated interferon response in nearby cells and raise the possibility that interferon signalling might mediate the pro-ageing proximity effect of T cells.

Mediators of the pro-rejuvenating effect of NSCs

Our unbiased differential gene expression analysis on more than 12,000 genes revealed that cells near NSCs exhibited upregulation of genes associated with endocytic pathways and lipid metabolism (Fig. 5f). We therefore investigated components of the NSC secretome with known effects on lipid metabolism or endocytosis, which include extracellular vesicles (exosomes)[49–51] and growth factors[52–54]. NSCs with greater pro-rejuvenating proximity effects exhibited increased expression of imputed gene signatures for 'exocytosis' ($P = 0.014$, two-sided TISSUE t-test) and 'exosomal secretion' ($P = 0.044$, two-sided TISSUE t-test), increased expression of the exosome marker *Cd9* ($P = 0.019$, two-sided Mann–Whitney test), and trending increased expression of the growth factor gene *Vegfa* ($P = 0.059$, two-sided Mann–Whitney test), which is the only gene encoding an NSC-secreted growth factor in the MERFISH panel (Fig. 5g). Exosomes have been implicated in neurogenesis[55] and could mediate the pro-rejuvenating effect of NSCs on their neighbours. The increase in *Vegfa* is notable in light of its effect on the maintenance of neurogenic niche cells[56–58] and on organismal longevity[59]. NSCs with greater pro-rejuvenating proximity effect also showed upregulation of pathways associated with cell proliferation and DNA replication (Extended Data Fig. 12g), which can be regulated by NSC-derived exosomes[60]. Concomitantly, cells near NSCs exhibited increased expression of imputed gene signatures for cell import and endocytosis ('caveolin-mediated endocytosis', $P = 1.9 \times 10^{-5}$; 'receptor-mediated endocytosis', $P = 7.2 \times 10^{-3}$; 'import across plasma membrane', $P = 0.017$; two-sided TISSUE t-test) and cellular response to multiple growth factors (VEGF, $P = 5.5 \times 10^{-4}$; FGF, $P = 3.3 \times 10^{-13}$; TGFβ1, $P = 7.0 \times 10^{-10}$; two-sided TISSUE t-tests) compared with cells far from NSCs, after matching by cell type and subregion (Fig. 5h). Cells near NSCs also showed increased expression of a signature for NADH metabolism 'NADH metabolic process' ($P = 1.5 \times 10^{-9}$, two-sided TISSUE t-test), which is linked to fatty acid oxidation metabolism and more youthful brain states[61–63] (Fig. 5h).

We experimentally validated that the NSC proximity effect is associated with exosomes in NSCs and upregulated fatty acid oxidation in nearby cells. We performed immunofluorescence staining on brain sections of young (3.5 months) male mice using antibodies to the NSC marker S100A6[64], the exosome marker CD9[65] and the fatty acid oxidation marker CPT1A[66,67], a marker that is linked to improved cell function[68]. NSCs (S100A6$^+$ cells) had significantly higher CD9 intensity than other cell types ('non-NSCs') in the VEN of young mice ($P = 0.0079$, two-sided Mann–Whitney U-test) (Fig. 5i–k and Extended Data Fig. 12h). Of note, cells near NSCs exhibited significantly higher CPT1A intensity than cells that were not near NSCs in the VEN ($P = 0.016$, two-sided Mann–Whitney U-test) (Fig. 5i,j,l and Extended Data Fig. 12h). The CD9 intensity of NSCs and the CPT1A intensity in nearby cells were positively correlated (Pearson correlation $r = 0.35$, Spearman correlation $\rho = 0.36$) (Fig. 5m). These experimental results support an association between increased exosome marker intensity in NSCs and upregulated fatty acid oxidation in nearby cells and raise the possibility that these changes might mediate part of the pro-rejuvenating proximity effect of NSCs.

Our results suggest the following model (Extended Data Fig. 12i): T cells have a strong pro-ageing effect on nearby cells and infiltrate the brain during ageing. These T cells express IFNγ[3,21,69], which may act on nearby cells in a pro-ageing manner by inducing inflammatory responses. By contrast, NSCs have a strong pro-rejuvenating effect on nearby cells and decline in number with age. NSCs may secrete growth factors and exosomes that could act on nearby cells in a pro-rejuvenating manner, in part by modulating lipid metabolism.

Discussion

Our study provides a high-resolution spatiotemporal profiling of the ageing mouse brain, which enables tracking of gene expression

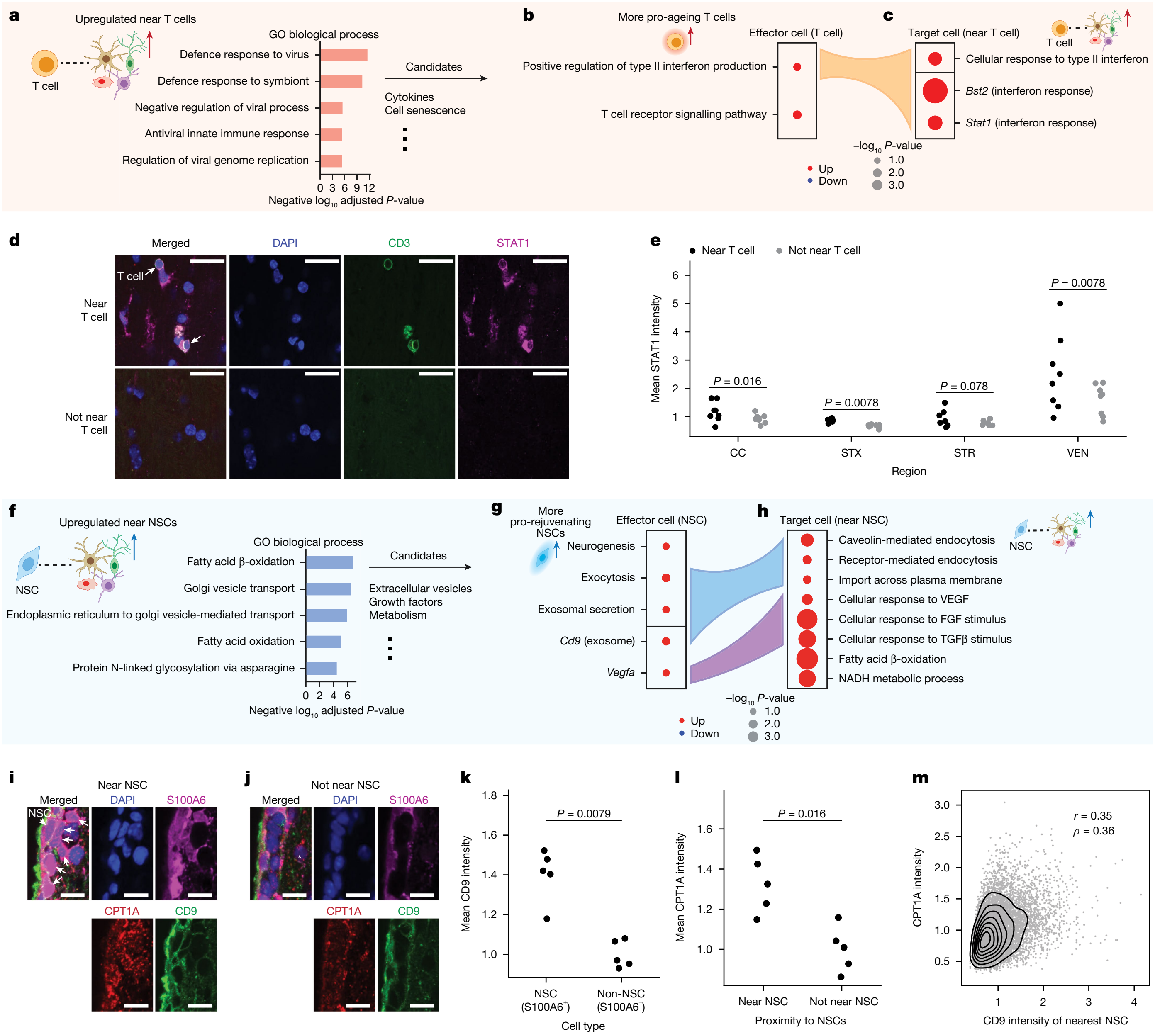

Fig. 5 | Molecular pathways underlying T cell and NSC proximity effects. **a**, Most enriched Gene Ontology (GO) biological processes for significantly upregulated genes in cells near T cells compared with cells that are far from T cells. *P* values from EnrichR pathway enrichment analysis. **b**,**c**, Key GO biological process signatures (sum of imputed expression across all genes in set) and genes in the MERFISH panel for imputed signatures in more pro-ageing T cells compared with less pro-ageing T cells (**b**) and imputed signatures and measured genes (*Bst2*, *Stat1*) in cells near T cells compared with cells that are far from T cells (**c**). Dot size corresponds to $-\log_{10} P$ value (TISSUE two-sided *t*-test for imputed signatures and two-sided Mann–Whitney *U*-test for measured log-normalized gene expression). **d**, Immunofluorescence images from the same coronal brain section of an old (28 months) male mouse highlighting increased STAT1 labelling in cells near T cells (CD3$^+$) (top row) compared with cells that are not near T cells (bottom row) in the CC. Scale bars, 20 µm. **e**, Mean STAT1 intensity of cells near T cells compared with cells that are not near T cells across 4 brain regions for independent old (28 months) male mice ($n = 7$–8) across 2 experiments (Methods). Two-sided Wilcoxon signed-ranked test. **f**, Same as **a** but for cells near NSCs compared with cells that are far from NSCs. **g**,**h**, Same as **b**,**c** except for imputed signatures and measured genes (*Cd9* and *Vegfa*) in more pro-rejuvenating NSCs compared with less pro-rejuvenating NSCs (**g**) and imputed signatures in cells near NSCs compared with cells far from NSCs (**h**). **i**,**j**, Immunofluorescence images from a young (3.5 months) male mouse highlighting increased CPT1A labelling in cells near NSCs (S100A6$^+$) with high CD9 fluorescence (**i**) compared with cells not near NSCs (**j**) in the VEN. Arrows indicate NSCs and stars indicate cells that are not near NSCs. Scale bars, 10 µm. **k**, Mean CD9 intensity of NSCs (S100A6$^+$) compared with non-NSCs (S100A6$^-$) for independent young (3.5 months) male mice ($n = 5$) across one experiment (Methods). Two-sided Mann–Whitney *U*-test. **l**, Mean CPT1A intensity of cells near NSCs compared with cells that are not near NSCs for independent mice ($n = 5$) (Methods). Two-sided Mann–Whitney *U*-test. **m**, Scatter plot with density contours of CPT1A intensity as a function of CD9 intensity of nearest NSC (S100A6$^+$) for all cells near NSCs. Pearson (*r*) and Spearman (*ρ*) correlations are shown.

trajectories during ageing in different regions and cell types. We use this dataset to generate spatial ageing clocks and, in turn, quantify the region-specific and cell-type-specific effects of different rejuvenating interventions or disease models. Spatial ageing clocks should be helpful to rapidly assess the effect of experimental interventions on ageing and other temporal processes at spatial and single-cell resolution. Our flexible machine learning framework for building spatial ageing clocks and modelling cell proximity effects could be adapted to other tissues and species. The development of new statistical methodologies or experimental approaches to enhance the causality and dimensionality of ageing clock predictions could further broaden the usage of these models.

We use these spatial ageing clocks here to quantify cell proximity effects. Systematic profiling with a larger gene panel and deeper imaging for spatial transcriptomics may enable the segmentation of long-range neuronal projections to provide greater resolution on the proximity effects of some cell types, particularly neurons. Although we identify potential mediating pathways for cell proximity effects, deeper and more functional studies with specific cellular readouts will be needed to provide a better understanding of the mode of action and its biological effects. For example, different types of T cells can have beneficial or detrimental effects on the brain[3,21,41,69–79], particularly in response to injury or disease[3,21,41,70,72–74,79]. Disentangling the proximity effect of heterogeneous T cell populations in different regions could further enrich our understanding of how T cells influence brain ageing. Finally, it will be interesting to determine how some newborn cells in the brain (NSCs and neuroblasts) exert their pro-rejuvenating effects on their neighbours, whether extracellular vesicles are involved, and whether this could be implemented in other regions that do not contain stem cells. Ultimately, broader investigation into proximity effects and their mediators will be critical and may lead to new therapeutic strategies for improving brain resilience during ageing.

Online content

Any methods, additional references, Nature Portfolio reporting summaries, source data, extended data, supplementary information, acknowledgements, peer review information; details of author contributions and competing interests; and statements of data and code availability are available at https://doi.org/10.1038/s41586-024-08334-8.

1. Hou, Y. et al. Ageing as a risk factor for neurodegenerative disease. *Nat. Rev. Neurol.* **15**, 565–581 (2019).
2. Mattson, M. P. & Arumugam, T. V. Hallmarks of brain aging: adaptive and pathological modification by metabolic states. *Cell Metab.* **27**, 1176–1199 (2018).
3. Dulken, B. W. et al. Single-cell analysis reveals T cell infiltration in old neurogenic niches. *Nature* **571**, 205–210 (2019).
4. Buckley, M. T. et al. Cell-type-specific aging clocks to quantify aging and rejuvenation in neurogenic regions of the brain. *Nat. Aging* **3**, 121–137 (2023).
5. Ximerakis, M. et al. Single-cell transcriptomic profiling of the aging mouse brain. *Nat. Neurosci.* **22**, 1696–1708 (2019).
6. Hajdarovic, K. H. et al. Single-cell analysis of the aging female mouse hypothalamus. *Nat. Aging* **2**, 662–678 (2022).
7. Almanzar, N. et al. A single-cell transcriptomic atlas characterizes ageing tissues in the mouse. *Nature* **583**, 590–595 (2020).
8. Kiss, T. et al. Single-cell RNA sequencing identifies senescent cerebromicrovascular endothelial cells in the aged mouse brain. *GeroScience* **42**, 429–444 (2020).
9. Mrdjen, D. et al. High-dimensional single-cell mapping of central nervous system immune cells reveals distinct myeloid subsets in health, aging, and disease. *Immunity* **48**, 380–395.e6 (2018).
10. Kearns, N. A. et al. Dissecting the human leptomeninges at single-cell resolution. *Nat. Commun.* **14**, 7036 (2023).
11. Hammond, T. R. et al. Single-cell RNA sequencing of microglia throughout the mouse lifespan and in the injured brain reveals complex cell-state changes. *Immunity* **50**, 253–271.e6 (2019).
12. Artegiani, B. et al. A single-cell RNA sequencing study reveals cellular and molecular dynamics of the hippocampal neurogenic niche. *Cell Rep.* **21**, 3271–3284 (2017).
13. Kalamakis, G. et al. Quiescence modulates stem cell maintenance and regenerative capacity in the aging brain. *Cell* **176**, 1407–1419.e14 (2019).
14. Su, Y. et al. A single-cell transcriptome atlas of glial diversity in the human hippocampus across the postnatal lifespan. *Cell Stem Cell* **29**, 1594–1610.e8 (2022).
15. Zhou, Y. et al. Molecular landscapes of human hippocampal immature neurons across lifespan. *Nature* **607**, 527–533 (2022).
16. Moses, L. & Pachter, L. Museum of spatial transcriptomics. *Nat. Methods* **19**, 534–546 (2022).
17. Allen, W. E., Blosser, T. R., Sullivan, Z. A., Dulac, C. & Zhuang, X. Molecular and spatial signatures of mouse brain aging at single-cell resolution. *Cell* **186**, 194–208.e18 (2023).
18. Kiss, T. et al. Spatial transcriptomic analysis reveals inflammatory foci defined by senescent cells in the white matter, hippocampi and cortical grey matter in the aged mouse brain. *GeroScience* **44**, 661–681 (2022).
19. Hahn, O. et al. Atlas of the aging mouse brain reveals white matter as vulnerable foci. *Cell* **186**, 4117–4133.e22 (2023).
20. Chen, K. H., Boettiger, A. N., Moffitt, J. R., Wang, S. & Zhuang, X. Spatially resolved, highly multiplexed RNA profiling in single cells. *Science* **348**, aaa6090 (2015).
21. Androvic, P. et al. Spatial transcriptomics-correlated electron microscopy maps transcriptional and ultrastructural responses to brain injury. *Nat. Commun.* **14**, 4115 (2023).
22. Zeng, H. et al. Integrative in situ mapping of single-cell transcriptional states and tissue histopathology in a mouse model of Alzheimer's disease. *Nat. Neurosci.* **26**, 430–446 (2023).
23. Kukanja, P. et al. Cellular architecture of evolving neuroinflammatory lesions and multiple sclerosis pathology. *Cell* **187**, 1990–2009.e19 (2024).
24. Zhang, M. et al. Spatially resolved cell atlas of the mouse primary motor cortex by MERFISH. *Nature* **598**, 137–143 (2021).
25. Zhang, M. et al. Molecularly defined and spatially resolved cell atlas of the whole mouse brain. *Nature* **624**, 343–354 (2023).
26. Yao, Z. et al. A high-resolution transcriptomic and spatial atlas of cell types in the whole mouse brain. *Nature* **624**, 317–332 (2023).
27. Lein, E. S. et al. Genome-wide atlas of gene expression in the adult mouse brain. *Nature* **445**, 168–176 (2007).
28. de Magalhães, J. P. & Toussaint, O. GenAge: a genomic and proteomic network map of human ageing. *FEBS Lett.* **571**, 243–247 (2004).
29. Sun, E. D., Ma, R., Navarro Negredo, P., Brunet, A. & Zou, J. TISSUE: uncertainty-calibrated prediction of single-cell spatial transcriptomics improves downstream analyses. *Nat. Methods* **21**, 444–454 (2024).
30. Bieri, G., Schroer, A. B. & Villeda, S. A. Blood-to-brain communication in aging and rejuvenation. *Nat. Neurosci.* **26**, 379–393 (2023).
31. Navarro Negredo, P., Yeo, R. W. & Brunet, A. Aging and rejuvenation of neural stem cells and their niches. *Cell Stem Cell* **27**, 202–223 (2020).
32. Liu, L. et al. Exercise reprograms the inflammatory landscape of multiple stem cell compartments during mammalian aging. *Cell Stem Cell* **30**, 689–705.e4 (2023).
33. Horowitz, A. M. et al. Blood factors transfer beneficial effects of exercise on neurogenesis and cognition to the aged brain. *Science* **369**, 167–173 (2020).
34. Rodríguez-Matellán, A., Alcazar, N., Hernández, F., Serrano, M. & Ávila, J. In vivo reprogramming ameliorates aging features in dentate gyrus cells and improves memory in mice. *Stem Cell Rep* **15**, 1056–1066 (2020).
35. Xu, L. et al. Restoration of neuronal progenitors by partial reprogramming in the aged neurogenic niche. *Nat. Aging* **4**, 546–567 (2024).
36. Chow, L. S. et al. Exerkines in health, resilience and disease. *Nat. Rev. Endocrinol.* **18**, 273–289 (2022).
37. Morland, C. et al. Exercise induces cerebral VEGF and angiogenesis via the lactate receptor HCAR1. *Nat. Commun.* **8**, 15557 (2017).
38. Høgestøl, E. A. et al. Cross-sectional and longitudinal MRI brain scans reveal accelerated brain aging in multiple sclerosis. *Front. Neurol.* **10**, 450 (2019).
39. Cole, J. H. et al. Longitudinal assessment of multiple sclerosis with the brain-age paradigm. *Ann. Neurol.* **88**, 93–105 (2020).
40. Brier, M. R. et al. "Brain age" predicts disability accumulation in multiple sclerosis. *Ann. Clin. Transl. Neurol.* **10**, 990–1001 (2023).
41. Chen, X. et al. Microglia-mediated T cell infiltration drives neurodegeneration in tauopathy. *Nature* **615**, 668–677 (2023).
42. Paliard, X. et al. Simultaneous production of IL-2, IL-4, and IFN-gamma by activated human CD4$^+$ and CD8$^+$ T cell clones. *J. Immunol.* **141**, 849–855 (1988).
43. Kasahara, T., Hooks, J. J., Dougherty, S. F. & Oppenheim, J. J. Interleukin 2-mediated immune interferon (IFN-gamma) production by human T cells and T cell subsets. *J. Immunol.* **130**, 1784–1789 (1983).
44. Matsushita, H. et al. Cytotoxic T lymphocytes block tumor growth both by lytic activity and IFNγ-dependent cell-cycle arrest. *Cancer Immunol. Res.* **3**, 26–36 (2015).
45. Said, E. A. et al. Programmed death-1–induced interleukin-10 production by monocytes impairs CD4$^+$ T cell activation during HIV infection. *Nat. Med.* **16**, 452–459 (2010).
46. Wolk, K., Döcke, W.-D., von Baehr, V., Volk, H.-D. & Sabat, R. Impaired antigen presentation by human monocytes during endotoxin tolerance. *Blood* **96**, 218–223 (2000).
47. Bryn, T. et al. LPS-activated monocytes suppress T-cell immune responses and induce FOXP3$^+$ T cells through a COX-2–PGE2-dependent mechanism. *Int. Immunol.* **20**, 235–245 (2008).
48. Rasa, S. M. M. et al. Inflammaging is driven by upregulation of innate immune receptors and systemic interferon signaling and is ameliorated by dietary restriction. *Cell Rep.* **39**, 111017 (2022).
49. Zhang, Y. et al. Hypothalamic stem cells control ageing speed partly through exosomal miRNAs. *Nature* **548**, 52–57 (2017).
50. Wang, W. et al. The crosstalk: exosomes and lipid metabolism. *Cell Commun. Signal.* **18**, 119 (2020).
51. Yang, F. et al. Human umbilical cord mesenchymal stem cell-derived exosomes ameliorate liver steatosis by promoting fatty acid oxidation and reducing fatty acid synthesis. *JHEP Rep.* **5**, 100746 (2023).
52. Ishikawa, T., Mizunoya, W., Shibakusa, T., Inoue, K. & Fushiki, T. Transforming growth factor-β in the brain regulates fat metabolism during endurance exercise. *Am. J. Physiol.* **291**, E1151–E1159 (2006).
53. Fujikawa, T., Matsumura, S., Yamada, H., Inoue, K. & Fushiki, T. Transforming growth factor-beta in the brain enhances fat oxidation via noradrenergic neurons in the ventromedial and paraventricular hypothalamic nucleus. *Brain Res.* **1173**, 92–101 (2007).
54. Matsumoto, J. et al. Brain-derived neurotrophic factor improves impaired fatty acid oxidation via the activation of adenosine monophosphate-activated protein kinase-α–proliferator-activated receptor-r coactivator-1α signaling in skeletal muscle of mice with heart failure. *Circ. Heart. Fail.* **14**, e005890 (2021).
55. Sharma, P. et al. Exosomes regulate neurogenesis and circuit assembly. *Proc. Natl Acad. Sci. USA* **116**, 16086–16094 (2019).
56. Kirby, E. D., Kuwahara, A. A., Messer, R. L. & Wyss-Coray, T. Adult hippocampal neural stem and progenitor cells regulate the neurogenic niche by secreting VEGF. *Proc. Natl Acad. Sci. USA* **112**, 4128–4133 (2015).
57. Miller, L. N. et al. Neural stem and progenitor cells support and protect adult hippocampal function via vascular endothelial growth factor secretion. *Mol. Psychiatry* https://doi.org/10.1038/s41380-024-02827-8 (2024).

58. Dause, T. J. et al. Autocrine VEGF drives neural stem cell proximity to the adult hippocampus vascular niche. *Life Sci. Alliance* **7**, e202402659 (2024).
59. Grunewald, M. et al. Counteracting age-related VEGF signaling insufficiency promotes healthy aging and extends life span. *Science* **373**, eabc8479 (2021).
60. Yuan, P. et al. Neural stem cell-derived exosomes regulate neural stem cell differentiation through miR-9–Hes1 axis. *Front. Cell Dev. Biol.* **9**, 601600 (2021).
61. Verdin, E. NAD^+ in aging, metabolism, and neurodegeneration. *Science* **350**, 1208–1213 (2015).
62. Mutlu, A. S., Duffy, J. & Wang, M. C. Lipid metabolism and lipid signals in aging and longevity. *Dev. Cell* **56**, 1394–1407 (2021).
63. Yaku, K., Okabe, K. & Nakagawa, T. NAD metabolism: implications in aging and longevity. *Ageing Res. Rev.* **47**, 1–17 (2018).
64. Kjell, J. et al. Defining the adult neural stem cell niche proteome identifies key regulators of adult neurogenesis. *Cell Stem Cell* **26**, 277–293.e8 (2020).
65. Morton, M. C., Neckles, V. N., Seluzicki, C. M., Holmberg, J. C. & Feliciano, D. M. Neonatal subventricular zone neural stem cells release extracellular vesicles that act as a microglial morphogen. *Cell Rep.* **23**, 78–89 (2018).
66. Schlaepfer, I. R. & Joshi, M. CPT1A-mediated fat oxidation, mechanisms, and therapeutic potential. *Endocrinology* **161**, bqz046 (2020).
67. Knobloch, M. et al. A fatty acid oxidation-dependent metabolic shift regulates adult neural stem cell activity. *Cell Rep.* **20**, 2144–2155 (2017).
68. Mihaylova, M. M. et al. Fasting activates fatty acid oxidation to enhance intestinal stem cell function during homeostasis and aging. *Cell Stem Cell* **22**, 769–778.e4 (2018).
69. Kaya, T. et al. $CD8^+$ T cells induce interferon-responsive oligodendrocytes and microglia in white matter aging. *Nat. Neurosci.* **25**, 1446–1457 (2022).
70. Gate, D. et al. Clonally expanded CD8 T cells patrol the cerebrospinal fluid in Alzheimer's disease. *Nature* **577**, 399–404 (2020).
71. Groh, J. et al. Accumulation of cytotoxic T cells in the aged CNS leads to axon degeneration and contributes to cognitive and motor decline. *Nat. Aging* **1**, 357–367 (2021).
72. Kedia, S. et al. T cell-mediated microglial activation triggers myelin pathology in a mouse model of amyloidosis. *Nat. Neurosci.* **27**, 1468–1474 (2024).
73. Da Mesquita, S. et al. Aging-associated deficit in CCR7 is linked to worsened glymphatic function, cognition, neuroinflammation, and β-amyloid pathology. *Sci. Adv.* **7**, eabe4601 (2021).
74. Saligrama, N. et al. Opposing T cell responses in experimental autoimmune encephalomyelitis. *Nature* **572**, 481–487 (2019).
75. Rustenhoven, J. et al. Age-related alterations in meningeal immunity drive impaired CNS lymphatic drainage. *J. Exp. Med.* **220**, e20221929 (2023).
76. Ziv, Y. et al. Immune cells contribute to the maintenance of neurogenesis and spatial learning abilities in adulthood. *Nat. Neurosci.* **9**, 268–275 (2006).
77. Kipnis, J., Gadani, S. & Derecki, N. C. Pro-cognitive properties of T cells. *Nat. Rev. Immunol.* **12**, 663–669 (2012).
78. Filiano, A. J. et al. Unexpected role of interferon-γ in regulating neuronal connectivity and social behaviour. *Nature* **535**, 425–429 (2016).
79. Yshii, L. et al. Astrocyte-targeted gene delivery of interleukin 2 specifically increases brain-resident regulatory T cell numbers and protects against pathological neuroinflammation. *Nat. Immunol.* **23**, 878–891 (2022).

Methods

Animals

All procedures involving mice were performed according to protocols approved by the Stanford University IACUC and APLAC (protocol no. 8661) and VA Palo Alto Committee on Animal Research ACORP (LUO1736). For the ageing cohort and exercise cohort, male C57BL/6JN mice were obtained from the National Institute on Aging (NIA) Aged Rodent colony. For the whole-body partial reprogramming cohort, male whole-body inducible OSKM (iOSKM) mice (*ROSA26(rtTA-M2); Col1a1(tetO-OSKM)*) (on a mixed background of the following strains: C57BL/6, B6D2F1, 129S4 and B6129SF1/J) were generated from the Jaenisch laboratory[80] and obtained from the Jackson Laboratory (JAX 011004). Mice were housed in groups of 3–5 mice of the same age at the ChEM-H/Neuro vivarium (ageing and partial reprogramming) or at the Veterinary Medical Unit at the Veterans Affairs Palo Alto Health Care System (exercise) under 12-h light/dark cycles, approximately 21 °C ambient temperature, and approximately 50% humidity for at least 3 weeks before any experiments or sample collection occurred.

Ageing coronal and sagittal cohorts

We used two independent ageing cohorts of male C57BL/6JN mice (referred to as ageing cohort 1 and ageing cohort 2). Ageing cohort 1 included mice of the following ages for the coronal section dataset: 3.8, 5.4, 9.8, 12.9, 15.5, 21.4, 23.5, 26.7, 30.9 and 33.2 months. Ageing cohort 1 also included mice of the following ages for the sagittal section dataset: 3.8 and 26.7 months. Ageing cohort 2 included mice of the following ages for the coronal section dataset: 3.4, 4.3, 6.6, 15.8, 18.8, 19.8, 24.6, 28.5, 32.6 and 34.5 months. Ageing cohort 2 included mice of the following ages for the sagittal section dataset: 6.6, 8.6, 19.8 and 23.5 months. Information on all mice in the ageing cohorts is provided in Supplementary Table 4.

Exercise experiment

The exercise experiment included 3 groups of male C57BL/6JN mice: 4 young (3 months) sedentary mice, 4 old (19 months) sedentary mice, and 4 old (19 months) exercise mice. Information on all mice in the exercise experiment is provided in Supplementary Table 4. Sample sizes were selected to allow testing of statistically significant differences of mouse-level attributes (for example, cell-type proportion) using the non-parametric two-sided Mann–Whitney *U*-test across groups. Littermates were randomized for exercise and sedentary conditions. The mice in the old exercise group were provided with voluntary wheel running through individual housing for 5 weeks in polycarbonate cages with 12.7 cm diameter running wheels (Lafayette Instrument, 80820) and monitored weekly for adequate running. The five-week duration of voluntary exercise was selected based on published regimens for efficacy[32,81]. Sedentary mice were individually housed in identical ages without running wheels.

Whole-body partial reprogramming experiment

The whole-body partial reprogramming experiment included 3 groups of male iOSKM mice (on a mixed background of the following strains: C57BL/6, B6D2F1, 129S4 and B6129SF1/J): 4 young (4.8–4.9 months) control mice, 4 old (25.6–29.2 months) control mice, and 4 old (26.5–29.2 months) OSKM mice. Information on all mice in the partial reprogramming experiment is provided in Supplementary Table 4. Sample sizes were selected to allow testing of statistically significant differences of mouse-level attributes (for example, cell-type proportion) using the non-parametric two-sided Mann–Whitney *U*-test across groups. Old mice were matched by age and body weight and then randomized to control and OSKM conditions. All mice (control and OSKM) were individually housed during the experiment. The mice in the old OSKM group underwent three periods of cyclic induction of OSKM by doxycycline treatment, which consisted of doxycycline administration in the drinking water for two days (ON), followed by five days without doxycycline administration (OFF) and repeated for 3 weeks (ON–OFF–ON–OFF–ON) with mice euthanized at the end of the last doxycycline administration treatment. Doxycycline (Fisher ICN19895505) was dissolved in drinking water (1 mg ml^{-1}), placed in amber water bottles to protect the solution from light, and provided ad libitum to the mice in the old OSKM group.

Sample collection

Mice were euthanized to collect fresh frozen whole-brain samples for MERFISH experiments. Mice were euthanized with 5 min of exposure in a CO$_2$ chamber, and brains were removed and placed in a cryomold on ice and filled with pre-chilled Optimal Cutting Temperature (OCT) Compound (Fisher Healthcare Tissue Plus, 4585) and then placed on dry ice. After OCT solidified, the samples were moved to long-term storage at −80 °C. RNaseZap (Invitrogen, AM9780) was used to disinfect all dissection tools before and after each mouse. The sample collection for ageing cohort 1 occurred on 4 November 2022 from 14:00–15:30 pm Pacific Standard Time (PST) and the sample collection for ageing cohort 2 occurred on 28 June 2023 from 14:30–16:15 PST. Sample collection alternated between younger and older mice. For the exercise experiment, mice were perfused with 15 ml of PBS with heparin sodium salt (50 U ml^{-1}) (Sigma-Aldrich, H3149-50KU) before sample collection. Sample collection for the exercise experiment occurred on 6 June 2022, and sample collection for the partial reprogramming experiment occurred on 28 June 2023. Sample collection alternated between mice from different experimental conditions.

MERFISH 300-gene panel selection

We selected 300 genes to profile for the MERFISH experiments. Our selected 300-gene panel consists of 129 cell-type and subtype markers (81 cell-type markers, ranging from 1 to 8 markers per cell type; 48 subtype or function-related markers) as well as 181 genes of interest that have been implicated in ageing-related pathways, in important processes not previously linked to ageing, as well as genes identified by analysis of single-cell RNA-seq atlases of murine brain ageing, with 10 genes shared across cell-type and subtype markers and genes of interest (Supplementary Table 1).

The cell-type and subtype marker genes included all markers in a suggested panel by Vizgen; markers determined from literature review focused on cells of the brain vasculature[5,82,83], NSCs and neuroblasts[3,5,84,85], and immune cells[3,5,86,87]. For these 129 cell-type or subtype markers, we also included several NSC and neuroblast markers obtained from integrated differential gene expression analysis across multiple single-cell RNA-seq datasets of the adult mouse subventricular zone[3,4]. We included markers for the following cell types: excitatory neurons, inhibitory neurons, medium spiny neurons, astrocytes, microglia, oligodendrocytes, OPCs, endothelial cells, pericytes, VSMCs, VLMCs, ependymal cells, neuroblasts, NSCs, macrophages, neutrophils, T cells, B cells, natural killer (NK) cells, mast cells and dendritic cells.

For the ageing-related genes, we included a set of 33 genes related to murine ageing selected from the GenAge model organism database[28] (accessed 7 September 2022) (Supplementary Table 1) to enrich for genes known to have a causal role in ageing, which is helpful for building more causal ageing clocks[88,89]. We further included genes related to T cell activity[3], subventricular zone NSC heterogeneity[90], endothelial heterogeneity[91], meningeal lymphatics functions[83,92,93], cellular senescence, immune response, stem cells, neurogenesis[94] and vasculogenesis[95]. We also included sets of expert-curated genes pertaining to interesting cellular and organismal functions, some of which have emerging roles in the regulation of ageing but are not well studied yet, including T cell signalling, reprogramming, cell adhesion and migration, lipid metabolism and neuropeptide signalling. Finally, for a more unbiased set of genes, we included several differentially expressed genes (DEGs) between young and old mice for cell types across three single-cell transcriptomics datasets of the subventricular zone[3,4] and two multi-region brain single-cell transcriptomics datasets[5,7].

We ensured that all selected genes in the MERFISH panel were expressed in existing single-cell or single-nuclei RNA-seq brain atlases[4,5,7] and met technical constraints for minimizing optical clouding. This included limiting the total estimated gene expression using the Vizgen Gene Panel Design Portal to under 9,000 fragments per kilobase of transcript per million mapped reads (FPKM) (total estimate at 7,691 FPKM) and limiting the maximum estimated expression per gene using the Vizgen Gene Panel Design Portal to under 700 FPKM (maximum per-gene estimate at 452 FPKM). The complete gene panel, classification of markers, and rationale for inclusion are included in Supplementary Table 1.

MERFISH imaging experiment

The MERFISH experiment was conducted through the Vizgen MERSCOPE technology laboratory service. Compared with other spatially resolved single-cell transcriptomics, Vizgen MERSCOPE technology has been shown to provide high specificity and sensitivity even with larger gene panel sizes[96]. Fresh frozen mouse brain samples were cut into 10 μm-thick sections on a cryostat at −20 °C and placed onto a MERSCOPE slide (Vizgen 20400001). We obtain coronal sections that contain the CTX, STR, CC/ACO and VEN including the subventricular zone neurogenic niche. We obtain sagittal sections that contain the aforementioned brain regions along with additional brain regions (olfactory bulb, rostral migratory stream, brain stem, and cerebellum). Two coronal sections were placed on each slide and paired to balance ages while sagittal sections were placed on their own slides. The tissue sections were fixed with 4% paraformaldehyde in 1× PBS for 15 min, washed 3 times with 5 ml 1× PBS and incubated with 70% ethanol at 4 °C overnight for tissue permeabilization. Samples were then stained for cell boundary using Cell Boundary Kit (Vizgen, 10400009), and later hybridized with a custom designed MERSCOPE Gene Panel Mix consisting of 300 genes (Vizgen 20300008) in a 37 °C incubator for 36–48 h. Following incubation, the tissues were washed with 5 ml formamide wash buffer at 47 °C for 30 min, twice and embedded into a hydrogel using the Gel Embedding Premix (Vizgen 20300004), ammonium persulfate (Sigma, 09913-100 G) and TEMED (*N*,*N*,*N*′,*N*′-tetramethylethylenediamine) (Sigma, T7024-25ML) from the MERSCOPE Sample Prep Kit (10400012). After the gel mix solution solidified, the samples were cleared with clearing solution consisting of 50 μl Proteinase K (NEB, P8107S) and 5 ml of Clearing Premix (Vizgen 20300003) at 37 °C overnight. After removing clearing solution, the sample was stained with DAPI and Poly T Reagent (Vizgen 20300021) for 15 min at room temperature, washed for 10 min with 5 ml of Formamide Wash Buffer, and then imaged on the MERSCOPE system (Vizgen 10000001). A fully detailed, step-by-step instruction on the MERFISH sample prep the full protocol is available at https://vizgen.com/resources/fresh-and-fixed-frozen-tissue-sample-preparation/. Full instrumentation protocol is available at https://vizgen.com/resources/merscope-instrument/. The MERFISH data were collected over two separate batches (see ‘slide_id’ in Supplementary Table 4). The first batch, A, included ageing cohort 1 (both coronal and sagittal) and half of the exercise experiment samples with even representation across conditions. The second batch, B, included ageing cohort 2 (both coronal and sagittal), the remaining half of the exercise experiment samples, and the partial reprogramming experiment samples.

Cell segmentation and MERFISH data preprocessing

Segmentation of cells was performed using Cellpose (1.0.2) through Vizgen's laboratory service. Cell segmentation was implemented on images using nuclear staining (DAPI) and cytosolic staining (Poly T). Transcripts were allocated using these cell segmentations by summing across seven *z*-stacks, accounting for both nuclear and cytosolic (soma) transcripts. Quality control statistics were computed using the Vizgen post-processing tool (vpt) (1.2.2) for cell segmentation (Supplementary Table 2).

For preprocessing, we performed initial cell filtering separately for each MERFISH experiment (consisting of either two coronal sections on the same slide or one sagittal section). For each experiment, we removed putative doublets using Scrublet[97] and a doublet score cutoff of 0.18. We then filtered out all cells with segmentation volume less than or equal to 100 μm^3 or greater than or equal to 3 times the median cell volume. We also filtered out all cells with fewer than or equal to 20 counts and/or fewer than or equal to 5 genes with non-zero expression. To correct for potential different segmentation sizes, we divided the raw transcript counts obtained for each cell in the MERFISH dataset by the volume of the corresponding segmentation. After combining all experiments into an integrated dataset, we then filtered out all cells in the top 2% highest and top 2% lowest total expression. Statistics associated for the aforementioned cell filtering steps and for additional steps after clustering can be found in Supplementary Table 3. To obtain log-normalized gene expression values, we normalized the total gene expression for each cell to 250 and log-transformed the expression with an added pseudocount. This procedure was performed separately for the ageing cohorts (coronal), ageing cohorts (sagittal), exercise experiment and partial reprogramming experiment.

Cell-type clustering and identification

For clustering, we converted each log-normalized gene expression value to a *z*-score using scanpy.pp.scale with max_value = 10 in the scanpy package[98]. We performed Leiden clustering using scanpy.tl.leiden with resolution = 0.5 for the initial clustering and default settings otherwise. We obtained batch-balanced nearest neighbours graph using BBKNN (scanpy.external.pp.bbknn) and then used this neighbours graph to generate a UMAP visualization of all cells (scanpy.tl.umap). For the partial reprogramming experiment, which only involved one batch of MERFISH data, we used scanpy.pp.neighbors with n_pcs=20 and n_neighbors=15 instead of BBKNN. To annotate cell types, we manually labelled each cluster based on cell-type expression patterns as observed across two orthogonal data visualization modalities (the UMAP visualization and a heat map of cell-type markers) to reduce errors in cell-type annotation resulting from dimensionality reduction distortions[99,100]. For clusters that expressed markers from multiple cell types, we performed successive Leiden clustering on those clusters until unique cell types could be annotated (see Supplementary Table 5). This procedure was performed separately for the ageing cohorts (coronal), ageing cohorts (sagittal), exercise experiment, and partial reprogramming experiment. A detailed description of the cell-type markers and Leiden clustering resolutions for each dataset and cell type can be found in Supplementary Table 5. Although a small set of markers for some rare immune cell types (NK cells, mast cells, dendritic cells) were included in our MERFISH panel (Supplementary Table 1), we were unable to identify these cell types in any of the datasets (Supplementary Table 5), probably owing to their low abundance. NK cells, mast cells, and dendritic cells were also not identified in several existing spatial transcriptomics studies of adult mouse brain[17,21–24]. NK cells and dendritic cells were identified in a large-scale and high-resolution spatial transcriptomic profiling of the whole adult mouse brain[25], although at 3–4 times lower abundance than the rarest immune cell types identified in our datasets (T cells and B cells), which may explain why we were not able to identify these cells in our dataset. In addition, in the partial reprogramming dataset, we were unable to identify other rare immune cell types (T cells, B cells and neutrophils), consistent with our previously published dissociated single-cell RNA-seq datasets[35] and probably owing to the lower abundance of these cell types in this partial reprogramming mouse model.

Spatial region and subregion clustering and annotation

To identify anatomical regions across the MERFISH datasets and assign region and subregion labels to each cell, we adapted a semi-supervised approach for clustering and annotating region labels from cell-type composition of local neighbourhoods around each cell[17]. For a given cell, we computed the cell-type abundances for each cell within 100 µm distance from the given cell. Then, we performed principal component analysis on the matrix consisting of the cell-type abundance profiles for each cell, applied *k*-means clustering ($k = 25$), manually visualized and merged clusters to obtain seven subregion annotations (CC/ACO, CTX_L1/MEN, CTX_L2/3, CTX_L4/5/6, STR_CP/ACB, STR_LS/NDB and VEN), and finally merged subregion annotations to obtain four region annotations (CC/ACO, CTX, STR and VEN). While we observed some variability in the subregion annotations between samples, there was general consistency in the four region annotations. We verified the expression of cortical layer markers in the three subregions of the CTX (Extended Data Fig. 3c,d), but we were unable to annotate each of the six known cortical layer individually through the clustering procedure, perhaps owing to the low number of cortical layer markers. This region and subregion clustering and annotation procedure was performed separately for the ageing cohorts (coronal), ageing cohorts (sagittal), exercise experiment, and partial reprogramming experiment.

Cell-type composition analysis

We computed cell-type proportions for a given sample by dividing the number of cells of each cell type by the total number of cells in the sample. For regional cell-type proportions, we divided the number of cells of each cell type in that region by the total number of cells in that region. Pearson correlation, 95% confidence interval for the correlation, and *P* value for association between cell-type proportion and sample age was computed using scipy.stats.pearsonr. We annotated strong changes in cell-type proportion with age as cell types with 95% confidence interval for the correlation that does not overlap with the interval [−0.25, 0.25]. Strong increases in cell-type proportion with age (coloured red) had 95% confidence interval for the correlation with lower bound greater than 0.25, and strong decreases in cell-type proportion with age (coloured blue) had 95% confidence interval for the correlation with upper bound less than −0.25. Linear regression of cell-type proportion on sample age with 95% confidence interval was computed using seaborn.regplot. To compute statistical significance of differences in cell-type proportions across categorical conditions, we used the two-sided Mann–Whitney *U*-test.

Increasing and decreasing gene expression with age analysis

For a given cell type, to identify genes that changed in expression with age, we computed the Spearman correlation between age and pseudobulk gene expression across samples in the coronal section dataset. The pseudobulk gene expression was computed as the mean log-normalized gene expression across all cells of the same cell type within a sample. For each gene, we obtained the Spearman correlation, the associated *P* value, and the lower and upper bounds of a 95% confidence interval for the correlation. We classified genes as 'increasing' if they had Spearman correlation greater than 0.3 and with the lower bound of the 95% confidence interval greater than 0.0. We classified genes as 'decreasing', if they had Spearman correlation less than −0.3 and with the upper bound of the 95% confidence interval less than 0.0. To reduce false positives resulting from transcript spillover due to segmentation, we constrained our analysis to the 220 genes with less than 5% estimated spillover based on an internal Vizgen metric using gene expression variations influenced by local cellular composition (see Supplementary Table 7 for list of genes).

GO enrichment analysis

We performed GO enrichment analysis to determine biological processes that were enriched in different sets of genes. For genes that increase or decrease in expression with age that were identified in 'Increasing and decreasing gene expression with age analysis', we performed GO biological process enrichment analysis separately for each set of genes and for each cell type. For genes in different spatiotemporal gene expression trajectory clusters for oligodendrocytes in the CC/ACO region (see 'Spatiotemporal gene expression trajectory analysis'), we performed GO biological process enrichment analysis for all genes present in each of the nine trajectory clusters separately after filtering out genes with greater than 5% estimated spillover based on an internal Vizgen metric using gene expression variations influenced by local cellular composition. For GO enrichment analysis on genes used by the spatial ageing clocks, we selected positive coefficient clock genes (up to 50 genes with the largest positive coefficients) and negative coefficient clocks genes (up to 50 genes with the largest negative coefficients) and performed GO biological process enrichment analysis separately for each set of genes. For GO enrichment analysis on DEGs in endothelial cells in response to exercise in old mice, we selected genes that significantly increased with exercise (increased in old exercise compared with old sedentary with $P < 0.05$ from two-sided Mann–Whitney *U*-test) and genes that significantly decreased with exercise (decreased in old exercise compared with old sedentary with $P < 0.05$ from two-sided Mann–Whitney *U*-test) and performed GO biological process enrichment analysis separately for each set of genes.

We performed GO biological process enrichment analysis by selecting genes for each analysis (as described above), and using all other genes measured by MERFISH as background. GO enrichment was performed with topGO[101] (R package version 2.54.0) using Fisher's exact test for all Biological Process terms.

Regional gene expression changes with age

To compare different anatomic regions and subregions by the magnitude of gene expression changes with age, we selected the five youngest and five oldest mice in the data. For each cell type, we determined the minimum number of cells present across each of the mice and regions, excluding the VEN due to their low cell number. We then downsampled cells for each mouse and region, without replacement, to that minimum number, such that after sampling, all combinations of mouse and region had the same number of cells. We then excluded cell types in which the number of cells per mouse and region was less than 20. We calculated the transcriptional profile for each mouse and region by averaging across the volume-normalized expression of all cells from that mouse in that region, normalizing this profile to sum to 250, and performing a log transformation with an added pseudocount. To determine the change between old and young mice in a specific region, we subtracted the mean profile of the 5 young mice from the mean profile of the 5 old mice and averaged the absolute value of this difference across all genes after filtering out genes with greater than 5% estimated spillover based on an internal Vizgen metric using gene expression variations influenced by local cellular composition. We repeated this process 20 times, each time sampling different cells.

Spatiotemporal gene expression trajectory analysis

For each cell, we divided the raw transcript counts by the segmentation volume of the cell and then normalized by total count using the default settings of scanpy.pp.normalize_total. For each combination of cell type, anatomic subregion, and gene; we computed a vector of length 20 (trajectory) containing the mean expression of that gene in each age conditioned on a specified subregion and cell type. If the given cell type and subregion combination was not present in at least 70% of profiled ages, we classified that trajectory as 'missing'. We performed last-value-carried-forward imputation to fill in missing values within trajectories that passed this threshold. Each trajectory was standardized by centring and scaling to unit variance with sklearn.preprocessing.StandardScaler[102]. Then, we performed *k*-means clustering using sklearn.cluster.KMeans with n_clusters=9, random_state=444, n_init='auto', and the matrix with each row corresponding to a scaled gene expression trajectory as input. The parameters of the clustering were selected to maximize the number of clusters while also maintaining qualitatively distinct trends in each cluster (Extended Data Fig. 4a,b). For each cluster of gene expression trajectories, we visualized the smoothed median and interquartile range of the scaled expression values. Smoothing was done with interpolating B-splines using scipy.interpolate.BSpline with $s = 20$. We manually annotated each cluster based on the qualitative expression patterns. These trajectory clusters include genes with expression that increases late in life ('increasing late'), increases gradually throughout life ('increasing gradual'), has the lowest expression in midlife ('midlife trough'), peaks in early life ('early peak'), peaks in midlife ('midlife peak'), peaks in late life ('late peak'), decreases after midlife ('midlife decrease'), decreases early in life ('decreasing early'), and decreases gradually through life ('decreasing gradual'). To visualize representative gene expression trajectories for each cell type, we performed the same smoothing procedure separately for each cell-type-specific subset of trajectories from the clusters. We developed this trajectory clustering approach instead of using parametric methods (for example, polynomial fitting) to provide a more unbiased characterization of different trajectories.

SpatialSmooth soft pseudobulking procedure

For each cell type, we build spatial graphs connecting each cell with its 20 nearest neighbours by Euclidean distance and of the same cell type[103]. Spatial ageing clock performance was generally robust to the choice of the number of nearest neighbours (k) in building this graph (Extended Data Fig. 5a). We computed a L1-normalized adjacency matrix representing the spatial graph. Then, the SpatialSmooth algorithm propagates gene expression features across the cell-type-specific spatial graph by iterating the update equation until convergence (that is, $X_{t+1} \approx X_t$):

$$X_{t+1} \leftarrow (1-\alpha)X + \alpha S X_t$$

Where X is the initial gene expression matrix (cells as rows, genes as columns), S is the normalized adjacency matrix, and α is the smoothing parameter. We set α equal to 0.8. We set the convergence to be 30 iterations at maximum with a tolerance of 0.01, for which convergence is reached if $||X_{t+1} - X_t||_\infty$ is less than the tolerance or 30 iterations has elapsed. For rare cell types (for example, T cells, B cells, neutrophils), SpatialSmooth generally converged before 30 iterations. For common cell types (for example, oligodendrocytes, microglia, astrocytes), SpatialSmooth was generally performed for 30 iterations. After convergence at step $t = T$, we use the smoothed spatial gene expression matrix X_T as input for training the ageing clocks.

Training and cross-validated evaluation of spatial ageing clocks

For training spatial ageing clocks, we performed the SpatialSmooth procedure on the log-normalized gene expression to obtain smoothed spatial gene expression matrices for each cell type independently. Then, for each cell type, we fitted a pipeline consisting of standardization of gene features followed by lasso regression model to predict sample age from a cell's gene expression profile and used sklearn.linear_model.LassoCV to select optimal hyperparameters with cv=5, n_alphas=20, max_iter=10000. We refer to this entire pipeline from SpatialSmooth to age prediction as the 'spatial ageing clock'. To avoid explicit conditioning of age prediction on spatial information, the spatial ageing clocks only leverage the spatial context to process the input data via SpatialSmooth.

For cross-validated evaluation of spatial ageing clocks, we held out a single sample/age as the test set and kept the remaining samples/ages as the train set. SpatialSmooth was performed separately for the train and test sets. We fitted the lasso regression pipeline to predict age on the train set and used the model to obtain predicted ages on the test set. We repeated this procedure across all samples/ages to obtain predicted ages for all cells in the study. Performance was evaluated by Pearson's correlation (R) and mean absolute error between the age and predicted ages of individual cells obtained from cross-validation. We also computed the Pearson's correlation (r) between the age and median predicted ages of individual mice obtained from cross-validation. For the subregion-specific ageing clocks, we trained and evaluated the models using the same settings except with five nearest neighbours for SpatialSmooth and restricted to only cells in each subregion for training. To compare spatial ageing clocks to cell-type-specific ageing clocks trained on dissociated single-cell RNA-seq data from adult mouse subventricular zone, we used the median predicted ages associated with these clocks and data[4].

Visualization of spatial ageing clock predictions

We used two approaches for visualizing the predicted ages obtained from the application of spatial ageing clocks, either through cross-validation on the coronal section dataset or directly through validation on an external dataset.

For datasets with relatively uniform distribution of many ages across lifespan (that is, the coronal section dataset), we used a correlation plot visualization consisting of a two-dimensional histogram of cell frequencies across bins defined by predicted age and actual age that is visualized as a heat map, a scatter plot of the median predicted age of cells across each sample as a function of the actual age, and a line of best fit for the median predicted ages as a function of actual age is shown in black and computed using numpy.polyfit with deg = 1. This type of visualization emphasizes the quality of median predicted age at the sample level across many different actual age values. Generally, in this visualization, the range of predicted ages will be larger than the range of actual ages due to heterogeneity in the predicted ages but not in the actual ages of cells from the same mouse. This may be especially pronounced for highly abundant cell types like excitatory neurons. Predicted ages obtained from cross-validation using a leave-mouse-out approach will exhibit some regression to the mean age (that is, cells from older mice predicted to be younger and cells from younger mice to be predicted to be older) due to different mean actual ages in each of the cross-validation training datasets.

For datasets with bimodal distribution of ages (that is, the sagittal section dataset) or with three or fewer distinct age groups (that is, all external datasets), we used a density plot visualization of predicted ages of cells across different age groups or different experimental conditions. A kernel density estimate was constructed for each group of predicted ages using seaborn.kdeplot with default settings. This type of visualization emphasizes the distribution of predicted ages in a small number of groups at the cell level. For the coronal sections dataset and sagittal sections dataset, we used both types of representations.

For comparisons of clock performances, we compare the mean absolute error and Pearson correlation between predicted age and actual age either with respect to the main spatial ageing clocks or between different data subsets or clocks to make our conclusions.

Application of spatial ageing clocks on external datasets

To apply the spatial ageing clocks to predict age for cell gene expression profiles in external spatial transcriptomics datasets, we applied the following general procedure. First, we filtered the external dataset to only include genes present in our MERFISH panel of 300 genes and only cell types also represented among the spatial ageing clocks. Then, we normalized and log-transformed the raw expression values using the same approach as for our MERFISH data and applied SpatialSmooth ($\alpha = 0.8$) to the log-normalized values for each cell type independently. For clock genes that are not present in the external dataset, we use the training data for the clock as reference data in the SpaGE algorithm[104] (n_pv = 15) to impute the expression of the missing genes. Negative imputed values were clipped to zero. We performed imputation for genes from our MERFISH panel that were missing from these datasets (228 genes in the 140-gene MERFISH coronal section dataset, 5 genes in the single-nuclei RNA-seq dataset, 36 genes in the single-cell RNA-seq dataset, 225 genes in the LPS dataset, 128 genes in the Alzheimer's mouse model dataset, 240 genes in the global demyelination through the EAE dataset, 236 genes in the localized demyelination injury dataset). Finally, for each cell type, we applied the corresponding spatial ageing clock to generate predicted ages from the smoothed spatial gene expression values. For single-nuclei RNA-seq datasets, which lack spatial information, we used the pseudobulk approach from a previous model[4] with 20 cells contributing to each pseudocell instead of SpatialSmooth.

For all evaluations, we also quantified the magnitude of difference in median predicted age (in units of months) and the 95% confidence interval for this difference, which was computed from the empirical distribution of differences in median predicted ages using 1,000 bootstrap samples of individual mice within each condition. These statistics are reported in Supplementary Table 12. In some cases, imputation resulted in biased age predictions, but the differences in predicted age across ages and conditions were generally robust. In applying spatial ageing clocks with imputation, we recommend comparing the predicted age to known ages in the dataset to calibrate interpretations. Generally, we observed lower spatial ageing clock performance for cell types with low transcriptomic changes with age such as neurons (see Fig. 1e) or those with limited marker genes in external datasets such as neuroblasts (see Fig. 2d). Results were also generally consistent for all applications of the spatial ageing clocks without SpaGE imputation and when using spatial ageing clocks trained with the 220 genes (see Supplementary Table 7 for list) with less than 5% estimated spillover based on an internal Vizgen metric using gene expression variations influenced by local cellular composition (Supplementary Table 12).

Age acceleration calculation

We computed age acceleration for the predicted age of each cell to measure the deviation from its expected predicted age (that is, the average of predicted age across all cells from a given cell type and mouse). For each sample $k \in \{1, \ldots, K\}$ and cell type $p \in \{1, \ldots, P\}$, we define the set of cells belonging to both sample k and cell type p as Q, and the age acceleration for each cell $i \in Q$ is defined as:

$$(\text{Age acceleration})_i = (\text{Predicted age})_i - E\,\{(\text{Predicted age})_j \mid j \in Q\}$$

Single-nuclei RNA-seq ageing data processing

We applied our spatial ageing clocks to publicly available single-nuclei RNA-seq data on the CTX and STR of juvenile (0.93 months) and old (20.93 months) female C57BL/6 J mice[17]. We downloaded processed data objects containing the scaled log-normalized gene expression from https://cellxgene.cziscience.com/collections/31937775-0602-4e52-a799-b6acdd2bac2e and mapped several cell types to our cell-type classifications. We modified the preprocessing and imputation steps outlined in 'Application of spatial ageing clocks on external datasets' to account for the scaled log-normalized expression being used as input. Predicted ages were highly consistent when using a scaled log-normalized coronal section dataset for imputation.

Single-cell RNA-seq ageing data processing

We applied our spatial ageing clocks to publicly available single-cell RNA-seq data on whole-brain tissue (without hindbrain regions) of young (2–3 months) and old (21–22 months) male C57BL/6 J mice[5]. We downloaded processed datasets from https://portals.broadinstitute.org/single_cell/study/aging-mouse-brain and mapped several cell types to our cell-type classifications.

140-gene MERFISH ageing data processing

We applied our spatial ageing clocks to our previously published 140-gene MERFISH spatial transcriptomics data on whole-brain coronal sections of young (0.93 months), middle-aged (5.58 months) and old (20.93 months) male C57BL/6 JN mice[29]. We mapped several cell types to our cell-type classifications.

MERFISH ageing and LPS data processing

We applied our spatial ageing clocks to publicly available MERFISH spatial transcriptomics data on the CTX and STR of female C57BL/6 J mice in juvenile (0.93 months), young (5.58 months), old (20.93 months), and lipopolysaccharide (LPS)-injected conditions[17]. We downloaded processed data objects containing the scaled log-normalized gene expression from https://cellxgene.cziscience.com/collections/31937775-0602-4e52-a799-b6acdd2bac2e and mapped several cell types to our cell-type classifications and used existing region annotations. We modified the preprocessing steps outlined in 'Application of spatial ageing clocks on external datasets' to account for the scaled log-normalized expression being used as input. Predicted ages were highly consistent when using a scaled log-normalized coronal section dataset for imputation. We included all control (ageing) and LPS-injected mice in our analyses.

STARmap Alzheimer's disease data processing

We applied our spatial ageing clocks to publicly available STARmap PLUS spatial transcriptomics data on the CTX and hippocampus of male TauPS2APP (Alzheimer's disease model) and non-transgenic control mice across two ages (8 and 13 months)[22]. We downloaded processed data from https://singlecell.broadinstitute.org/single_cell/study/SCP1375 and mapped several cell types to our cell-type classifications and used existing region annotations. We included all control and Alzheimer's disease mice in our analyses. The percentage of zero counts was higher in this dataset (94%) than in the coronal section dataset used for training the spatial ageing clocks (70%).

In situ sequencing global demyelination data processing

We applied our spatial ageing clocks to publicly available in situ sequencing spatial transcriptomics data on whole-brain coronal sections of male and female C57BL/6J mice (2.5 months) across global demyelination and control conditions[23]. Global demyelination models consisted of induction of EAE via injection of myelin oligodendrocyte glycoprotein. We downloaded processed data from https://zenodo.org/records/8037425 and selected only whole-brain coronal sections. We mapped several cell types to our cell-type classifications and used existing region annotations. The percentage of zero counts in this dataset (76%) was similar to that in the coronal section dataset used for training the spatial ageing clocks (70%).

MERFISH localized demyelination injury data processing

We applied our spatial ageing clocks to publicly available MERFISH spatial transcriptomics data of three whole-brain coronal sections at different depths collected from young (3–4 months) male C57BL/6J mice that were subjected to demyelination injury via stereotactic injection of lysophosphatidylcholine at coordinates (from bregma): (X, ±1.0 mm; Y, −0.1 mm)[21]. We downloaded processed data and metadata from Gene Expression Omnibus (GSE202638) and mapped several cell types to our cell-type classifications. Due to the spatially localized nature of the demyelination injury and the lack of control conditions in this dataset, we analysed the predicted ages of cells in this dataset by spatially visualizing all cells by their positive age acceleration (negative values floored at zero) across each of the coronal sections to determine spatial patterns in age acceleration with respect to the site of injury for all cell types and for different major cell types. The percentage of zero counts was higher in this dataset (94%) than in the coronal section dataset used for training the spatial ageing clocks (70%).

Effect of interventions on predicted age

For a given cell type and experiment, to quantify the difference in predicted ages between two experimental conditions, we computed the difference in median predicted ages between cells of the two conditions. Specifically for interventions, we subtracted the median predicted age of cells belonging to mice in the control condition (sedentary, control) from the median predicted age of cells belonging to mice in the intervention condition (exercise, OSKM, LPS or Alzheimer's disease). Positive values indicate that the intervention has an accelerated ageing effect and negative values indicate that the intervention has a rejuvenating effect on the cells of the mice. For the whole-body partial reprogramming experiment, since there was a difference in the mean age of mice in the control and OSKM conditions of 0.3 months, we corrected for this difference by adding an intercept to the predicted ages before computing the effect. We computed this effect at the global levels (all cells of a cell type) and at the regional level (all cells of a cell type within a defined anatomic region). For the adverse interventions datasets (LPS and Alzheimer's disease), we used the existing anatomic region annotations and mapped them to the closest region label in our study. For all global comparisons, we quantified the difference in median predicted age (in units of months) and the 95% confidence interval for this difference, which was computed from the empirical distribution of differences in median predicted ages using 1,000 bootstrap samples of individual mice within each condition. These statistics are reported in Supplementary Table 12.

Spatial visualizations of the effect of interventions on predicted age involved computing an effect value for each cell in a sample in the intervention condition. Specifically, for each cell in the intervention condition, we subtracted the median predicted age of cells belonging to mice in the age-matched control condition (sedentary, control) from the predicted age of that cell, and then visualized that cell by its spatial coordinates and coloured by the computed value.

Cell proximity effects of ageing and rejuvenation

The cell proximity effect measures the effect that an effector cell type has on the transcriptomic ageing of a target cell type by comparing target cells near effector cells to those that are far from effector cells. To compute the distribution of nearest neighbour distances, we constructed a triangulation mesh graph connecting neighbouring cells on a given sample using squidpy.gr.spatial_neighbors with delaunay=True[103]. We used the centroid of each cell to compute distances between cells. We computed subregion-specific distance cutoffs for calling nearby cells as the average of the median neighbour-neighbour distances measured across all samples. The distance cutoffs (in micrometres) for the ageing (coronal) study were: CC/ACO: 24.89, CTX_L1/MEN: 25.91, CTX_L2/3: 24.05, CTX_L4/5/6: 27.24, STR_CP/ACB: 21.65, STR_LS/NDB: 20.36, VEN: 17.86. The distance cutoffs (in micrometres) for the exercise study were: CC/ACO: 23.58, CTX_L1/MEN: 22.13, CTX_L2/3: 21.80, CTX_L4/5/6: 24.81, STR_CP/ACB: 20.75, STR_LS/NDB: 19.82, VEN: 16.23. Using these subregion-specific distance cutoffs, we identified target cells near effector cells ('near') and matched them to target cells far from any effector cells ('far') for a given target cell type and effector cell type. First, we computed for each cell, the shortest Euclidean distance to any effector cell in the same sample for each effector cell type. Then, for each sample and combination of target cell type and effector cell type, we labelled all target cells with shortest Euclidean distance to effector cell type that was less than the corresponding distance cutoff as 'near' and match them with 'far' target cells in the same subregion and sample that were furthest away from the effector cell type with shortest distance greater than the cutoff for 'near' cells. After obtaining matched sets of 'near' and 'far' target cells across all samples, we combined them into a single set to estimate the proximity effect of the effector cell type on the target cell type. The proximity effect was computed as Cohen's *d* measure of effect size between the age acceleration of the 'near' target cells compared with the age acceleration of the 'far' target cells. The variance in age acceleration was similar between 'near' and 'far' target cell groups (Extended Data Fig. 9a). We filtered out comparisons with less than 50 'near' cells or less than 50 'far' cells. Positive proximity effect values indicate a pro-ageing effect exerted by the effector cell type on the target cell type and negative proximity effect values indicate a pro-rejuvenating effect exerted by the effector cell type on the target cell type. We also computed the normalized frequency of proximity interactions as the number of 'near' target cells divided by the total number of target cells in the study and the statistics and *P* value from the associated two-sided Student's *t*-test between the age acceleration of the 'near' and 'far' target cells.

We implemented several variations to the standard proximity effect analysis. For region-specific proximity effects, we restricted the proximity effect analysis to only cells within each of the anatomic regions. For cell proximity effects using alternative definitions of 'far' cells, we used two orthogonal approaches. The first approach consisted of random sampling of 'far' cells from all target cells with shortest distance greater than the cutoff for 'near' cells in the same subregion and sample. The second approach consisted of selecting the set of 'far' cells with total raw transcript counts closest to the mean total raw transcript count of the 'near' cells in the same subregion and sample. For cell proximity effects based on predicted ages obtained from non-spatial ageing clocks such as spatial ageing clocks that did not use the SpatialSmooth step for prediction (SingleCell (SS)) or single-cell ageing clocks using cell-type-specific pseudobulking of gene expression (1,000 bootstrap samples of 30 cells following prescribed procedures[4]) during training and prediction (SingleCell (PB)), we used predicted ages from these aforementioned clocks in lieu of predicted ages from the spatial ageing clocks and performed cell proximity analysis following the original setup. For the 'spillover filtered' cell proximity effects, we used predicted ages from the spatial ageing clocks trained on the 220 genes with less than 5% estimated spillover based on an internal Vizgen metric using gene expression variations influenced by local cellular composition. For cell proximity effects on datasets other than the coronal section dataset, we computed dataset-specific distance cutoffs for subregions and regions and computed proximity effects using the original setup for all cell types that were mapped to our cell-type classifications. We calculated separate proximity effects for cells across the entire external dataset and for cells restricted to the control conditions. To assess the effect of interventions on cell proximity effects, we computed cell proximity effects separately for each experimental condition. We excluded the 140-gene MERFISH dataset from proximity effect analysis because this dataset was spatially sparse with distance cutoffs that were several times greater than that of other datasets, probably owing to lower cell detection/segmentation frequency.

The average proximity effect for each effector cell type was computed as the average proximity effect across all target cell types after filtering. To assess the most impacted target cell types, the mean absolute proximity effect for each target cell type was computed by averaging the absolute value of the proximity effect across all effector cell types after filtering.

Spatial permutation analysis

Spatial permutations can be used to assess frequency of cell–cell interactions occurring by chance due to regional differences in cell-type proportion[105]. We performed subregional spatial permutations of cells as a negative control for the spatial proximity effects measured for effector cells. In each permutation, for each sample in the ageing (coronal) study, we randomly permuted the spatial coordinates of each cell using numpy.random.permutation. This permutation was performed separately for each subregion to maintain regional heterogeneity. Then, we measured proximity effects on the permuted dataset. We repeated these permutations twenty times using random seeds drawn uniformly from 0 to 50,000 with a generating random seed of 444. We computed the median and 95% confidence interval for the proximity effect of each effector cell type across these twenty permutations.

Spatial visualization of age acceleration near effector cells

We generated visualizations of cells coloured by their age acceleration around key effector cell types (for example, T cells and NSCs) by selecting an effector cell, drawing a square bounding box centred on the effector cell with edge lengths of 200 μm, and then visualizing all cells with centre coordinates inside of the bounding box. We manually selected visualizations from a middle-aged (18.8 months) mouse for T cells and NSCs.

Impact of potential spillover transcripts on proximity effect

We verified that the cell proximity effects were unlikely to be confounded by spillover of transcripts between nearby effector and target cells arising from segmentation errors, which can be particularly prominent for cells near NSCs in the densely packed VEN region (Supplementary Fig. 7a). In a first approach to test this, we computed proximity effects based on predicted ages obtained from spatial ageing clocks trained on a subset of genes after filtering out genes with high estimated spillover rate (see Methods) (Supplementary Fig. 7b). In a second approach to test this, we performed area-restricted proximity effect analysis, which excluded cells within a small radius of the effector cells (see 'Area-restricted cell proximity effects'), for spatial ageing clocks and two non-spatial ageing clocks (Supplementary Fig. 8a,b). We verified that this area-restricted approach drastically attenuated transcript spillover effects in all target cell types near T cells and NSCs (Supplementary Fig. 8c). Both approaches corroborate that T cells have the most pro-ageing proximity effect and NSCs have the most pro-rejuvenating proximity effect (Supplementary Figs. 7b and 8b).

Area-restricted cell proximity effects

To remove the potential influence of transcript spillover from cell segmentations on the cell proximity effect analysis, we developed an alternative approach to compute area-restricted cell proximity effects, where 'near' cells are labelled using two cutoff distances instead of the single cutoff distance in the standard proximity effect analysis (see Supplementary Fig. 8a). We set the larger of the two cutoff distances equal to double the subregion-specific distance cutoff from 'Cell proximity effects of ageing and rejuvenation'. We set the smaller cutoff distance to be 15 μm less than the larger cutoff distance. We label target cells with shortest Euclidean distance to effector cell type that is greater than the smaller distance cutoff but less than the larger distance cutoff as 'near' and match them with 'far' target cells in the same region and sample that are farthest away from the effector cell type with shortest distance greater than the larger distance cutoff for 'near' cells. Then, area-restricted cell proximity effects are calculated using the same approach as described in 'Cell proximity effects of ageing and rejuvenation' except with these modified 'near' and 'far' cell labels.

Spatial gradation of cell proximity effects

We computed cell proximity effects as a function of the unit distance between the effector and target cells, where the unit distance is defined as a scalar value that is multiplied by the subregion-specific distance cutoffs from 'Cell proximity effects of ageing and rejuvenation'. These unit distances are used as new cutoff distances to compute cell proximity effects. We also analysed spatial gradation of area-restricted cell proximity effects by setting the larger of the two cutoff distances to the unit distance and the smaller cutoff distance to be 15 μm less than the larger cutoff distance, which ensured no overlap of cells defined as 'near' between integer multiples of the cutoff distances.

Activation/inflammation glia signatures and subtype identification

We computed microglia activation scores and oligodendrocyte/OPC inflammation scores by summing the log-normalized expression of all shared genes between gene signature sets curated from several published sets[17,106,107] and the 300 genes in the MERFISH dataset. The microglia activation score consisted of gene expression from *Apoe*, *B2m*, *C1qa*, *Cd69*, *Cd9*, *Il1a*, *Il1b*, *Il6* and *Lyz2*. The oligodendrocyte/OPC inflammation score consisted of gene expression from *C4b*, *Cdkn1a*, *H2-D1*, *Ifit1* and *Stat1*.

To control for activation/inflammation status in the T cell proximity effect, we selected the cutoff for classifying microglia (activated) and oligodendrocyte (inflamed) subtypes as the top 0.2% highest scores since that was the highest percentage cutoff for which there was no statistically significant difference in the distribution of activation/inflammation scores between activated/inflamed cells that were near or far from T cells. We performed all associated proximity effect analysis using the normal and activated/inflamed subtype labels for microglia and oligodendrocytes.

Cell-type perturbation modelling with deep learning

Deep learning approaches such as GNNs can be leveraged to predict the effects of in silico perturbations. For each section in the coronal section dataset, we constructed a global graph connecting neighbouring cells on a given sample using squidpy.gr.spatial_neighbors with delaunay=True[103] and pruned edges connecting neighbouring cells with distance greater than 200 μm. To define local cell graphs, we extracted induced 2-hop subgraphs of the global graph by random sampling of at most 100 centre cells per cell type for T cells and NSCs. To increase the heterogeneity of these local cell graphs, we further augmented these local cell graphs by inducing two-hop subgraphs centred on all cells within the first set of local subgraphs. For each local cell graph, we defined the neighbourhood ageing as the average age acceleration of all cells in the graph. We defined cell (node) features as a one-hot vector for cell type using the 18 cell-type annotations. We trained a GNN model using PyTorch Geometric[108] to predict neighbourhood ageing from the features of a local cell graph. The GNN model consisted of a three-layer graph isomorphism network (GIN), with node embedding updates for each layer modelled by a linear transformation with hidden dimensionality of 16 followed by batch normalization, ReLU transformation, and a final linear transformation with hidden dimensionality of 16. The first two GIN layers were followed by a ReLU transformation and the output of the final GIN layer was globally pooled by addition before linearly transformed to predict neighbourhood ageing. We trained the GNN model using a balanced mean-squared error loss[109], the Adam optimizer[110] with a learning rate of 0.0001, and a batch size of 64 for 50 epochs.

To model 'loss-of-function' perturbations for a given local cell graph, we mutated the centre cell of the graph into a random cell type drawn from a uniform distribution across all cell types in the dataset excluding the original cell type. We performed 'loss-of-function' perturbations for local cell graphs that had T cells and NSCs as centre cells. To model 'gain-of-function' perturbations for a given local cell graph, we replaced the centre cell of the graph with the specified cell type by modifying its node features. We performed 'gain-of-function' perturbations for all local cell graphs and mutated the centre cells to either T cells or NSCs. We excluded 'gain-of-function' perturbations resulting in unperturbed local cell graphs from our analysis (for example, graph with T cell as centre cell replaced by T cell). For both 'loss of function' and 'gain-of-function' experiments, we used endothelial cells as a negative control setting. Using the GNN model, we evaluated the effect of both 'loss-of-function' and 'gain-of-function' perturbations by predicting the neighbourhood ageing for the unperturbed local cell graph and the neighbourhood ageing for the perturbed local cell graph. The effect on neighbourhood ageing was then measured as the unperturbed neighbourhood ageing subtracted from the perturbed neighbourhood ageing (positive values indicating a pro-ageing perturbation and negative values indicating a pro-rejuvenating perturbation).

TISSUE imputation

To augment the 300 genes measured through MERFISH to more than 12,000 genes, we performed uncertainty-aware spatial gene expression imputation, using a method we recently developed, TISSUE[29], as a wrapper around the SpaGE[104] and Tangram[111] imputation algorithms. TISSUE is an algorithm that provides an uncertainty-aware framework for performing differential gene expression and signature analysis on imputed spatial gene expression with marked reductions in false discovery rates compared with other approaches[29]. This imputation approach consists of jointly mapping transcriptomes from our MERFISH study with single-cell RNA-seq datasets collected from mice across multiple ages and containing the brain regions of interest (for example, VEN, CC or STR)[3,4], followed by prediction of new gene expression profiles using the single-cell RNA-seq dataset as reference and differential analysis of gene expression and gene signatures (Extended Data Fig. 12a). The log-normalized gene expression data from the first dissociated single-cell RNA-seq dataset[3] were used for imputation of gene expression for T cells (8,170 genes imputed in total), and log-normalized gene expression data from the second dissociated single-cell RNA-seq dataset[4] were used for imputation of gene expression for all other cell types (12,719 genes imputed in total). We applied the TISSUE algorithm on a subset of the coronal section dataset (see below for details). We used the raw MERFISH counts normalized by cell segmentation volume as input for imputation. We used TISSUE with the SpaGE imputation algorithm[104] and Tangram imputation algorithm[111], under default settings such as 10 folds of cross-validation, 4 stratified gene groups, 1 stratified cell group, and 100 multiple imputations (for hypothesis testing purposes). Evaluation of TISSUE calibration quality and SpaGE/Tangram imputation performance were conducted using the TISSUE software package and associated code[29]. Using cross-validation, we verified that the imputed gene expression values were positively correlated with the actual gene expression values and generally had small absolute prediction errors (Extended Data Fig. 12b).

We filtered cells in the coronal section dataset to include NSCs and T cells, and all target cells labelled ‘near’ or ‘far’ with respect to NSCs or T cells under the proximity effect framework. We re-centred each sample to grid lattice points such that no samples spatially overlap. In addition to ‘near’ and ‘far’ labels, we also labelled each T cell and NSC by the strength of their proximity effects. First, we computed the neighbourhood age acceleration as the average age acceleration of all cells within the maximum subregion distance cutoff for each T cell or NSC. Then, we labelled all T cells with the 50% highest neighbourhood age acceleration as ‘more pro-ageing’ and the remaining T cells as ‘less pro-ageing’, and we labelled all NSCs with the 50% lowest neighbourhood age acceleration as ‘more pro-rejuvenating’ and the remaining NSCs as ‘less pro-rejuvenating’.

TISSUE differential gene expression analysis and pathway enrichment

To uncover potential mediators of T cell and NSC proximity effects, we used a two-step approach. First, we performed unbiased differential gene expression analysis using TISSUE[29] on more than 12,000 imputed genes, with the goal of identifying common genes that were upregulated in cells near key effector cell types (T cells or NSCs) compared with cells far from the same effector cell type and matched by cell type and subregion (that is, the same procedure as for calculating proximity effects). We verified that cells near T cells or NSCs did not include a cell type that was substantially more represented than all other cell types and that all 14 cell types with spatial ageing clocks were present (Supplementary Table 16), and we checked that the variances in imputed gene expression were similar between the comparison groups (Extended Data Fig. 12c). In the second step, to better understand potential mechanisms of action, we performed targeted statistical comparisons of imputed gene signatures using TISSUE and gene expression in the MERFISH datasets for processes related to the most enriched terms from the unbiased analyses in both effector cell types (T cells or NSCs) and target cells (nearby cells).

We used TISSUE to perform uncertainty-aware differential gene expression analysis on the imputed gene expression. TISSUE relies on a multiple imputation framework with statistical guarantees that are only extensible to t-tests (non-parametric TISSUE tests rely on a less rigorously defined P value transformation)[29]. Given the variability in imputation quality, we chose the TISSUE framework, which was well-suited for this task despite some limitations of the t-test. We performed two sets of comparisons using TISSUE two-sided t-test for hypothesis testing of gene signatures. First, we compared gene signature scores between ‘near’ and ‘far’ target cells with respect to either T cells or NSCs. Second, we compared gene signature scores between more pro-ageing and less pro-ageing T cells or between more pro-rejuvenating and less pro-rejuvenating NSCs. We determined significant DEGs as genes with permissive cutoff of $P < 0.05$ from TISSUE two-sample t-tests for both SpaGE and Tangram imputed expression to reduce false discoveries resulting from variability or biases in imputation quality. We further filtered these genes such that the associated TISSUE t-statistic were of the same sign across the tests on SpaGE and Tangram imputations. We did not perform any filtering of genes by the log fold change in imputed gene expression across conditions because unlike the TISSUE P value, the log fold change is not calibrated for uncertainty in spatial gene imputation.

GO biological process (2023) gene set enrichment was performed using the EnrichR framework[112] accessed through gseapy[113] (version 1.0.4). We separated DEGs for each comparison into upregulated DEGs (positive TISSUE t-statistic) and downregulated DEGs (negative TISSUE t-statistic) and used these gene lists as inputs into EnrichR to obtain enrichment statistics for different gene sets. We selected the top five gene sets for each comparison, which were generally representative of all significantly enriched gene sets.

Test for equal variances between groups

We performed Levene’s test for equal variances using the scipy.stats.levene implementation with default settings (center = median, proportiontocut = 0.05) for analyses relying on Cohen’s d or variations of the Student’s t-test. Levene’s test was applied to test for equal variance of age acceleration of ‘near’ and ‘far’ cell groupings for each cell proximity effect. Levene’s test was also applied to test for equal variance of TISSUE (SpaGE) imputed gene expression of ‘near’ and ‘far’ cell groupings with respect to T cells and NSCs. In both cases, the number of samples between the compared groups was equal, a setting in which Cohen’s d and Student’s t-test are usually robust against unequal variances across groups.

TISSUE gene signature scores

We further modified the hypothesis testing framework in TISSUE to perform testing for gene signature scores (sum of imputed gene expression values across all genes in a GO gene set). We have made this modification publicly available in the TISSUE package[29] as tissue.downstream.multiple_imputation_gene_signature and we set n_imputations=100 for all gene signature tests. For imputed gene signature scores, we performed the same two sets of comparisons as outlined in ‘TISSUE differential gene expression analysis and pathway enrichment’. For similar comparisons involving expression of individual genes (for example, *Bst2*, *Stat1*, *Cd9* and *Vegfa*) instead of gene signatures, we used the measured (log-normalized) gene expression values in the MERFISH dataset instead of imputed values.

Immunofluorescence staining of brain sections

All immunostainings were performed on male C57BL/6JN mice at the indicated ages. Mice were sedated with 0.8 ml 2.5% vol/vol Avertin (Sigma-Aldrich, T48402-25G) in PBS (Corning, 21-040-CV) and perfused via the left ventricle of the heart with 5 ml of PBS (Corning, 21-040-CV) with heparin sodium salt (50 U ml^{-1}, Sigma-Aldrich, H3149-50KU) to remove circulating blood cells followed by 4% paraformaldehyde (Electron Microscopy Sciences, 15714) in PBS. Brains were post-fixed overnight in 4% paraformaldehyde (Electron Microscopy Sciences, 15714) and then dehydrated in 30% sucrose (Sigma-Aldrich, S3929) for 72 h. Brains were embedded in OCT compound (Fisher Healthcare Tissue Plus, 4585), sectioned in 20-μm coronal sections using a cryostat (Leica, CM3050S), and then mounted on electrostatic glass slides (Fisher Scientific, 12-550-15). Coronal sections at a similar depth to the MERFISH coronal sections were collected. For the following steps, all brain sections were processed simultaneously within each experiment. For immunofluorescence staining, brain sections were washed with PBS for 5 min, permeabilized in ice-cold methanol with 0.1% Triton X-100 (Fisher Scientific, BP151) for 15 min, and washed 3 times with PBS for 5 min. We performed antigen retrieval by placing the brain sections in 10 mM sodium citrate buffer (pH 6.0; 2.94 g Tri-sodium citrate dihydrate (Sigma-Aldrich, S1804) in 1,000 ml milliQ H_2O adjusted to pH 6.0 with 1 N HCl) + 0.05% Tween-20 (Sigma-Aldrich, P1379-1L) at 85 °C in a water bath for 2 h. Brain sections in buffer were cooled to room temperature for 20 min and then washed twice with PBS for 3 min. Sections were blocked for 30 min at room temperature with block buffer consisting of 5% normal donkey serum (ImmunoReagents, SP-072-VX10) and 1% BSA (Sigma, A7979) in PBS. Primary antibodies were diluted in blocking buffer and primary antibody staining was performed overnight at 4 °C. Primary antibodies used were as follows: anti-GFAP (1:1,000 dilution, Abcam, ab53554), anti-Ki67 (1:500 dilution, Thermo Fisher Scientific, 14-5698-82), anti-DCX (1:500 dilution, Millipore Sigma, AB2253), anti-EGFR (1:200 dilution, Millipore Sigma, 06-847), anti-STAT1 (1:500 dilution, Cell Signaling Technology, 14994), anti-CD3 (1:500, Abcam, ab11089), anti-S100A6 (1:500, Abcam, ab181975), anti-CD9 (1:100, Thermo Fisher, eBioKMC8 (KMC8)), anti-CPT1A (1:200, Abcam, ab128568). Sections were washed 3 times with PBS and 0.2% Tween-20 for 10 min at room temperature followed by twice with PBS for 15 min. Secondary antibodies were diluted in blocking buffer and secondary antibody staining was performed for 2 h at room temperature. Secondary antibodies used were as follows: Donkey anti-Goat 647 (1:500 dilution, Invitrogen, A21447), Donkey anti-Rabbit 488 (1:500 dilution, Invitrogen, A-21206), Donkey anti-Guinea pig 594 (1:500 dilution, Jackson ImmunoResearch, 706-585-148), Donkey anti-Rat 647 (1:500 dilution, Invitrogen, A48272), Donkey anti-Rat 488 (1:500, Invitrogen, A21208), Donkey anti-Mouse 647 (1:500, Invitrogen, A31571), Donkey anti-Rabbit 568 (1:500, Invitrogen, A10042). DAPI (1:500, Thermo Fisher, 62248) was added during secondary antibody staining. Sections were washed 3 times with PBS and 0.2% Tween-20 for 10 min followed by 3 times with PBS for 5 min. Sections were mounted with ProLong Gold Antifade Mountant with DAPI (Thermo Fisher, P36931) and a coverslip.

For immunofluorescence experiments corresponding to spatiotemporal marker expression, images were acquired on a Zeiss LSM 900 with Zeiss ZEN Blue 3.0 software or a Zeiss LSM 980 confocal microscope with Zeiss ZEN Blue 3.3 software using a 10× objective and automatic tiling of entire coronal brain sections. The same equipment and microscope acquisition settings were used for different brain sections with the same antibody panel. Tile images were stitched using Zeiss ZEN Blue software. Image brightness and contrast were adjusted in ImageJ (1.53n) to enhance visualization with the same settings applied to all images shown for each antibody staining panel.

For immunofluorescence experiments corresponding to T cell and NSC proximity effects, images were acquired with a 60× objective on a Nikon Eclipse Ti confocal microscope equipped with a Zyla sCMOS camera (Andor) and NIS-Elements software (AR 4.30.02, 64-bit). For immunofluorescence experiment corresponding to T cell proximity effects, we acquired at least two images containing T cells and at least one image without any T cells from each of four anatomic regions (CC, CTX, striatum and adjacent regions (STR) and VEN) for each brain section. The same image acquisition settings were used for all brain sections in this experiment. For immunofluorescence experiment corresponding to NSC proximity effects, we acquired individual images tiling the entire right and left VEN for each brain section. The same image acquisition settings were used for all brain sections in this experiment.

Immunofluorescence quantification of T cell proximity effect via interferon response

Immunofluorescence imaging was performed on brain sections from old (28 months) mice. All cell segmentations and cell-type annotations were performed using automated pipelines in QuPath 0.5.1. For all images, cell nuclei were automatically segmented based on DAPI intensity, and then nuclear segmentation masks were expanded by 2 μm to define the cell segmentations. Cells were labelled as CD3$^+$ using a manually determined threshold for mean cell CD3 intensity. The same threshold was used across all images and CD3$^+$ cells were annotated as T cells. For all CD3$^-$ cells, we defined cells as ‘near’ if they were located within 50 μm of a T cell based on the centroids of cell segmentations and otherwise defined them as ‘not near’. For each anatomic region (CC, CTX, STR and VEN) and each cell proximity definition (‘near’ or ‘not near’), we quantified the mean STAT1 intensity by averaging the mean cell STAT1 intensity across each section and then by averaging these values across each mouse (3–5 coronal sections per mouse, 8 mice per condition). We were unable to discover any T cells in the STR region for one of the eight mice due to low CD3 intensity in its brain sections. The mean STAT1 intensity values were normalized for each independent experiment by dividing them by the corresponding mean ‘not near’ STAT1 intensity.

Immunofluorescence quantification of NSC proximity effect via exosomes and fatty acid oxidation pathway

Immunofluorescence imaging was performed on brain sections from young (3.5 months) mice. All cell segmentations and cell-type annotations were performed using automated pipelines in QuPath 0.5.1. For all images, regions of interest were defined along the lining of the VEN. Within these regions of interest, cell nuclei were segmented based on DAPI intensity, and then nuclear segmentation masks were expanded by 2 μm to define the cell segmentations. Cells were labelled as S100A6$^+$ using a manually determined threshold for mean nuclear S100A6 intensity. The same threshold was used across all images and S100A6$^+$ cells were annotated as NSCs and other cells were annotated as non-NSCs. To compare CD9 intensity between S100A6$^+$ and S100A6$^-$ cells, we quantified the mean CD9 intensity by averaging the mean cell CD9 intensity across each section and then by averaging these values across each mouse (three coronal sections per mouse, five mice per condition). The mean CD9 intensity values were normalized for each independent experiment by dividing them by the CD9 intensity in S100A6$^-$ cells. For all cells, we defined cells as ‘near’ if they were located within 20 μm of a NSC (excluding itself) based on the centroids of cell segmentations and otherwise defined them as ‘not near’. To compare CPT1A intensity between ‘near’ and ‘not near’ cells, we quantified the mean CPT1A intensity by averaging the mean cell CPT1A intensity across each section and then by averaging these values across each mouse (three coronal sections per mouse, five mice per condition). The mean CPT1A intensity values were normalized for each independent experiment by dividing them by the corresponding mean ‘not near’ CPT1A intensity. To examine the correlation between CPT1A intensity of all ‘near’ cells and the CD9 intensity of the nearest NSC, we matched all ‘near’ cells to their nearest NSC defined by the minimum non-zero Euclidean distance between centroids and computed the Pearson and Spearman correlation between the paired CPT1A and CD9 intensities. To check the robustness of the correlation analysis to technical variability, we also re-imaged all sections using a Zeiss LSM 900 with Zeiss ZEN Blue 3.0 software and performed the same image analysis. Results were highly consistent with the reported findings.

Statistics and reproducibility

For measures of Pearson and Spearman correlation and their associated test statistics (*P* values and 95% confidence intervals), we used the implementation from scipy.stats.pearsonr and scipy.stats.spearmanr. For most comparisons, we used the two-sided Mann–Whitney tests according to the implementation from scipy.stats.mannwhitneyu. We used Cohen's *d* for cell proximity effect analysis in which similar variances in age acceleration were typically observed between 'near' and 'far' cell groups (Extended Data Fig. 9a). GO biological process enrichment analysis was performed with topGO[101] (R package version 2.54.0) using Fisher's exact test for all Biological Process terms and using all other genes measured by MERFISH as background. For other data analysis and plotting tasks, we used Python (3.8.13), pandas (1.4.2), matplotlib (3.5.1), seaborn (0.12.2), numpy (1.21.6), scipy (1.8.0), sklearn (1.0.2), anndata (0.8.0), scanpy (1.9.1), squidpy (1.1.2), tissue-sc (0.0.2), tangram-sc (1.0.3), spage (accessed September 1, 2022), gseapy (1.0.4), umap-learn (0.5.3) and statsmodels (0.13.2).

For the gene signature and differential gene expression analysis with imputed spatial gene expression, we used the two-sample two-sided TISSUE *t*-test with specifications outlined in the 'TISSUE imputation' section. The TISSUE *t*-test is the only statistical test that considers uncertainty in imputed gene expression and to further decrease false discoveries, we selected genes with consistent differential expression across two imputation methods (SpaGE[104] and Tangram[111]). For most comparisons using the TISSUE *t*-test, variances in imputed gene expression were similar across groups (Extended Data Fig. 12c). We did not perform multiple hypothesis correction of *P* values for the targeted gene signature analysis using TISSUE imputation because gene signatures were manually selected. Reported *P* values are from the SpaGE imputed gene expression. For pathway enrichment for DEGs identified with TISSUE and imputed gene expression, we used gseapy.enrichr with the 'GO_Biological_Process_2023' gene set, 'mouse' as the organism, and all imputed genes as background.

Technical reproducibility of MERFISH measurements was confirmed by profiling consecutive sections in the 140-gene MERFISH dataset[29] (Extended Data Fig. 1a). For the MERFISH (300 gene) ageing dataset, we combined two cohorts ($n = 10$ mice for each cohort) and confirmed reproducibility of spatial ageing clock performance and generalization of key findings within each cohort (Extended Data Fig. 5b,c and Supplementary Fig. 6d,e). All experimental validation was performed on independent mice. Technical reproducibility of immunofluorescence image analysis for the NSC proximity effect mediation through exosomes and fatty acid oxidation was assessed with re-imaging of the same sections by a different experimentalist with a different microscope. Two separate immunofluorescence staining and imaging experiments for T cell proximity effect mediated through interferon response were performed and combined for analysis, with intensities normalized against each experiment independently.

Reporting summary

Further information on research design is available in the Nature Portfolio Reporting Summary linked to this article.

Data availability

The processed MERFISH spatial transcriptomics datasets generated for this study are available at https://doi.org/10.5281/zenodo.13883177 (ref. 114). The ageing and LPS injection dataset and the associated single-nuclei RNA-seq dataset were accessed from https://cellxgene.cziscience.com/collections/31937775-0602-4e52-a799-b6acdd2bac2e. The single-cell RNA-seq ageing dataset of whole mouse brain was accessed from https://portals.broadinstitute.org/single_cell/study/aging-mouse-brain. The Alzheimer's model dataset was accessed from https://singlecell.broadinstitute.org/single_cell/study/SCP1375. The multiple sclerosis model dataset with global demyelination via experimental autoimmune encephalomyelitis was accessed from https://zenodo.org/records/8037425. The localized demyelination injury dataset was accessed from Gene Expression Omnibus under accession number GSE202638. The single-cell RNA-seq datasets for the subventricular zone across lifespan were accessed from https://doi.org/10.5281/zenodo.7145398. The GenAge database was accessed at https://genomics.senescence.info/genes/models.html. Source data are provided with this paper.

Code availability

All code used for data analysis and experiments is available at https://github.com/sunericd/spatial_aging_clocks. The Python package for deploying spatial ageing clocks to single-cell transcriptomics datasets and performing cell proximity effect analysis for spatial transcriptomics is available at https://github.com/sunericd/SpatialAgingClock.

80. Carey, B. W., Markoulaki, S., Beard, C., Hanna, J. & Jaenisch, R. Single-gene transgenic mouse strains for reprogramming adult somatic cells. *Nat. Methods* **7**, 56–59 (2010).
81. Blackmore, D. G. et al. An exercise "sweet spot" reverses cognitive deficits of aging by growth-hormone-induced neurogenesis. *iScience* **24**, 103275 (2021).
82. McKenzie, A. T. et al. Brain cell type specific gene expression and co-expression network architectures. *Sci Rep.* **8**, 8868 (2018).
83. Louveau, A. et al. CNS lymphatic drainage and neuroinflammation are regulated by meningeal lymphatic vasculature. *Nat. Neurosci.* **21**, 1380–1391 (2018).
84. Llorens-Bobadilla, E. et al. Single-cell transcriptomics reveals a population of dormant neural stem cells that become activated upon brain injury. *Cell Stem Cell* **17**, 329–340 (2015).
85. Dulken, B. W., Leeman, D. S., Boutet, S. C., Hebestreit, K. & Brunet, A. Single-cell transcriptomic analysis defines heterogeneity and transcriptional dynamics in the adult neural stem cell lineage. *Cell Rep.* **18**, 777–790 (2017).
86. Li, X. et al. Single-cell transcriptomic analysis of the immune cell landscape in the aged mouse brain after ischemic stroke. *J. Neuroinflammation* **19**, 83 (2022).
87. Morgan, D. & Tergaonkar, V. Unraveling B cell trajectories at single cell resolution. *Trends Immunol.* **43**, 210–229 (2022).
88. Ying, K. et al. Causality-enriched epigenetic age uncouples damage and adaptation. *Nat. Aging* **4**, 231–246 (2024).
89. Nelson, P. G., Promislow, D. E. L. & Masel, J. Biomarkers for aging identified in cross-sectional studies tend to be non-causative. *J. Gerontol. Ser. A* **75**, 466–472 (2020).
90. Cebrian-Silla, A. et al. Single-cell analysis of the ventricular-subventricular zone reveals signatures of dorsal and ventral adult neurogenesis. *eLife* **10**, e67436 (2021).
91. Jambusaria, A. et al. Endothelial heterogeneity across distinct vascular beds during homeostasis and inflammation. *eLife* **9**, e51413 (2020).
92. Da Mesquita, S. et al. Functional aspects of meningeal lymphatics in ageing and Alzheimer's disease. *Nature* **560**, 185–191 (2018).
93. Alves de Lima, K. et al. Meningeal γδ T cells regulate anxiety-like behavior via IL-17a signaling in neurons. *Nat. Immunol.* **21**, 1421–1429 (2020).
94. Ruetz, T. J. et al. CRISPR–Cas9 screens reveal regulators of ageing in neural stem cells. *Nature* **634**, 1150–1159 (2024).
95. Argraves, W. S. & Drake, C. J. Genes critical to vasculogenesis as defined by systematic analysis of vascular defects in knockout mice. *Anat. Rec. A.* **286**, 875–884 (2005).
96. Hartman, A. & Satija, R. Comparative analysis of multiplexed in situ gene expression profiling technologies. *eLife* https://doi.org/10.7554/eLife.96949.1 (2024).
97. Wolock, S. L., Lopez, R. & Klein, A. M. Scrublet: computational identification of cell doublets in single-cell transcriptomic data. *Cell Syst.* **8**, 281–291.e9 (2019).
98. Wolf, F. A., Angerer, P. & Theis, F. J. SCANPY: large-scale single-cell gene expression data analysis. *Genome Biol.* **19**, 15 (2018).
99. Chari, T. & Pachter, L. The specious art of single-cell genomics. *PLoS Comput. Biol.* **19**, e1011288 (2023).
100. Lause, J., Berens, P. & Kobak, D. The art of seeing the elephant in the room: 2D embeddings of single-cell data do make sense. *PLoS Comput. Biol.* **20**, e1012403 (2024).
101. Alexa, A. & Rahnenfuhrer, J. topGO: Enrichment analysis for Gene Ontology. R package version 2.54.0 (2016).
102. Pedregosa, F. et al. Scikit-learn: machine learning in Python. *J. Mach. Learn. Res.* **12**, 2825–2830 (2011).
103. Palla, G. et al. Squidpy: a scalable framework for spatial omics analysis. *Nat. Methods* **19**, 171–178 (2022).
104. Abdelaal, T., Mourragui, S., Mahfouz, A. & Reinders, M. J. T. SpaGE: spatial gene enhancement using scRNA-seq. *Nucleic Acids Res.* **48**, e107 (2020).
105. Fang, R. et al. Conservation and divergence of cortical cell organization in human and mouse revealed by MERFISH. *Science* **377**, 56–62 (2022).
106. Madeddu, S. et al. Identification of glial activation markers by comparison of transcriptome changes between astrocytes and microglia following innate immune stimulation. *PLoS ONE* **10**, e0127336 (2015).
107. Pandey, S. et al. Disease-associated oligodendrocyte responses across neurodegenerative diseases. *Cell Rep.* **40**, 111189 (2022).

108. Fey, M. & Lenssen, J. E. Fast graph representation learning with PyTorch geometric. In *Proc. ICLR 2019 Workshop on Representation Learning on Graphs and Manifolds* (ICLR, 2019).
109. Ren, J., Zhang, M., Yu, C. & Liu, Z. Balanced MSE for imbalanced visual regression. In *Proc. IEEE/CVF Conference on Computer Vision and Pattern Recognition (CVPR)* (ed. O'Conner, L.) 7926–7935 (IEEE, 2022).
110. Kingma, D. P. & Ba, J. Adam: a method for stochastic optimization. In *Proc. International Conference on Learning Representations* (ICLR, 2015).
111. Biancalani, T. et al. Deep learning and alignment of spatially resolved single-cell transcriptomes with Tangram. *Nat. Methods* **18**, 1352–1362 (2021).
112. Xie, Z. et al. Gene set knowledge discovery with Enrichr. *Curr. Protoc.* **1**, e90 (2021).
113. Fang, Z., Liu, X. & Peltz, G. GSEApy: a comprehensive package for performing gene set enrichment analysis in Python. *Bioinformatics* **39**, btac757 (2023).
114. Sun, E. Processed MERFISH datasets for brain aging (coronal, sagittal) and rejuvenation (exercise, partial reprogramming). *Zenodo* https://doi.org/10.5281/zenodo.13883177 (2024).

Acknowledgements The authors thank members of the Brunet and Zou laboratories, especially Z. Huang, C. Bedbrook, J. Chen and J. Na for helpful discussion and assistance; C. Bedbrook for independent checking of the code; B. Engelhardt, L. Jerby and M. Snyder for helpful discussion; the Vizgen laboratory service team, especially J. He, Y. Cai, N. DiNapoli and B. Wang for technical assistance; and the Stanford Wu Tsai Neuroscience Microscopy Service. Support was provided by NSF Graduate Research Fellowship (to E.D.S.), P.D. Soros Fellowship for New Americans (to E.D.S.), Knight-Hennessy Scholars Program (to E.D.S.), NSF CAREER 1942926 (to J.Z.), grants from Silicon Valley Foundation (to J.Z.), Chan Zuckerberg Biohub–San Francisco Investigator program (to J.Z. and A.B.), Chan Zuckerberg Initiative award (to A.B.), NIH grant P01AG036695 (to A.B. and T.A.R.), NIH grant R01AG071711 (to A.B.), the Milky Way Research Foundation (to A.B.), Simons Foundation grant (to A.B.), the Knight Initiative for Brain Resilience (to A.B.), and a generous gift from M. and T. Barakett (to A.B.).

Author contributions E.D.S., J.Z. and A.B. planned the study. E.D.S. generated all datasets and performed all experiments and analyses, with contributions from other authors indicated below. M.H., O.Y.Z. and L.X. assisted with immunofluorescence experiments. O.Y.Z. assisted with sample collection for the exercise experiment. N.R. performed GO term enrichment and regional gene expression change analysis and performed independent code checking. L.X. assisted with study design and sample collection for the partial reprogramming experiment. O.Y.Z., L.X. and P.N.N. assisted with sample collection for the ageing dataset. L.L. and T.A.R. provided mice from the exercise experiment. E.D.S., J.Z. and A.B. wrote the manuscript, and all authors provided feedback.

Competing interests A.B. is a scientific advisory board member of Calico. The other authors declare no competing interests.

Additional information

Supplementary information The online version contains supplementary material available at https://doi.org/10.1038/s41586-024-08334-8.

Correspondence and requests for materials should be addressed to James Zou or Anne Brunet.

Peer review information *Nature* thanks Johannes Köster and the other, anonymous, reviewer(s) for their contribution to the peer review of this work. Peer review reports are available.

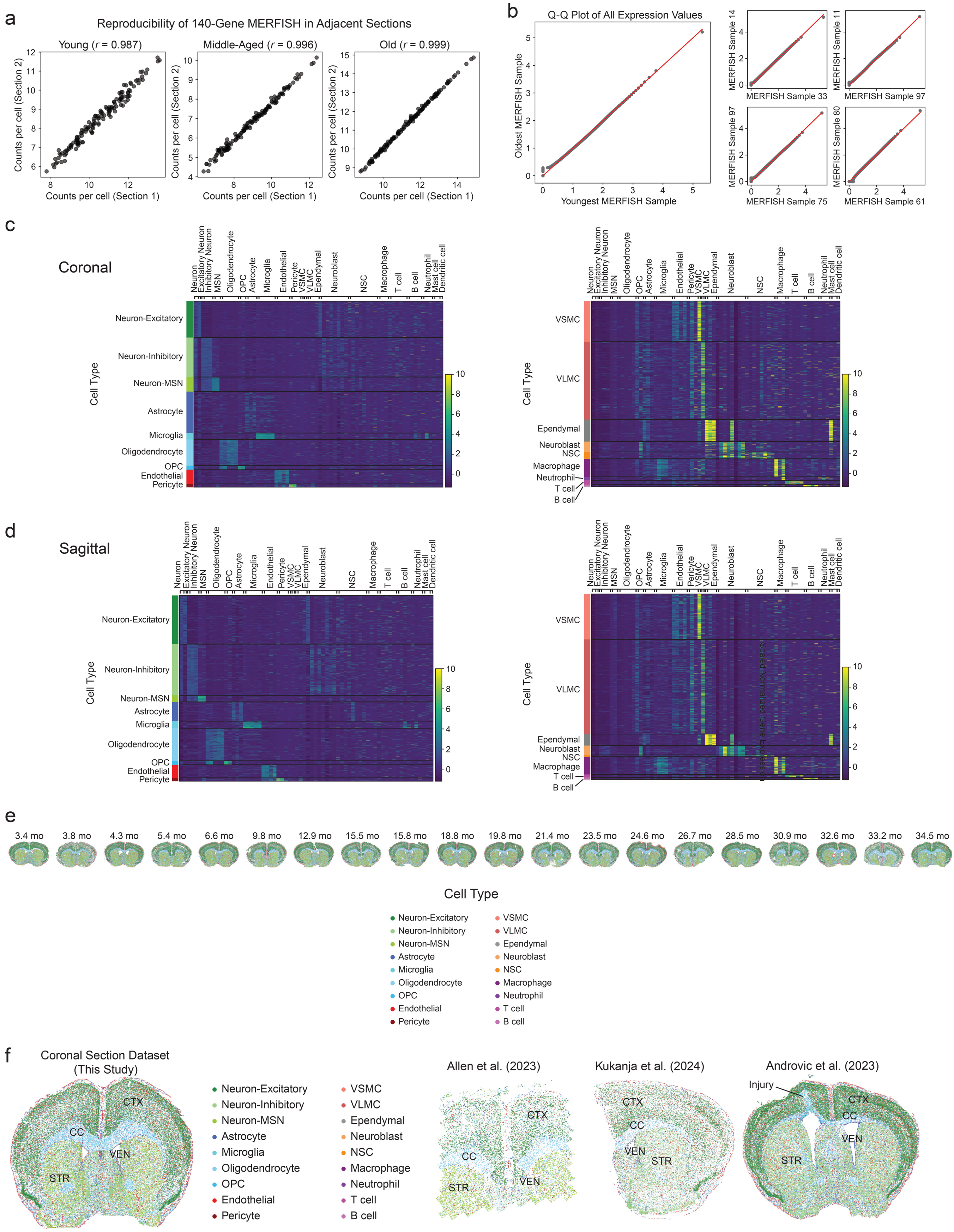

Extended Data Fig. 1 | See next page for caption.

Extended Data Fig. 1 | MERFISH data reproducibility and external validation. **a**, Reproducibility plot of individual genes by their counts per cell between two adjacent coronal sections in the 140-gene MERFISH dataset. Pearson correlation between the gene counts per cell of the two sections is noted in parentheses. **b**, Q-Q (quantile-quantile) plot of all log-normalized expression values across all cells and genes in the MERFISH data of the youngest mouse (3.4 months) compared to the oldest mouse (34.5 months) in the coronal sections dataset (left) and for four randomly selected pairs of mice from the coronal sections dataset (right). **c,d**, Heatmaps showing the scaled log-normalized expression of key cell type marker genes for different cell types (columns) and grouped by the identified cell type clusters (rows) for **(c)** the coronal sections of the aging study and **(d)** the sagittal sections of the aging study. **e**, Scatter plot of cells by their spatial coordinates across all coronal sections and ages with cells colored by cell type. **f**, Scatter plot of cells by their spatial coordinates with cells colored by cell type for representative coronal sections from our coronal section dataset (leftmost) and each of three publicly available spatial transcriptomics datasets of adult mouse brain (coronal brain sections). Regions are labeled for each dataset: cortex (CTX), striatum and adjacent regions (STR), corpus callosum (CC), lateral ventricle (VEN), and injury site (arrow).

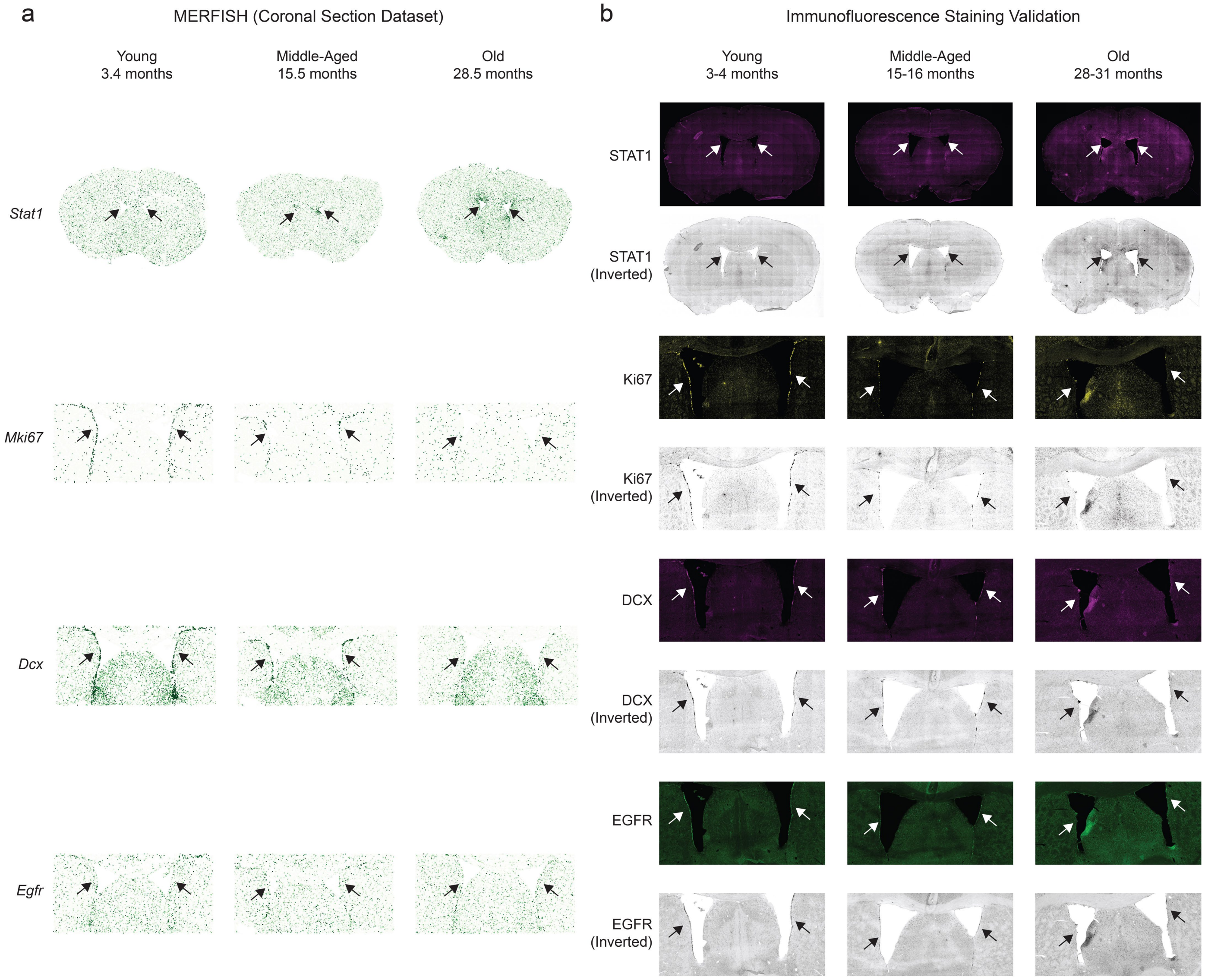

Extended Data Fig. 2 | Validation of spatiotemporal gene expression in the MERFISH panel by immunofluorescence staining. a, MERFISH coronal section dataset: Scatter plot of cells by their spatial coordinates across all sections for three ages (young 3.4 months, middle-aged 15.8 months, old 28.5 months) with cells colored by scaled log-normalized gene expression of key marker genes in the MERFISH coronal section dataset for four genes (*Stat1*, *Mki67*, *Dcx*, *Egfr*). Stat1 is an interferon-response gene. *Mki67* is a cell proliferation marker gene. *Dcx* is a neuroblast marker gene. *Egfr* is a neural stem cell marker gene. The whole coronal sections are shown for *Stat1*. The areas around the lateral ventricles are shown for *Mki67*, *Dcx*, and *Egfr*. Arrows indicate the subventricular zone neurogenic niche in the lateral ventricles. **b**, Immunofluorescence validation: Immunofluorescence staining of perfused mouse brain sections from male mice at three ages (young 3-4 months, middle-aged 15-16 months, old 28-31 months) for protein markers corresponding to each of the select MERFISH genes. The whole coronal section is shown for STAT1. The area around the lateral ventricles is shown for Ki67, DCX, and EGFR. Arrows indicate the subventricular zone neurogenic niche in the lateral ventricles. Shown are the original immunofluorescence images and the inverted grayscale images (to provide a more direct comparison with the MERFISH data).

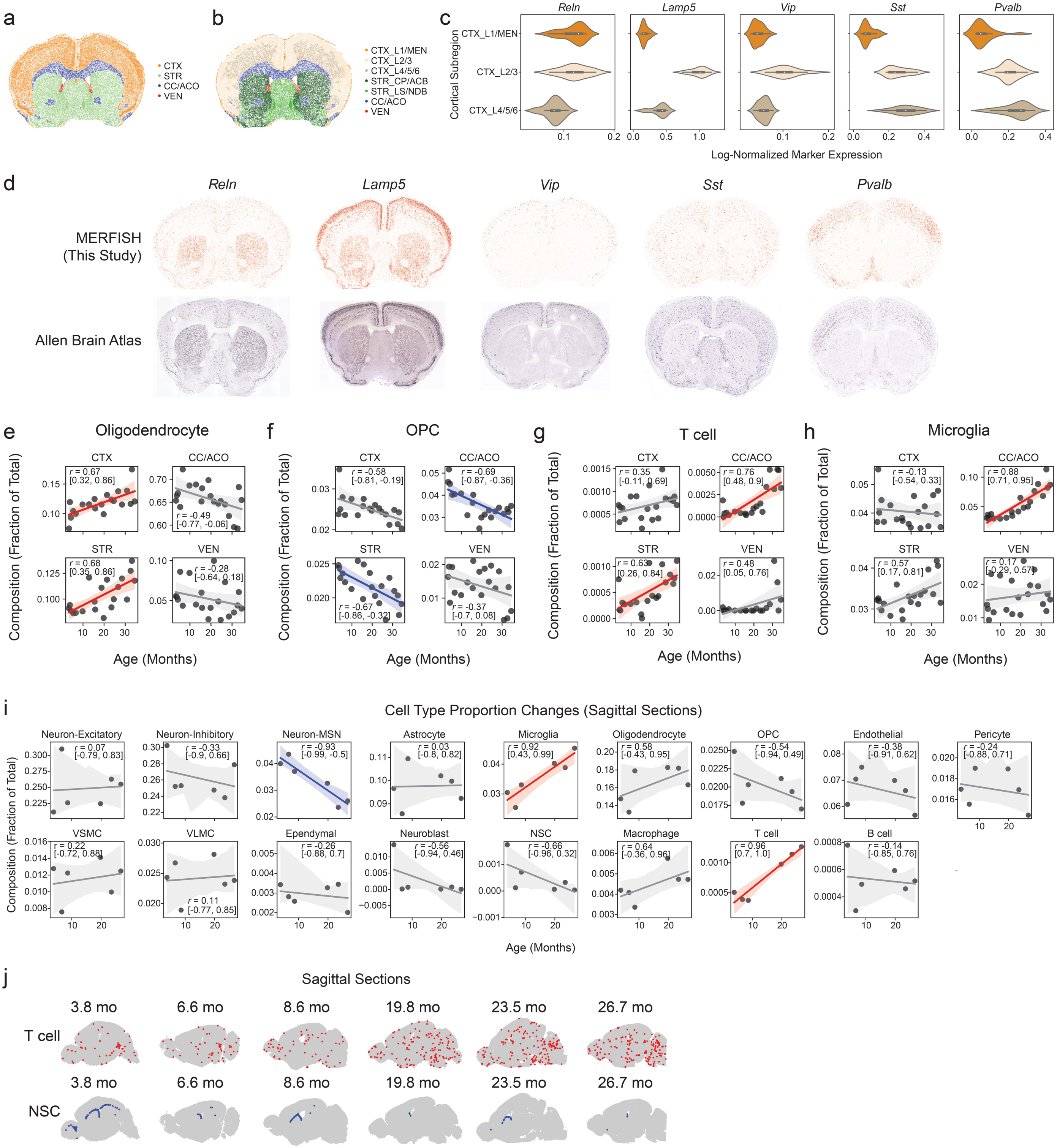

Extended Data Fig. 3 | See next page for caption.

Extended Data Fig. 3 | Subregion annotation and cell type composition changes. **a**, Scatter plot of cells by their spatial coordinates in an example coronal section with cells colored by region. **b**, Scatter plot of cells by their spatial coordinates in the example coronal section with cells colored by subregion. **c**, Violin plots showing log-normalized gene expression of five different cortical layer or neuronal subtype markers across all cells in different subregions of the cortex in the coronal section dataset. The markers include: *Reln* (indicative of L1), *Lamp5* (indicative of L2/3 together with L1), *Vip* (indicative of L2/3), *Sst* (indicative of L5 and L6 together with L2/3), and *Pvalb* (indicative of L5 and L6 together with L2/3). The line indicates the median, the inner box corresponds to 25th and 75th quartiles, and the whiskers span up to 1.5 times the interquartile range of log-normalized gene expression values. **d**, Scatter plot of cells by their spatial coordinates in the example coronal section with cells colored by their log-normalized expression (upper row) compared to mouse brain coronal sections from the Allen brain in situ hybridization atlas at https://mouse.brain-map.org/ (credit: Allen Institute) (bottom row) for five different cortical layer or neuronal markers. **e-h**, Region-specific composition changes in the coronal section dataset across the four regions (cortex, striatum and adjacent regions, corpus callosum and anterior commissure, lateral ventricles). Line and error bands represent regression line of best fit and corresponding 95% confidence interval. Pearson correlations between cell type composition and age are reported along with their 95% confidence interval. Strong increases in cell type proportion with age are in red and strong decreases in cell type proportion with age are in blue (see Methods). Shown are plots for **(e)** oligodendrocytes, **(f)** oligodendrocyte progenitor cells (OPCs), **(g)** T cells, and **(h)** microglia. **i**, Global cell type composition changes with each dot representing an individual mouse in the sagittal section dataset with the same plotting and statistical parameters as in (e-h). **j**, Scatter plot of cells by their spatial coordinates across all ages for all sagittal sections with cells colored by cell type: T cell (red), neural stem cell (NSC) (blue), other cell type (gray).

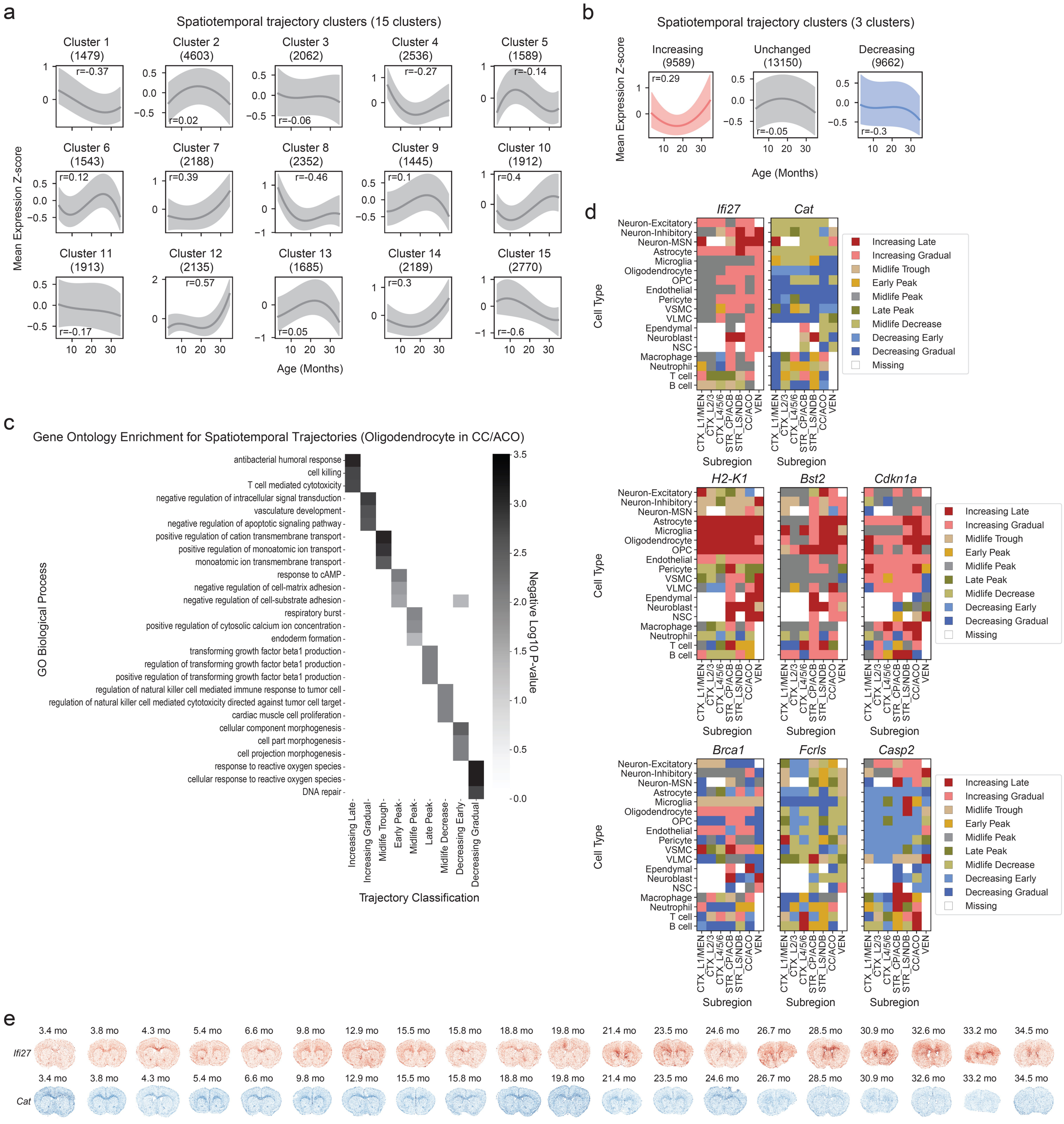

Extended Data Fig. 4 | Gene expression changes and trajectories with age. **a,b**, Smoothed median and interquartile range (error band) of the mean gene expression z-scores across age of all gene, cell type, and subregion combinations split into k clusters (determined by k-means clustering) (see Methods) for **(a)** $k = 15$ and **(b)** $k = 3$. Pearson correlation (r) between median gene expression z-score and age is shown, and the number of trajectories within each cluster is noted inside parentheses. **c**, Heatmap of GO biological process terms with color scale corresponding to negative log10 P-value from Fisher's exact test for the top three terms that are significantly enriched for MERFISH genes in each of the nine annotated gene trajectory clusters for oligodendrocytes in the corpus callosum and anterior commissure region, which corresponds to an abundant cell type in the region with the greatest gene expression change with age (Supplementary Fig. 1c). See Supplementary Table 9 for all GO biological process enrichment results. **d**, Heatmaps showing spatiotemporal trajectory cluster membership across all subregions and cell types for select genes with distinct patterns: interferon gene *Ifi27* (broad "Increasing Gradual"), antioxidant enzyme gene *Cat* (cell type-specific "Decreasing Gradual"), major histocompatibility complex protein-encoding gene *H2-K1* (cell type-specific "Increasing Late"), interferon-response gene *Bst2* (mixed "Increasing Late" and "Increasing Gradual"), cell senescence marker *Cdkn1a* (broad "Increasing Gradual"), DNA damage repair gene *Brca1* (broad "Decreasing Gradual" with "Increasing Gradual" in some cell types), Fc receptor gene *Fcrls* (cell type-specific "Decreasing Gradual"), and cellular apoptosis gene *Casp2* (cell type-specific "Decreasing Early" and "Increasing Gradual"). **e**, Scatter plot of cells by their spatial coordinates across all coronal sections and ages with cells colored by scaled log-normalized gene expression of *Ifi27* (red) and *Cat* (blue).

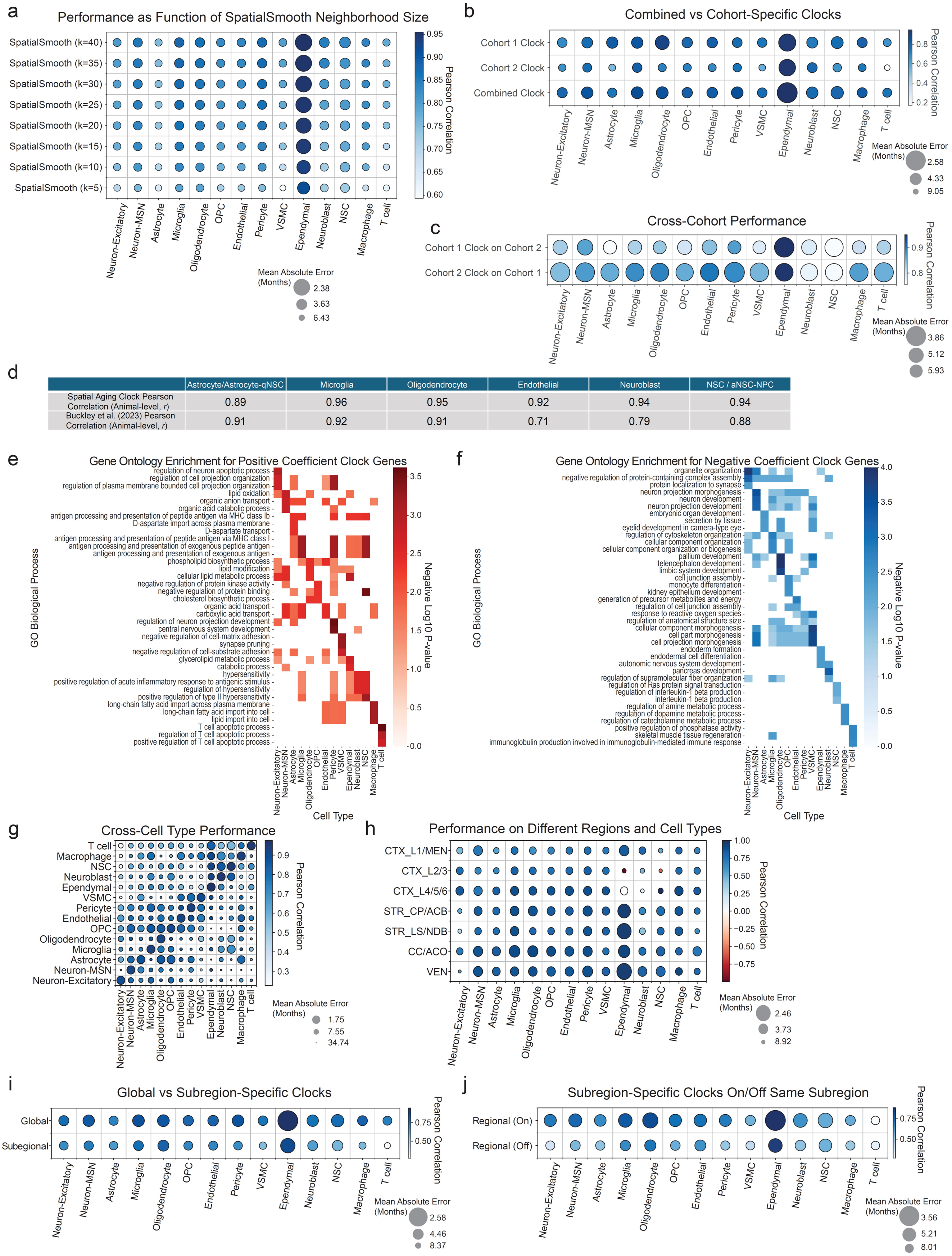

	Astrocyte/Astrocyte-qNSC	Microglia	Oligodendrocyte	Endothelial	Neuroblast	NSC / aNSC-NPC
Spatial Aging Clock Pearson Correlation (Animal-level, *r*)	0.89	0.96	0.95	0.92	0.94	0.94
Buckley et al. (2023) Pearson Correlation (Animal-level, *r*)	0.91	0.92	0.91	0.71	0.79	0.88

Extended Data Fig. 5 | See next page for caption.

Extended Data Fig. 5 | Specificity and robustness of spatial aging clocks. **a-c**, Dot plots evaluating the predictive performance of aging clocks in various contexts. Colors correspond to Pearson correlation between predicted age and actual age and the size of the dots are inversely related to the mean absolute error between predicted age and actual age. Shown are comparisons for **(a)** spatial aging clocks trained and evaluated using different numbers of nearest neighbors in the SpatialSmooth processing step; **(b)** spatial aging clocks trained and evaluated on the two independent cohorts ($n = 10$ per cohort) in the coronal section dataset compared to the spatial aging clock trained on the full (combined) dataset; **(c)** spatial aging clocks trained on one of the independent cohorts ($n = 10$ per cohort) in the coronal section dataset and evaluated on the other independent cohort. **d**, Table comparing Pearson correlation of median predicted age and actual age of individual mice between the spatial aging clocks and existing single-cell RNA-seq aging clocks for six shared cell types. Cross-validation was used to generate predicted ages for both clocks within their respective training datasets. **e,f**, Heatmaps of GO biological process terms with color scale corresponding to negative log10 *P*-value from Fisher's exact test for **(e)** the top three terms that are significantly enriched for genes with positive coefficients per cell type-specific spatial aging clock and **(f)** the top three terms that are significantly enriched for negative coefficients per cell type-specific spatial aging clock. **g-j**, Dot plots evaluating the predictive performance of aging clocks in various contexts. Colors correspond to Pearson correlation between predicted age and actual age and the size of the dots are inversely related to the mean absolute error between predicted age and actual age. Shown are comparisons for **(g)** cell type-specific spatial aging clocks applied to predict age for all other cell types in the coronal section dataset; **(h)** spatial aging clocks evaluated within each of the subregions in the coronal section dataset; **(i)** spatial aging clocks (Global) and subregion-specific spatial aging clocks (Regional) applied to all cells in the coronal section dataset; **(j)** subregion-specific aging clocks applied to all cells within the same subregion (On) compared to all cells in other subregions (Off). The largest mean absolute errors are observed in the off-diagonal elements of panel **g** (for example in comparison to panel **h**, which generally had lower mean absolute errors).

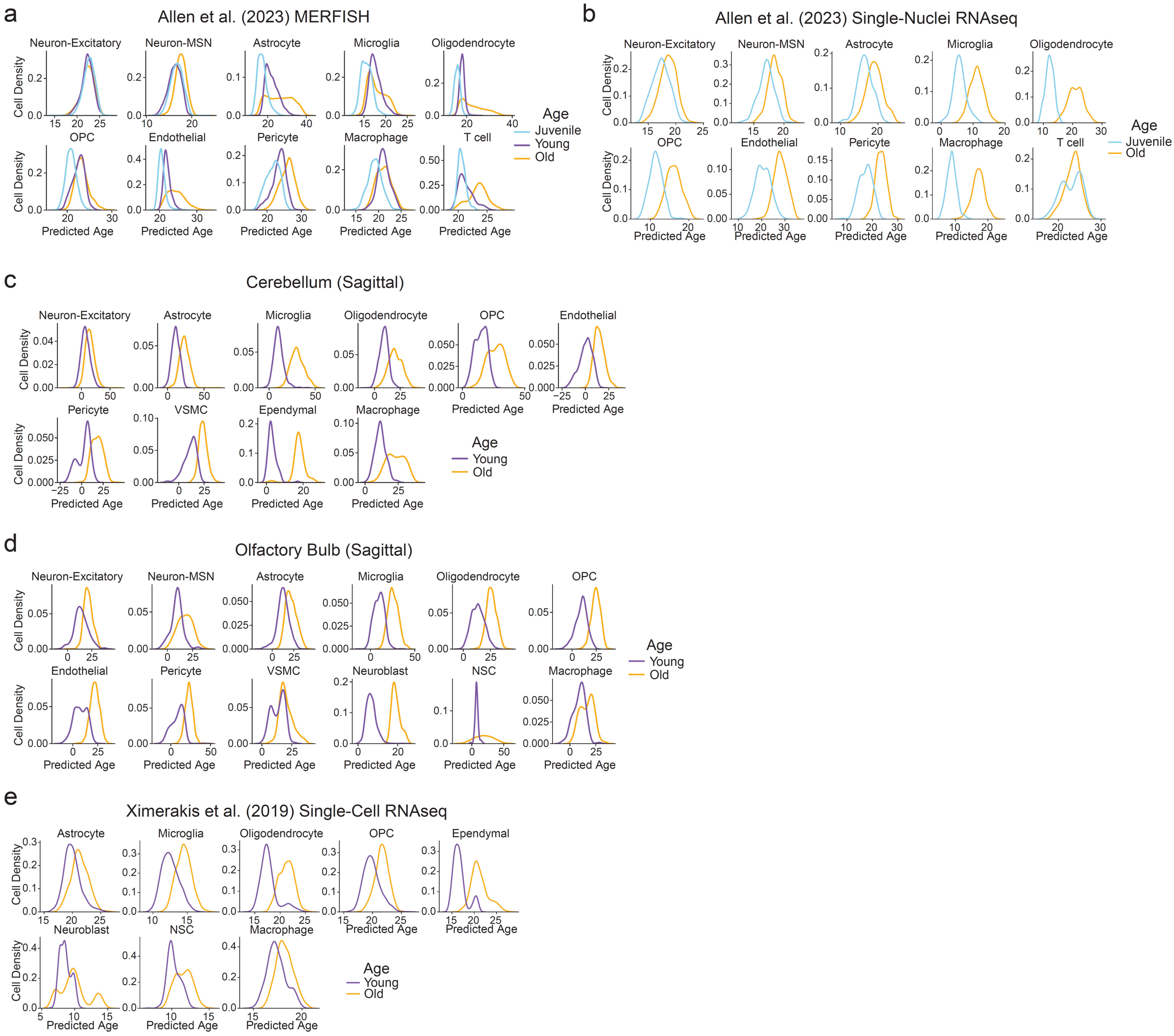

Extended Data Fig. 6 | Generalizability of spatial aging clocks. a-e, Density of predicted ages computed using spatial aging clocks for different age groups in the following datasets: **(a)** publicly available MERFISH dataset in female mice across juvenile (0.93 months), young (5.58 months), and old (20.93 months) age timepoints, with the dataset sharing 75 genes in common with the coronal section dataset; **(b)** publicly available single-nuclei RNA-seq dataset in female mice across juvenile (0.93 months) and old age (20.93 months) timepoints, with the dataset sharing 295 genes in common with the original dataset; **(c)** cerebellum region in the MERFISH sagittal section dataset with young (<9 months) and old (>19 months) age bins; **(d)** olfactory bulb region in the MERFISH sagittal section dataset with young (<9 months) and old (>19 months) age bins; **(e)** publicly available single-cell RNA-seq dataset of whole brain from male mice at young (2-3 months) and old (21-22 months) age, with the dataset sharing 264 genes in common with the coronal section dataset. Missing genes were imputed using SpaGE before spatial aging clock predictions were obtained. For statistics, see Supplementary Table 12.

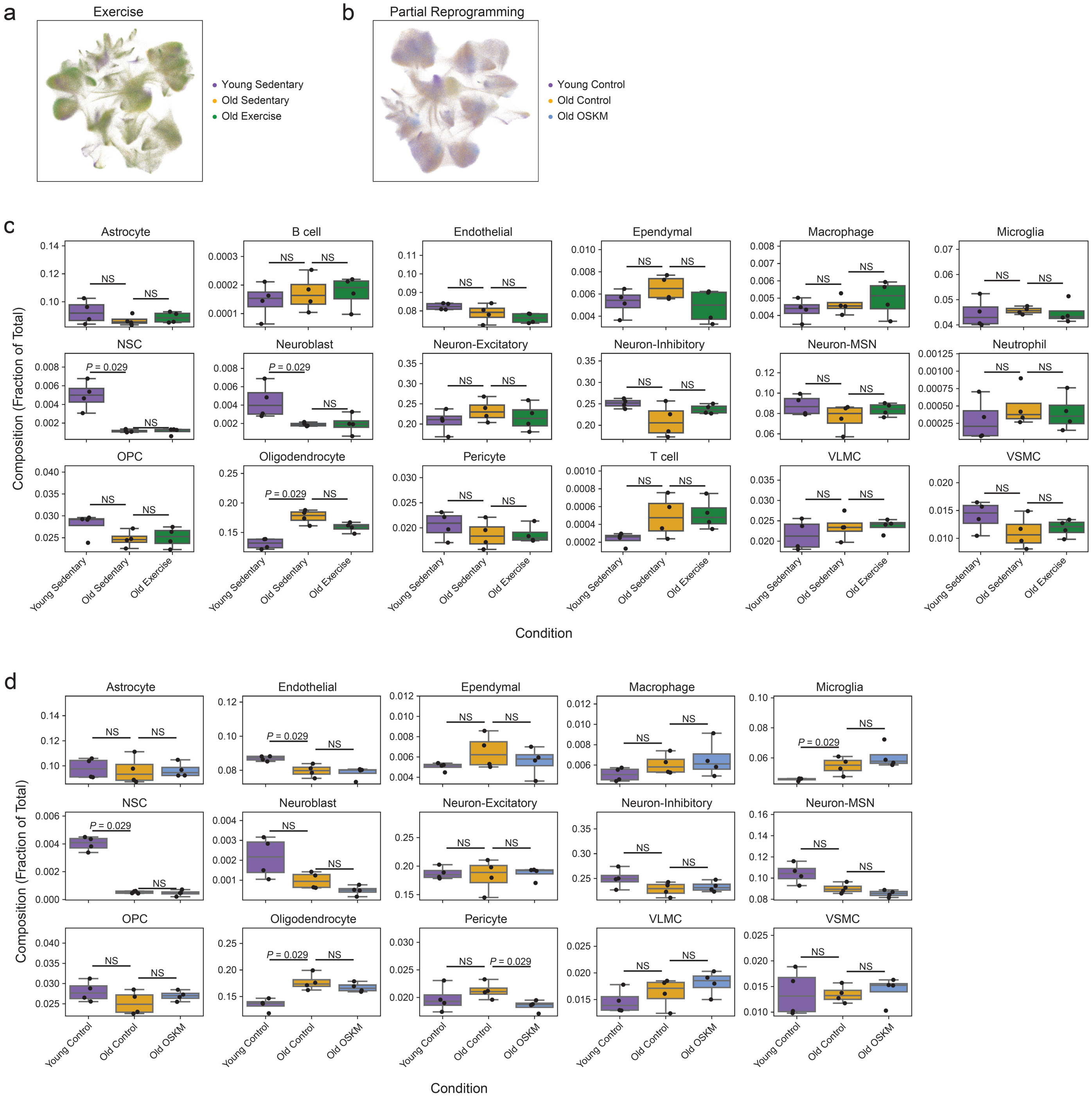

Extended Data Fig. 7 | Rejuvenating intervention experiments. a,b, UMAP visualization of all cells by age and experimental condition for the **(a)** exercise cohort and **(b)** partial reprogramming cohort. **c,d**, Box plots showing cell type proportions for each cell type and across experimental conditions for the **(c)** exercise cohort and **(d)** partial reprogramming cohort. Dots indicate proportions for individual mice (*n* = 4 per condition). The line indicates the median, the box corresponds to 25th and 75th quartiles, and the whiskers span up to 1.5 times the interquartile range. *P*-values computed using two-sided Mann-Whitney test. Not significant *P* > 0.05 abbreviated as "NS".

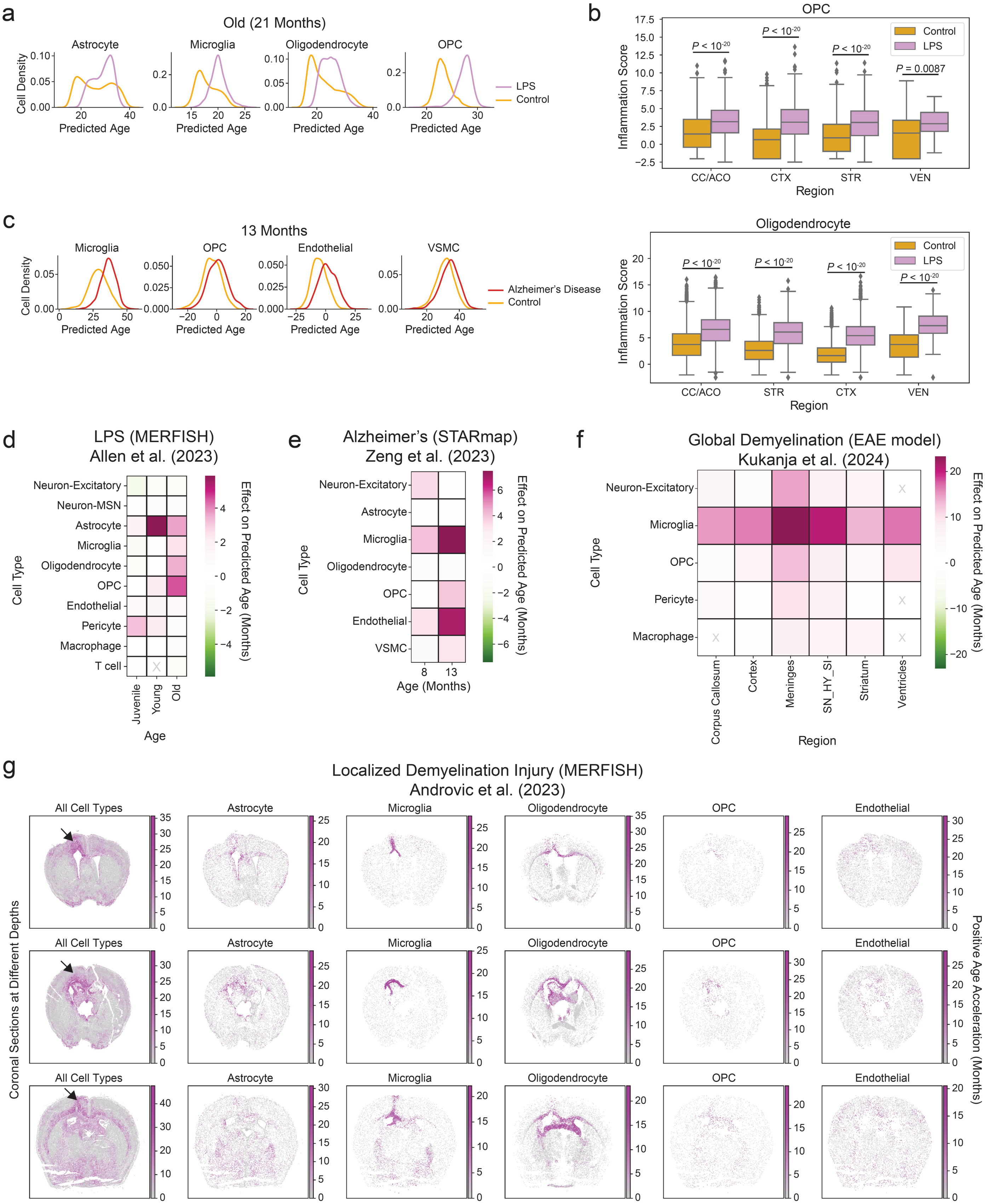

Extended Data Fig. 8 | See next page for caption.

Extended Data Fig. 8 | Spatial aging clocks record adverse interventions. **a**, Density of predicted ages across different experimental conditions and ages for spatial aging clocks corresponding to four cell types with accelerated aging under LPS-induced inflammation. For statistical analysis, see Supplementary Table 12. **b**, Boxplots of the oligodendrocyte inflammation score computed on scaled log-normalized gene expression values from the LPS MERFISH dataset for oligodendrocyte progenitor cells (OPCs) (top) and oligodendrocytes (bottom) across four anatomic regions and compared between LPS-injected and control conditions. *P*-values computed using two-sided Mann-Whitney test. For OPCs: CC/ACO control $n = 916$ cells, CC/ACO LPS $n = 621$ cells; CTX control $n = 2071$ cells, CTX LPS $n = 1391$ cells; STR control $n = 432$ cells, STR LPS $n = 388$ cells; VEN control $n = 35$ cells, VEN LPS $n = 27$ cells. For oligodendrocytes: CC/ACO control $n = 23858$ cells, CC/ACO LPS $n = 12591$ cells; CTX control $n = 13222$ cells, CTX LPS $n = 7548$ cells; STR control $n = 4690$ cells, STR LPS n = 4050 cells; VEN control $n = 241$ cells, VEN LPS $n = 110$ cells. The line indicates the median, the box corresponds to 25th and 75th quartiles, and the whiskers span up to 1.5 times the interquartile range with diamonds showing outlier values. **c**, Density of predicted ages across different experimental conditions and ages for spatial aging clocks corresponding to four cell types with accelerated aging in Alzheimer's disease models. For statistical analysis, see Supplementary Table 12. **d,e**, Heatmaps showing the effect of adverse interventions on predicted age for different cell types, measured as the difference in median predicted age between intervention and control conditions, across different age groups, under **(d)** systemic inflammatory challenge by LPS injection across female juvenile (0.93 months), young (5.58 months), and old (20.93 months) mice and **(e)** for Alzheimer's disease model male mice across 8 and 13 months of age. Gray "X" denotes cell types and regions with insufficient numbers of cells (<50). **f**, Heatmap showing the effect of global demyelination injury (EAE model of multiple sclerosis) on predicted age for different cell types and regions, measured as the difference in median predicted age between intervention and control conditions for the EAE model in young (2.2 months) male and female mice in an in situ sequencing dataset. Gray "X" denotes cell types and regions with insufficient numbers of cells (<50). "SN_HY_SI" refers to the region between the ventricles containing the substantia nigra and hypothalamus. **g**, Scatter plot of cells by their spatial coordinates in the localized demyelination injury MERFISH dataset with cells colored by the positive age acceleration (age acceleration with a floor value of zero) obtained from the spatial aging clocks. The leftmost column shows all cells with the site of injury marked with an arrow, and the other columns show select cell types. Three coronal sections at different depths are shown across the rows.

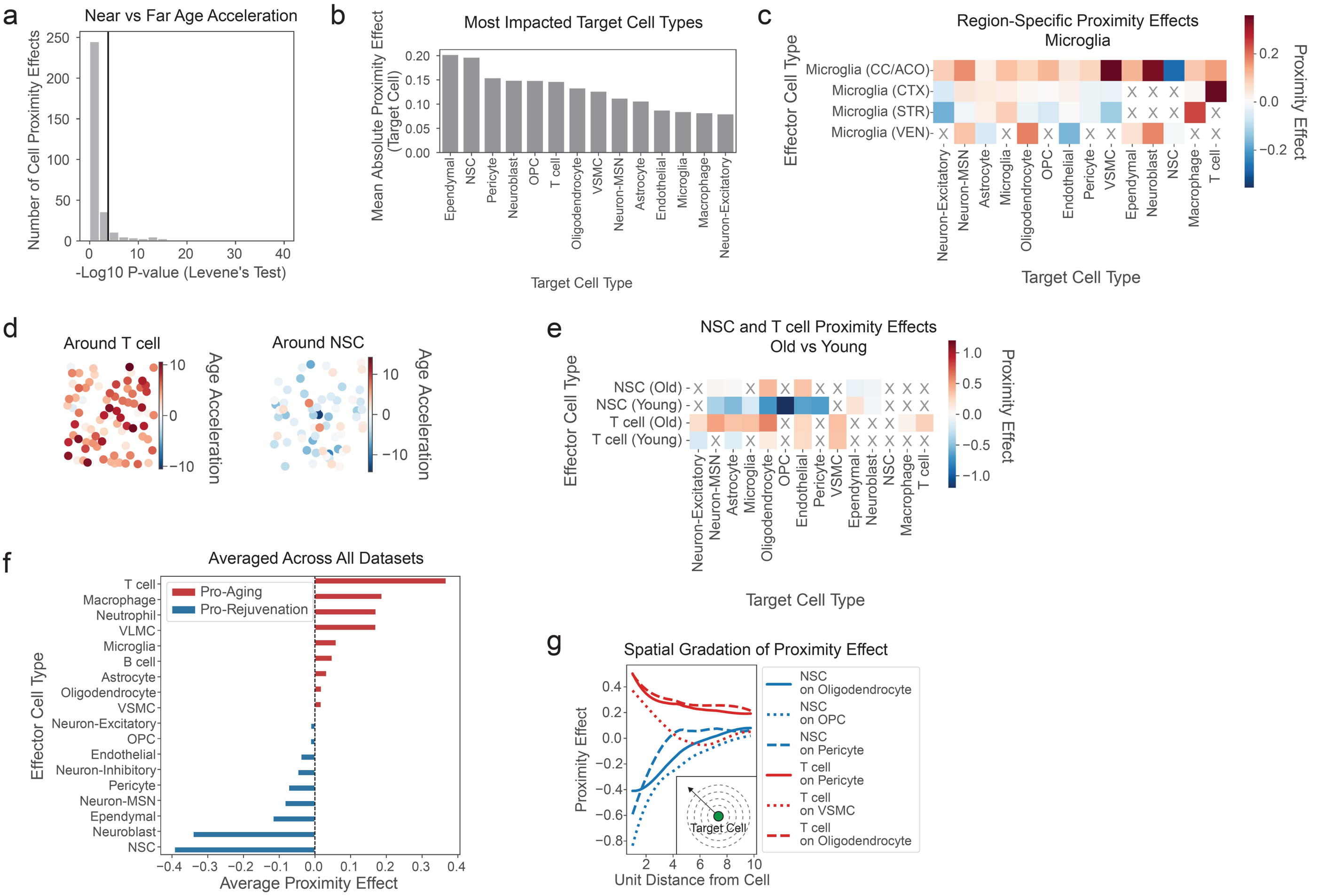

Extended Data Fig. 9 | Specificity and robustness of cell proximity effects. **a**, Histogram showing distribution of negative log10 *P*-values from Levene's test for equal variance between age acceleration of "Near" versus "Far" cell groups for each of the observed cell proximity effects. Solid vertical black line indicates the Bonferroni-adjusted cutoff corresponding to $P = 0.05$. **b**, Target cell types ranked by their mean absolute proximity effect experienced across all effector cell types. **c**, Heatmap showing the proximity effect for different cell type proximity relationships separated by brain region for microglia for NSCs and T cells. Rows correspond to the effector cell type and columns correspond to the target cell type, which experiences the proximity effect by the effector cells. "X" denotes proximity relationships for which there were insufficient cell pairings (<50) to compute a proximity effect (see Methods). **d**, Spatial visualization of cells within 100 microns from an example T cell (left) and NSC (right) with colors corresponding to age acceleration. **e**, Heatmap showing the proximity effect for different cell type proximity relationships separated by young (<16 months) and old (>16 months) for NSCs and T cells with the same plotting and statistical parameters as in (c). **f**, Mean of the average proximity effects for a given effector cell type on all other target cell types ranked from most pro-aging (positive aging effect) to most pro-rejuvenating (negative aging effect) across seven datasets (see Supplementary Table 15). **g**, Spatial gradation of the proximity effect as a function of the unit distance from the target cell (see Methods) for three select pro-aging proximity relationships with T cell as the effector cell type and three select pro-rejuvenating proximity relationships with NSC as the effector cell type. Cutout shows scheme for spatial gradation analysis.

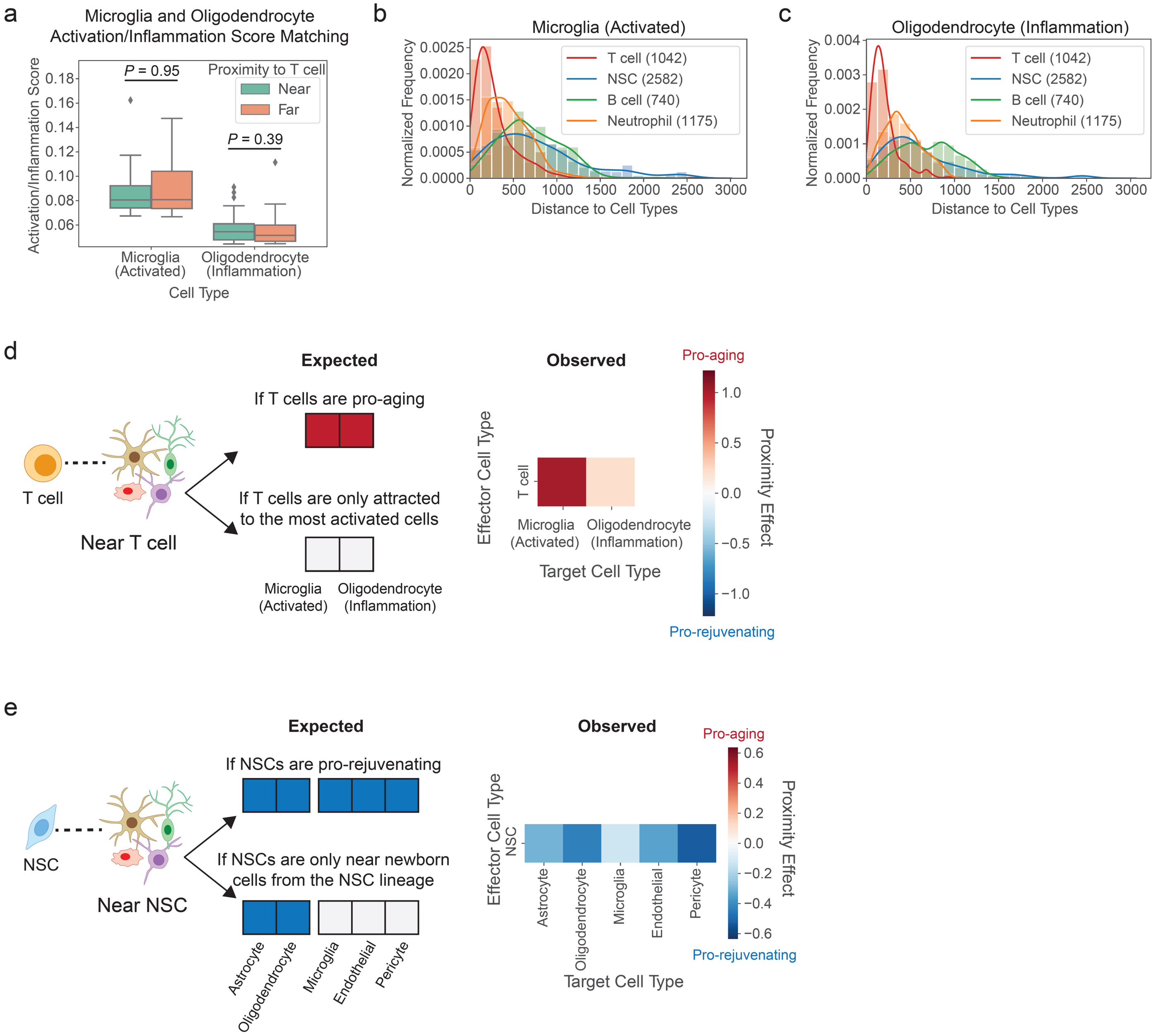

Extended Data Fig. 10 | Controls for inflammation and proliferation. **a**, Boxplots of the glial activation/inflammation gene signature score for "Far" and "Near" activated/inflamed glia near T cells (activated/inflamed status determined by top 0.2% expression of signature). For activated microglia, $n = 15$ cells near T cell and $n = 16$ cells far from T cell. For inflamed oligodendrocytes, $n = 64$ cells near T cell and $n = 64$ cells far from T cell. The line indicates the median, the box corresponds to 25th and 75th quartiles, and the whiskers span up to 1.5 times the interquartile range with diamonds showing outlier values. *P*-values computed using two-sided Mann-Whitney test. **b**,**c**, Density plots and histograms showing the nearest distance to different cell types for **(b)** all activated microglia and **(c)** all inflamed oligodendrocytes in the coronal section dataset. Numbers of cells for each cell type are listed in parentheses in the legend. **d**, Schematic showing expected heatmaps (left) for different T cell proximity effect scenarios and the observed heatmap (right) showing the T cell proximity effect on glial cell subtypes (activated/inflamed status, see Methods). **e**, Schematic showing expected heatmaps (left) for different NSC proximity effect scenarios and the observed heatmap (right) showing NSC proximity effect on terminal cell types in the NSC lineage (astrocytes, oligodendrocytes) and cells not in the lineage (microglia, endothelial cells, pericytes) reproduced from (Fig. 4b).

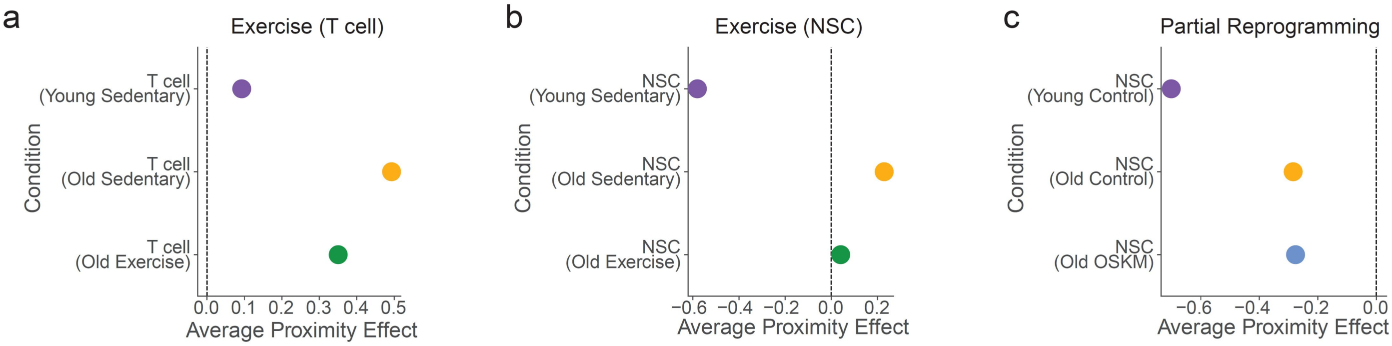

Extended Data Fig. 11 | Impact of exercise and partial reprogramming on proximity effects. a,b, Average proximity effects of **(a)** T cells and **(b)** NSCs on nearby cells computed from all cells in the exercise dataset for each of the three experimental conditions (Young Sedentary, Old Sedentary, Old Exercise). **c**, Average proximity effect of NSCs on nearby cells computed from all cells in the partial reprogramming dataset for each of the three experimental conditions (Young Control, Old Control, Old OSKM). There were no T cells detected in the partial reprogramming mouse model (see Methods).

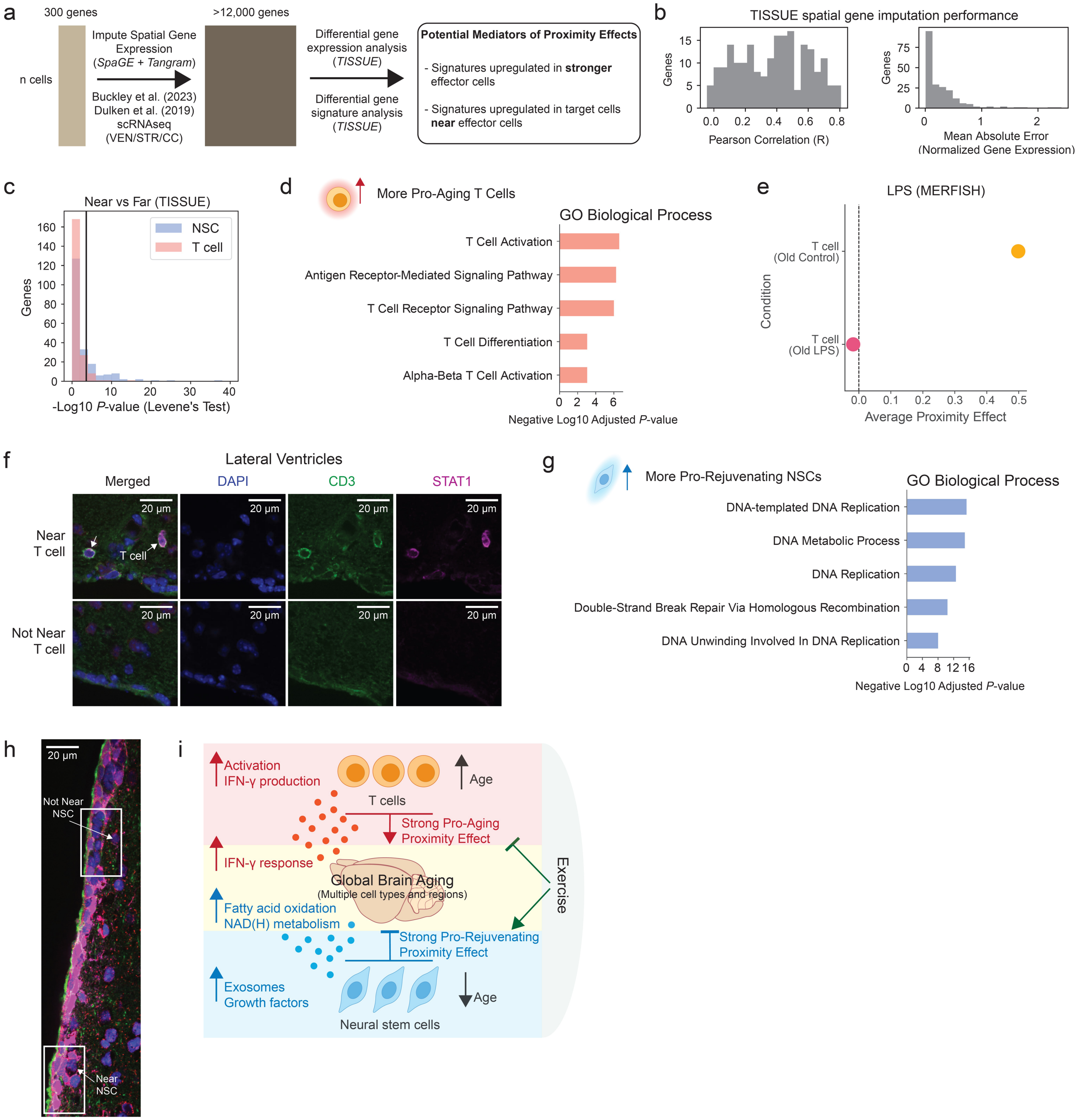

Extended Data Fig. 12 | See next page for caption.

Extended Data Fig. 12 | Identification and validation of potential mediators of cell proximity effects. a, Schematic of the computational pipeline using SpaGE and Tangram algorithms for spatial gene expression imputation and using TISSUE for uncertainty-aware differential expression testing of imputed gene expression and gene signatures related to potential mediators of proximity effects. **b**, Histograms of gene-wise performance metrics for SpaGE imputation comparing predicted to actual gene expression using Pearson correlation (left) and mean absolute error (right). **c**, Histogram showing distribution of negative log10 *P*-values from Levene's test for equal variance between SpaGE-imputed gene expression in "Near" versus "Far" cells with respect to NSCs or T cells. Solid vertical black line indicates the Bonferroni-adjusted cutoff corresponding to $P = 0.05$. **d**, Bar plots showing the top five most enriched GO Biological Processes for significantly upregulated genes in more pro-aging T cells compared to less pro-aging T cells. *P*-values computed from EnrichR pathway enrichment analysis. **e**, Average proximity effects of T cells computed from all nearby cells in the LPS MERFISH study for each of the two experimental conditions (Old Control, Old LPS) with reduced *Ifng* expression in Old LPS condition. **f**, Immunofluorescence staining image of a perfused mouse brain section from an old (28 months old) male mouse highlighting elevated STAT1 fluorescence (magenta) in cells near T cells (marked by arrows, top panels) compared to cells not near T cells (bottom panels) in the lateral ventricles. Images were taken from the same brain section. **g**, Bar plots showing the top five most enriched GO Biological Processes for significantly upregulated genes in more pro-rejuvenating NSCs compared to less pro-rejuvenating NSCs. *P*-values computed from EnrichR pathway enrichment analysis. **h**, Immunofluorescence staining image of the perfused mouse lateral ventricle from a young (3.5 months) male mouse with cutouts highlighting elevated CPT1A fluorescence in cells near NSCs (S100A6^{+}) with high CD9 fluorescence compared to cells not near NSCs. Arrows within white rectangles label example cell near NSC and example cell not near NSC. **i**, Summary of T cell and NSC proximity effects and their potential mediators.

nature portfolio

Corresponding author(s): Anne Brunet, James Zou

Last updated by author(s): Oct 9, 2024

Reporting Summary

Nature Portfolio wishes to improve the reproducibility of the work that we publish. This form provides structure for consistency and transparency in reporting. For further information on Nature Portfolio policies, see our Editorial Policies and the Editorial Policy Checklist.

Statistics

For all statistical analyses, confirm that the following items are present in the figure legend, table legend, main text, or Methods section.

n/a	Confirmed	
☐	☒	The exact sample size (n) for each experimental group/condition, given as a discrete number and unit of measurement
☐	☒	A statement on whether measurements were taken from distinct samples or whether the same sample was measured repeatedly
☐	☒	The statistical test(s) used AND whether they are one- or two-sided *Only common tests should be described solely by name; describe more complex techniques in the Methods section.*
☐	☒	A description of all covariates tested
☐	☒	A description of any assumptions or corrections, such as tests of normality and adjustment for multiple comparisons
☐	☒	A full description of the statistical parameters including central tendency (e.g. means) or other basic estimates (e.g. regression coefficient) AND variation (e.g. standard deviation) or associated estimates of uncertainty (e.g. confidence intervals)
☐	☒	For null hypothesis testing, the test statistic (e.g. F, t, r) with confidence intervals, effect sizes, degrees of freedom and P value noted *Give P values as exact values whenever suitable.*
☒	☐	For Bayesian analysis, information on the choice of priors and Markov chain Monte Carlo settings
☒	☐	For hierarchical and complex designs, identification of the appropriate level for tests and full reporting of outcomes
☐	☒	Estimates of effect sizes (e.g. Cohen's d, Pearson's r), indicating how they were calculated

Our web collection on statistics for biologists contains articles on many of the points above.

Software and code

Policy information about availability of computer code

Data collection	Confocal microscopy: Zeiss ZEN Blue 3.0, NIS-Elements software (AR 4.30.02, 64-bit)
Data analysis	python (3.8.13), pandas (1.4.2), matplotlib (3.5.1), seaborn (0.12.2), numpy (1.21.6), scipy (1.8.0), sklearn (1.0.2), anndata (0.8.0), scanpy (1.9.1), squidpy (1.1.2) were used for most plotting and data analysis tasks. Other software used for specific data analysis include tissue-sc (0.0.2), tangram-sc (1.0.3), spage (package included in repository), gseapy (1.0.4), umap-learn (0.5.3), statsmodels (0.13.2), topgo (R package version 2.54.0), QuPath (0.5.1), ImageJ (1.53n), vpt (1.2.2), cellpose (1.0.2). All code used for data analysis and experiments is available at https://github.com/sunericd/spatial_aging_clocks.

For manuscripts utilizing custom algorithms or software that are central to the research but not yet described in published literature, software must be made available to editors and reviewers. We strongly encourage code deposition in a community repository (e.g. GitHub). See the Nature Portfolio guidelines for submitting code & software for further information.

Data

Policy information about availability of data

All manuscripts must include a data availability statement. This statement should provide the following information, where applicable:

- Accession codes, unique identifiers, or web links for publicly available datasets
- A description of any restrictions on data availability
- For clinical datasets or third party data, please ensure that the statement adheres to our policy

The processed MERFISH spatial transcriptomics datasets generated for this study are available at https://doi.org/10.5281/zenodo.13883177. The aging and LPS injection dataset and the associated single-nuclei RNAseq dataset were accessed from https://cellxgene.cziscience.com/collections/31937775-0602-4e52-a799-b6acdd2bac2e. The single-cell RNAseq aging dataset of whole mouse brain was accessed from https://portals.broadinstitute.org/single_cell/study/aging-mouse-brain. The Alzheimer's model dataset was accessed from https://singlecell.broadinstitute.org/single_cell/study/SCP1375. The multiple sclerosis model dataset with global demyelination via experimental autoimmune encephalomyelitis was accessed from https://zenodo.org/records/8037425. The localized demyelination injury dataset was accessed from Gene Expression Omnibus under accession number GSE202638. The single-cell RNAseq datasets for the subventricular zone across lifespan were accessed from https://zenodo.org/doi/10.5281/zenodo.7145398. The single-cell RNAseq dataset on exercise in the subventricular zone was accessed from https://zenodo.org/doi/10.5281/zenodo.7338745. The single-cell RNAseq dataset on partial reprogramming in the subventricular zone was accessed from the Gene Expression Omnibus under accession number GSE224438. The GenAge database was accessed at https://genomics.senescence.info/genes/models.html.

Research involving human participants, their data, or biological material

Policy information about studies with human participants or human data. See also policy information about sex, gender (identity/presentation), and sexual orientation and race, ethnicity and racism.

Reporting on sex and gender	This study did not involve human participants.
Reporting on race, ethnicity, or other socially relevant groupings	This study did not involve human participants.
Population characteristics	This study did not involve human participants.
Recruitment	This study did not involve human participants.
Ethics oversight	This study did not involve human participants.

Note that full information on the approval of the study protocol must also be provided in the manuscript.

Field-specific reporting

Please select the one below that is the best fit for your research. If you are not sure, read the appropriate sections before making your selection.

☒ Life sciences ☐ Behavioural & social sciences ☐ Ecological, evolutionary & environmental sciences

For a reference copy of the document with all sections, see nature.com/documents/nr-reporting-summary-flat.pdf

Life sciences study design

All studies must disclose on these points even when the disclosure is negative.

Sample size	Sample size for MERFISH was determined by literature review and on our own previous published studies on single-cell RNAseq datasets for building cell type-specific transcriptomic aging clocks and for different rejuvenation interventions (Buckley et al., 2023). For immunofluorescence experiments, sample size was determined based on previous immunostaining experiments for neural stem cells and T cells in the adult mouse brain from previous published studies (Yeo et al., 2023, Dulken et al., 2019). We did not perform power analysis in selecting sample size.
Data exclusions	One MERFISH slide containing two coronal sections (slide B18 in the metadata containing samples 67 and 89) was removed from the coronal aging cohort dataset for all downstream processing and data analysis due to technical artifacts. A batch-specific cluster of very small volume cells corresponding to false cell segmentations was removed from the coronal section aging dataset, sagittal section aging dataset, exercise dataset, and partial reprogramming dataset.
Replication	For the aging cohort datasets, we collected two independent cohorts at two different times. For the brain coronal section aging experiment, each cohort contributed 10 coronal sections (from 10 independent mice), for a total of 20 coronal sections. For the brain sagittal section experiment, one cohort contributed 2 sagittal sections (from 2 independent mice) for the first cohort and the other cohort contributed 4 sagittal sections (from 4 independent mice) for a total of 6 samples. Findings were highly consistent across the replicates. For the voluntary exercise cohort and whole-body partial reprogramming cohort, one experiment (each with 4 independent mice per group) was conducted. MERFISH experiments were conducted at two different times and separately for each cohort with the exception of the exercise cohort samples, which were evenly split across groups for two MERFISH experiments (2 independent mice per group per MERFISH experiment).

Randomization	When possible, mice from multiple orders were randomized to build the aging cohort. For whole-body partial reprogramming, mice were paired by age and weight and the allocation of a mouse within each pair to intervention or control was randomized. For exercise, littermates were randomized to intervention or control.
Blinding	Blinding was not done for sample collection. However, processing of the sections for MERFISH data was done at Vizgen, with no prior knowledge of the specific conditions.

Reporting for specific materials, systems and methods

We require information from authors about some types of materials, experimental systems and methods used in many studies. Here, indicate whether each material, system or method listed is relevant to your study. If you are not sure if a list item applies to your research, read the appropriate section before selecting a response.

Materials & experimental systems

n/a	Involved in the study
☐	☒ Antibodies
☒	☐ Eukaryotic cell lines
☒	☐ Palaeontology and archaeology
☐	☒ Animals and other organisms
☒	☐ Clinical data
☒	☐ Dual use research of concern
☒	☐ Plants

Methods

n/a	Involved in the study
☒	☐ ChIP-seq
☒	☐ Flow cytometry
☒	☐ MRI-based neuroimaging

Antibodies

Antibodies used	Primary antibodies used were as follows: anti-GFAP (1:1000 dilution, Abcam, ab53554), anti-Ki67 (1:500 dilution, Thermo Fisher Scientific, 14-5698-82), anti-DCX (1:500 dilution, Millipore Sigma, AB2253), anti-EGFR (1:200 dilution, Millipore Sigma, 06-847), anti-STAT1 (1:500 dilution, Cell Signaling Technology, 14994), anti-CD3 (1:500, Abcam, ab11089), anti-S100A6 (1:500, Abcam, ab181975), anti-CD9 (1:100, Thermo Fisher, eBioKMC8 (KMC8)), anti-CPT1A (1:200, Abcam, ab128568). Secondary antibodies used were as follows: Donkey anti-Goat 647 (1:500 dilution, Invitrogen, A21447), Donkey anti-Rabbit 488 (1:500 dilution, Invitrogen, A-21206), Donkey anti-Guinea pig 594 (1:500 dilution, Jackson ImmunoResearch, 706-585-148), Donkey anti-Rat 647 (1:500 dilution, Invitrogen, A48272), Donkey anti-Rat 488 (1:500, Invitrogen, A21208), Donkey anti-Mouse 647 (1:500, Invitrogen, A31571), Donkey anti-Rabbit 568 (1:500, Invitrogen, A10042).
Validation	All antibodies were validated by the manufacturers. Antibodies for GFAP, Ki67, DCX, EGFR, STAT1, CD3, S100A6 were selected based on extensive validation by the field, including prior publications from our lab: Yeo et al. (2023), Xu et al. (2024), Dulken et al. (2019). Antibodies for CD9 (Morton et al., 2018) and CPT1A (Knobloch et al., 2017) were selected based by validation in the field for similar use cases.

Animals and other research organisms

Policy information about studies involving animals; ARRIVE guidelines recommended for reporting animal research, and Sex and Gender in Research

Laboratory animals	For the aging cohort (age range: 3.4-34.5 months) and exercise cohort (age range: 3 months for young, 19 months for old), male C57BL/6JN mice were obtained from the National Institute on Aging (NIA) Aged Rodent colony. For the whole-body partial reprogramming cohort, male whole-body inducible OSKM (iOSKM) mice [ROSA26(rtTA-M2); Col1a1(tetO-OSKM)] with age ranges (4.8-4.9 months for young and 25.6-29.2 months for old) were obtained from the Jackson Laboratory (JAX #011004). Mice were housed under 12-hour light/dark cycles, approximately 21 °C ambient temperature, and approximately 50% humidity. Mice in the aging experiments were housed in groups of 3 to 5 mice. For the exercise and whole-body partial reprogramming experiments, all mice were individually housed during the experiment.
Wild animals	No wild animals were used in this study.
Reporting on sex	Data generated through this study was only for male mice. However, validation and application of our models was achieved on publicly available data including for those of female mice.
Field-collected samples	No field-collected samples were used in this study.
Ethics oversight	All procedures involving mice were performed according to protocols approved by the Stanford University IACUC/AAPLAC (Protocol #8661) and VA Palo Alto Committee on Animal Research ACORP (LUO1736)

Note that full information on the approval of the study protocol must also be provided in the manuscript.

Plants

Seed stocks	No plants were used in this study.
Novel plant genotypes	No plants were used in this study.
Authentication	No plants were used in this study.